

## Computational and Experimental Investigation of Quadrotor Aerodynamics and Aeroacoustics

Anna Aleksandra Kostek

Deutsches Zentrum für Luft- und Raumfahrt  
Institut für Aerodynamik und Strömungstechnik  
Göttingen



DLR

Deutsches Zentrum  
für Luft- und Raumfahrt

# **Forschungsbericht 2024-18**

## **Computational and Experimental Investigation of Quadrotor Aerodynamics and Aeroacoustics**

Anna Aleksandra Kostek

Deutsches Zentrum für Luft- und Raumfahrt  
Institut für Aerodynamik und  
Strömungstechnik  
Göttingen

138 Seiten

121 Bilder

4 Tabellen

163 Literaturstellen



**Deutsches Zentrum  
DLR für Luft- und Raumfahrt**



*Herausgeber:*

Deutsches Zentrum  
für Luft- und Raumfahrt e. V.  
Wissenschaftliche  
InformationLinder Höhe  
D-51147 Köln

ISSN 1434-8454  
ISRN DLR-FB-2024-18  
Erscheinungsjahr 2024  
DOI: [10.57676/68kb-pv48](https://doi.org/10.57676/68kb-pv48)

**Erklärung des Herausgebers**

Als Manuskript gedruckt.

Abdruck oder sonstige Verwendung nur nach Absprache mit dem DLR gestattet.

*Panel-Methode, Quadrokoopter, Multikoopter, aerodynamische Wechselwirkungen*  
(Veröffentlicht in englischer Sprache)

Anna Aleksandra KOSTEK  
DLR, Institut für Aerodynamik und Strömungstechnik, Göttingen

**Numerische und experimentelle Untersuchung der Aerodynamik und Aeroakustik von Quadrokooptern**

Gottfried Wilhelm Leibniz Universität Hannover

Aerodynamische Wechselwirkungen haben einen entscheidenden Einfluss auf die Flugleistung und die aeroakustische Signatur von Quadrokooptern. Free-Wake-Methoden ermöglichen es, komplexe Multirotor-Strömungen mit geringem Rechenaufwand nachzubilden, wurden aber ursprünglich für Simulationen von Hubschrauberrotoren entwickelt. Daher ist es Ziel der Studie, die Anwendbarkeit einfacherer (lower fidelity) Methoden für die Vorhersage der Flugleistungen kleiner Rotoren nachzuweisen, die auch als Input für aeroakustische Berechnungen verwendet werden. Ein weiterer Fokus der Arbeit liegt auf der Charakterisierung von aerodynamischen Wechselwirkungen, die einen erheblichen Unterschied zur Superposition von Einzelrotoren verursachen.

Dazu werden Quadrokoopter-Konfigurationen sowohl experimentell als auch numerisch mit Strömungslösern unterschiedlicher Genauigkeit (fidelity) untersucht, darunter mehrere Free-Wake-Methoden und ein URANS-Löser. Die Effizienz der Diamantkonfiguration mit nicht überlappenden Rotorblättern wird im Vergleich zu vier isolierten Rotoren um 5% gesteigert. Bei aufgenickter Rotorebene ist der Effekt durch verstärkte aerodynamische Wechselwirkungen ausgeprägter. Dabei steigt die Effizienz der Diamantkonfiguration um bis zu 11% bei einem Rotorabstand von 1.2 Rotordurchmessern. Im Gegensatz dazu, erweisen sich die Wechselwirkungen in der Kreuzkonfiguration für alle Rotorabstände als nachteilig, mit einem Optimum bei einer Blattüberlappung von 0.04 Rotordurchmessern. Eine vertikale Anhebung der hinteren Rotoren über die Ebene der vorderen Rotoren in der Kreuzkonfiguration verbessert die Flugleistung des Quadrokoopters, während eine Anhebung des hinteren Rotors in der Diamantkonfiguration dessen Effizienz verringert.

*panel method, quadrotor, multicopter, aerodynamic interactions*

Anna Aleksandra KOSTEK  
German Aerospace Center (DLR), Institute of Aerodynamics and Flow Technology, Göttingen

**Computational and Experimental Investigation of Quadrotor Aerodynamics and Aeroacoustics**

Gottfried Wilhelm Leibniz University Hannover

Aerodynamic interactions have a significant effect on quadrotor performance and aeroacoustic signature. Free wake methods allow the simulation of complex multirotor flows at a low computational cost, yet they were originally developed for simulations of full-scale helicopter rotors. The study aims to demonstrate the applicability of lower fidelity methods for predicting small-size rotors performance, also used as input for aeroacoustic computations. Another focus is to characterise the aerodynamic interactions that cause a considerable difference to the superposition of single rotors.

Quadrotor configurations are investigated experimentally and numerically using solvers of different fidelity, including free wake methods and an URANS tool. The efficiency of a diamond configuration with non-overlapping rotor blades improves by 5% compared to four isolated rotors. The effect is pronounced for the nose-up rotor tilt with intensified interactions, for which the efficiency of the diamond configuration increases by 11% at the rotor spacing of 1.2 rotor diameters. In contrast, interactions in the square configuration are detrimental for all spacings with the optimum at blade overlap of 0.04 rotor diameters. Adding a vertical offset of the back rotors relative to the front rotors in the square configuration improves the quadrotor performance, while raising the rearmost rotor in the diamond configuration causes a decrease in its efficiency.





# COMPUTATIONAL AND EXPERIMENTAL INVESTIGATION OF QUADROTOR AERODYNAMICS AND AEROACOUSTICS

Der Fakultät für Maschinenbau  
der Gottfried Wilhelm Leibniz Universität Hannover  
zur Erlangung des akademischen Grades  
Doktor-Ingenieur  
vorgelegte Dissertation

von  
Anna Aleksandra Kostek, M.Sc.

2024

Referent: Prof. Dr.-Ing. Markus Raffel

Korreferent: Prof. Dr.-Ing. Tomasz Goetzendorf-Grabowski

Tag der Promotion: 20.09.2024

# Abstract

Aerodynamic interactions have a significant effect on quadrotor performance and aeroacoustic signature. Free wake methods allow the simulation of complex multirotor flows at a low computational cost, yet they were originally developed for simulations of full-scale helicopter rotors operating at high Reynolds numbers. Therefore, the study aims to demonstrate the applicability of lower fidelity methods for predicting small-size rotors performance, also used as input for aeroacoustic computations. Another focus is to characterise the aerodynamic interactions that cause a considerable difference to the superposition of single rotors.

For this purpose, quadrotor configurations are investigated experimentally and numerically using solvers of different fidelity, including free wake methods and an URANS tool. Depending on the solver, the rotor is represented with lifting lines, lifting surfaces or thick-blade models. The performance of the diamond and cross configurations in forward flight is compared at different quadrotor tilt angles as well as varying horizontal and vertical rotor spacings. The interaction effects are evaluated relative to the single rotor results. In order to identify separate effects, the generic two-rotor systems are analysed in the first step. All of the used tools capture interactions in tandem, side-by-side and oblique two-rotor alignments.

The efficiency of a diamond configuration with non-overlapping rotor blades improves by 5% compared to four isolated rotors. The effect is pronounced for the nose-up rotor tilt with intensified interactions, for which the efficiency of the diamond configuration increases by 11% at the rotor spacing of 1.2 rotor diameters. In contrast, interactions in the square configuration are detrimental for all spacings with the optimum at blade overlap of 0.04 rotor diameters. Adding a vertical offset of the back rotors relative to the front rotors in the square configuration improves the quadrotor performance, while raising the rearmost rotor in the diamond configuration causes a decrease in its efficiency.

The computational results show good agreement with the measured data for the forward rotor plane tilt, yet for the nose-up tilt angle a spread between the calculated values can be observed, especially for the torque. However, the general trends are

maintained in the simulations. The panel method is able to capture the absolute change in torque for cases without significant flow separation. The results show a stronger dependence on empirical vortex models than on the blade representation.

The results of a noise prediction based on calculations from a panel method and a URANS solver are compared for selected test cases. While rotor phasing can be neglected for quadrotor performance, it has a significant impact on the first harmonics of the blade passing frequency and thus on the overall sound pressure levels. However, aerodynamic interaction noise remains an important factor at higher harmonics.

**Key words:** panel method, quadrotor, multicopter, aerodynamic interactions

# Kurzfassung

## *Numerische und experimentelle Untersuchung der Aerodynamik und Aeroakustik von Quadroptern*

Aerodynamische Wechselwirkungen haben einen entscheidenden Einfluss auf die Flugleistung und die aeroakustische Signatur von Quadroptern. Free-Wake-Methoden ermöglichen es, komplexe Multirotor-Strömungen mit geringem Rechenaufwand nachzubilden, wurden aber ursprünglich für Simulationen von Hubschrauberrotoren mit hohen Reynoldszahlen entwickelt. Daher ist es Ziel der Studie, die Anwendbarkeit einfacherer (lower fidelity) Methoden für die Vorhersage der Flugleistungen kleiner Rotoren nachzuweisen, die auch als Input für aeroakustische Berechnungen verwendet werden. Ein weiterer Fokus der Arbeit liegt auf der Charakterisierung von aerodynamischen Wechselwirkungen, die einen erheblichen Unterschied zur Superposition von Einzelrotoren verursachen.

Dazu werden Quadropten-Konfigurationen sowohl experimentell als auch numerisch mit Strömungslösern unterschiedlicher Genauigkeit (fidelity) untersucht, darunter mehrere Free-Wake-Methoden und ein URANS-Löser. Je nach Solver wird der Rotor durch Traglinien, tragende Flächen oder dicke Blattmodelle dargestellt. Die Flugleistung wird für Diamant- und Kreuzkonfigurationen im Vorwärtsflug bei verschiedenen Neigungswinkeln des Multikopters sowie unterschiedlichen horizontalen und vertikalen Rotorabständen verglichen. Die Interaktionseffekte werden anhand der Ergebnisse eines Einzelrotors bewertet. Um die separate Effekte zu identifizieren, werden zunächst generische Zwei-Rotor-Systeme untersucht. Alle verwendeten Simulationsverfahren erfassen die Wechselwirkungen bei der Tandemkonfiguration sowie bei seitlicher und schräger Anordnung der Rotoren.

Die Effizienz der Diamantkonfiguration mit nicht überlappenden Rotorblättern wird im Vergleich zu vier isolierten Rotoren um 5% gesteigert. Bei aufgenickter Rotorebene ist der Effekt durch verstärkte aerodynamische Wechselwirkungen ausgeprägter. Dabei steigt die Effizienz der Diamantkonfiguration um bis zu 11% bei einem Rotorabstand von 1.2 Rotordurchmessern. Im Gegensatz dazu, erweisen

sich die Wechselwirkungen in der Kreuzkonfiguration für alle Rotorabstände als nachteilig, mit einem Optimum bei einer Blattüberlappung von 0.04 Rotordurchmessern. Eine vertikale Anhebung der hinteren Rotoren über die Ebene der vorderen Rotoren in der Kreuzkonfiguration verbessert die Flugleistung des Quadropters, während eine Anhebung des hinteren Rotors in der Diamantkonfiguration dessen Effizienz verringert.

Die Berechnungsergebnisse zeigen bei abgenickter Rotorebene eine gute Übereinstimmung mit den Messdaten. Bei aufgenickter Rotorebene kann eine Abweichung zwischen den berechneten Werten, insbesondere für das Drehmoment, beobachtet werden. Die Simulationen geben jedoch die Trends richtig wieder. Die Panel-Methode ist in der Lage, die absolute Änderung des Drehmoments für Fälle, in denen keine signifikante Strömungsablösung auftritt, korrekt zu erfassen. Die Ergebnisse der Free-Wake-Simulationen zeigen eine stärkere Abhängigkeit von empirischen Wirbelmodellen als von der Blattdarstellung.

Für ausgewählte Testfälle werden die Ergebnisse der Lärmprognose auf Basis der aerodynamischen Simulationen des Panelverfahrens und des URANS-Lösers verglichen. Die Phasenlage des Rotors kann zwar für die Flugleistung des Quadropters vernachlässigt werden, hat aber einen erheblichen Einfluss auf die ersten Harmonischen der Blattfolgefrequenz und damit auf den Gesamtschalldruckpegel. Dennoch bleibt der aerodynamische Interaktionslärm für die höheren Harmonischen ein wichtiger Faktor.

**Stichwörter:** Panel-Methode, Quadropters, Multiopters, aerodynamische Wechselwirkungen

# Publications

Following publications have been published in journals and conference proceedings within the scope of this work. Passages and figures from these articles were included in the thesis as noted in the text.

1. A. A. Kostek, J. N. Braukmann, F. Lößle, S. Miesner, A. Visingardi, R. Boisard, V. Riziotis, M. Keßler, A. D. Gardner, "Experimental and Computational Investigation of Aerodynamic Interactions in Quadrotor Configurations", *Journal of the American Helicopter Society*, Vol. 69, No. 2, 2024. DOI: 10.4050/JAHS.69.022009
2. A. A. Kostek, J. N. Braukmann, F. Lößle, S. Miesner, A. Visingardi, R. Boisard, V. Riziotis, M. Keßler, A. D. Gardner, "Experimental Investigation of Quadrotor Aerodynamics with Computational Cross-Validation", *Vertical Flight Society 79th Annual Forum*, West Palm Beach, Florida, USA, May 2023. DOI: 10.4050/F-0079-2023-17991
3. A. A. Kostek, F. Lößle, R. Wickersheim, M. Keßler, R. Boisard, G. Reboul, A. Visingardi, M. Barbarino, A. D. Gardner, "Experimental Investigation of UAV Rotor Aeroacoustics and Aerodynamics with Computational Cross-Validation", *CEAS Aeronautical Journal*, 2023. DOI: 10.1007/s13272-023-00680-z
4. A. A. Kostek, F. Lößle, R. Wickersheim, M. Keßler, R. Boisard, G. Reboul, A. Visingardi, M. Barbarino, A. D. Gardner, "Experimental Investigation of UAV Rotor Aeroacoustics and Aerodynamics with Computational Cross-Validation", *48th European Rotorcraft Forum*, Winterthur, Switzerland, Sept. 2022

Additionally, contributions to the following publications were made:

1. A. D. Gardner, A. A. Kostek, F. Lößle, J. N. Braukmann, "Experiments and modelling of multicopter rotor response to sinusoidal gusts", *Vertical Flight Society 80th Annual Forum*, Montréal, Québec, Canada, May 2024



2. F. Löffle, R. Schmid, D. Ernst, C. Schwarz, A. A. Kostek, "Experimentelle Untersuchung der Schallemission eines Kleinrotors", *DAGA - 50. Jahrestagung für Akustik*, Hannover, Germany, March 2024
3. R. Boisard, L. Lefevre, T. Zhang, G. Barakos, A. Visingardi, F. Löffle, A. Kostek, T. Andronikos, M. Keßler, R. Wickersheim, A. Colli, G. Gibertini, A. Zanotti, "Rotor / Rotor aerodynamic interactions – A Garteur Action Group", *33rd Congress of the International Council of the Aeronautical Sciences*, Stockholm, Sweden, Sept. 2022
4. F. Löffle, A. A. Kostek, C. Schwarz, R. Schmid, A. D. Gardner, M. Raffel, "Aerodynamics of small rotors in hover and forward flight", *48th European Rotorcraft Forum*, Winterthur, Switzerland, Sept. 2022
5. F. Löffle, A. A. Kostek, C. Schwarz, R. Schmid, "Experimental Measurement of a UAV Rotor's Acoustic Emission", *New Results in Numerical and Experimental Fluid Mechanics XIII, Notes on Numerical Fluid Mechanics and Multidisciplinary Design*, Vol. 151, 2021, pp. 387-396, DOI: 10.1007/978-3-030-79561-0\_37

# Acknowledgments

The thesis includes a comparison between several computational methods and experimental results, made possible thanks to collaborations within the institute and with other research facilities. The following contributions, which are not primarily the work of the main author, were done by:

- Felix Lößle (DLR): Isolated rotor experiment, preparation of the FW-H code,
- Johannes N. Braukmann (DLR): PIV setup and image processing,
- Antonio Visingardi (CIRA): RAMSYS calculations,
- Ronan Boisard (ONERA): PUMA calculations,
- Robin Wickersheim (University of Stuttgart): FLOWer + ACCO calculations (isolated rotor),
- Sebastian Miesner (University of Stuttgart): FLOWer + ACCO calculations (multirotor configurations),
- Mattia Barbarino (CIRA): ACO calculations,
- Gabriel Reboul (ONERA): KIM calculations,
- Vasilis Riziotis (NTUA): CORAL calculations.

The thesis is a summary of my work at the Institute of Aerodynamics and Flow Technology at the German Aerospace Center (DLR) Göttingen. I would like to say a huge thank you to the Helicopters Department for the atmosphere and support without which this thesis could not have been completed. First of all, I would like to thank Prof. Markus Raffel for giving me an opportunity to complete my PhD and for his very human approach as well as Tony Gardner for the great amount of advice and guidance within the project. Special thanks go to Felix Lößle for sharing his experimental data and experience as well as for his willingness to provide professional

and personal support at all times. I also want to thank Johannes Braukmann for his invaluable contribution in setting up the multirotor test stand and performing PIV measurements. I am very grateful for all the other substantive, linguistic and technical assistance of my colleagues, also bearing in mind that the change of rotor spacing was a joint effort I would like to thank Christian Wolf, Alexander Heintz, Hauke Bartzsch, Clemens Schwarz, Beatrice Carter, Vincent Domogalla, Michel Nöding and Markus Krebs.

The project was made possible thanks to the exchange within the GARTEUR AG-25 group "Rotor-rotor wakes interactions". I would like to give a special mention to Antonio Visingardi and Ronan Boisard who contributed to every stage of the computational study, and also to gratefully acknowledge the contributions of Sebastian Miesner, Robin Wickersheim, Vasilis Riziotis, Gabriel Reboul and Mattia Barbarino.

I would like to thank Prof. Goetzendorf-Grabowski from the Warsaw University of Technology and Prof. Poll from the Gottfried Wilhelm Leibniz Universität Hannover for their time and effort as members of my dissertation committee.

Last but not least I would like to express my special gratitude to my parents for their unconditional love and acceptance of all my ideas. I am very grateful to my friends, whose support knew no borders. To the people not mentioned above who I met professionally or privately and who enriched my time in Göttingen in many ways, thank you.

# Contents

	Page
<b>Contents</b>	xi
<b>List of Figures</b>	xv
<b>List of Tables</b>	xxi
<b>Nomenclature</b>	xxiii
<b>1 Introduction</b>	<b>1</b>
<b>2 Fundamentals and state of the art</b>	<b>5</b>
2.1 Rotor in forward flight . . . . .	5
2.1.1 Specifics of small rotor aerodynamics and aeroacoustics . . . . .	8
2.2 Low- and mid-fidelity methods for forward flight calculations . . . . .	11
2.2.1 Blade element theory . . . . .	11
2.2.2 Potential and vortex methods . . . . .	14
2.2.3 Aeroacoustic computations . . . . .	19
2.3 Aerodynamic interactions in multirotor configurations . . . . .	20
<b>3 Tools and methods</b>	<b>27</b>
3.1 Blade geometry and model preparation . . . . .	27
3.2 Computational tools . . . . .	29
3.2.1 BET and FW-H code . . . . .	29
3.2.2 UPM and APSIM . . . . .	33
3.2.3 PUMA and KIM . . . . .	38
3.2.4 CORAL . . . . .	39

3.2.5	RAMSYS and ACO suite . . . . .	39
3.2.6	FLOWer and ACCO . . . . .	41
3.3	Experimental setups . . . . .	43
3.3.1	Isolated rotor test campaign . . . . .	43
3.3.2	Multirotor test campaign . . . . .	45
<b>4</b>	<b>Isolated rotor study</b>	<b>51</b>
4.1	Aerodynamic loading prediction . . . . .	51
4.2	Noise prediction . . . . .	56
4.3	Scattering effects . . . . .	59
4.3.1	Influence of the shielding . . . . .	59
4.3.2	Installation and ground proximity effects . . . . .	60
4.4	Summary . . . . .	63
<b>5</b>	<b>Multirotor configurations study</b>	<b>65</b>
5.1	Reference results of an isolated rotor . . . . .	66
5.2	Two-rotor configurations . . . . .	67
5.2.1	Side-by-side alignment . . . . .	68
5.2.2	Tandem . . . . .	69
5.2.3	Oblique alignment . . . . .	71
5.3	Quadrotor configurations . . . . .	75
5.3.1	Square configurations . . . . .	78
5.3.2	Diamond configuration . . . . .	84
5.3.3	Influence of rotor phasing . . . . .	88
5.4	Discussion . . . . .	94
5.4.1	Accuracy of the measurement . . . . .	94
5.4.2	Discrepancies in torque prediction . . . . .	94
5.5	Quadrotor configurations with vertical spacing . . . . .	97
5.5.1	Square bearhug configuration . . . . .	101
5.5.2	Diamond configuration . . . . .	106
5.6	Summary . . . . .	110
<b>6</b>	<b>Discussion</b>	<b>113</b>
6.1	Real flight conditions . . . . .	113

---

6.2 Interactions at other advance ratios . . . . .	114
6.3 Torque prediction for other blade models . . . . .	116
<b>7 Conclusions</b>	<b>119</b>
<b>References</b>	<b>123</b>
<b>Curriculum Vitae</b>	<b>139</b>



# List of Figures

Figure 1.1: Quadrotor configurations after [117] . . . . .	2
Figure 1.2: Examples of the most popular quadcopters in 2023 . . . . .	3
Figure 2.1: Tilt angle sign convention . . . . .	6
Figure 2.2: Rotor in forward flight . . . . .	7
Figure 2.3: Aerodynamic rotor noise sources based on [20, 63, 98] . . . . .	8
Figure 2.4: Forward flight of a quadrotor after [117] . . . . .	9
Figure 2.5: Asymmetry of the rigid rotor’s wake in forward flight viewed from the front [79] . . . . .	10
Figure 2.6: Velocities and forces on a blade element . . . . .	13
Figure 2.7: Scheme of tangential (swirl) velocity profile of the tip vortex after [88] . . . . .	16
Figure 2.8: Examples of vortex core models . . . . .	17
Figure 2.9: Blade wake scheme after [82] . . . . .	17
Figure 2.10: Blade models with free wake based on [83] . . . . .	18
Figure 2.11: Vortex wake representations including tip vortex roll-up [88] . . . . .	19
Figure 2.12: Schematics of wake interference effect between two rotors in hover after Lee et al. [86] . . . . .	21
Figure 2.13: Interactions between rotors in hover depending Reynolds num- ber by Shukla et al. [131] . . . . .	22
Figure 2.14: Time-averaged PIV flowfield of a tandem configuration at $\mu =$ 0.69 by Stokkermans et al. [134] . . . . .	23
Figure 2.15: Urban air mobility designs . . . . .	24
Figure 3.1: Scanned blade with cross-sections . . . . .	27
Figure 3.2: Twist and chord distributions . . . . .	28
Figure 3.3: Example - trailing edge shapes of recreated profiles . . . . .	29
Figure 3.4: Blades connection in the KDE rotor . . . . .	29
Figure 3.5: Induced velocity distribution with Pitt and Peters model for 5400 RPM, 12.9 m/s, tilt -10° . . . . .	32



Figure 3.6: Viterna extrapolation of lift coefficient for higher angles of attack used in the BET code . . . . .	33
Figure 3.7: Numerical model used in UPM . . . . .	33
Figure 3.8: Influence of the number of spanwise panels on the results of an isolated rotor . . . . .	35
Figure 3.9: Panel distribution in UPM . . . . .	35
Figure 3.10: Thrust convergence study depending on the time step size (tilt $-10^\circ$ , 5400 RPM and flight velocity 12.9 m/s) . . . . .	36
Figure 3.11: Wake representations in UPM . . . . .	37
Figure 3.12: Applied blade models . . . . .	40
Figure 3.13: Wake of an isolated rotor visualised in FLOWer using $\lambda_2$ -criterion . . . . .	42
Figure 3.14: Numerical setup for 1r in FLOWer – background and rotor mesh with Chimera interpolation . . . . .	42
Figure 3.15: Computational mesh for 4r in FLOWer . . . . .	42
Figure 3.16: Integration surface for acoustic coupling as input for ACCO and physical surface of the rotor blade . . . . .	43
Figure 3.17: Rotor with a shielding element implemented in the Scatman tool . . . . .	43
Figure 3.18: Experimental setup . . . . .	44
Figure 3.19: Microphone positions relative to the rotor plane . . . . .	45
Figure 3.20: Experimental setup with investigated parameters . . . . .	46
Figure 3.21: Setup of the drive unit . . . . .	47
Figure 3.22: Frame support variants . . . . .	48
Figure 3.23: Initial blade positions depending on the rotor phasing . . . . .	48
Figure 3.24: Motor efficiency as a function of torque at 5400 RPM . . . . .	49
Figure 3.25: Torque coefficient measured and derived from electric power consumption . . . . .	49
Figure 3.26: PIV setup presented for the square configuration with a top view (left) and side view (right) relative to the rotor plane . . . . .	50
Figure 4.1: Effect of varying rotational speed on rotor thrust and torque at fixed tilt angle $-10^\circ$ and flight velocity 12.9 m/s . . . . .	52
Figure 4.2: Effect of varying flight velocity on rotor thrust and torque at fixed tilt angle $-10^\circ$ and rotational speed 5900 RPM . . . . .	53
Figure 4.3: Effect of varying tilt angle on rotor thrust and torque at fixed rotational speed 5400 RPM and flight velocity 12.9 m/s . . . . .	53
Figure 4.4: Rotor wake system development for different tilt angles (RAM-SYS) . . . . .	54

Figure 4.5:	Thrust fluctuations during one rotation for rotational speed 5400 RPM and flight velocity 12.9 m/s . . . . .	54
Figure 4.6:	Time signal of thrust for tilt 20° during one rotation with 5400 RPM and flight velocity 12.9 m/s . . . . .	55
Figure 4.7:	Noise carpets of the BPF, 5400 RPM, flight velocity 12.9 m/s, tilt angle -10°. (a) Experiment, (b) UPM+APSIM, (c) BET+FW-H, (d) FLOWer+ACCO, (e) PUMA+KIM, (f) RAMSYS+ACO . . . . .	56
Figure 4.8:	Noise carpets of the BPF, 5400 RPM, flight velocity 12.9 m/s, tilt angle 20°. (a) Experiment, (b) UPM+APSIM, (c) BET+FW-H, (d) FLOWer+ACCO, (e) PUMA+KIM, (f) RAMSYS+ACO . . . . .	57
Figure 4.9:	Noise carpets of the BPF, 5400 RPM, flight velocity 12.9 m/s, tilt angle 30°. (a) Experiment, (b) UPM+APSIM, (c) BET+FW-H, (d) FLOWer+ACCO, (e) PUMA+KIM, (f) RAMSYS+ACO . . . . .	58
Figure 4.10:	Vortex trajectories detected in BOS pictures and UPM wake visualisations . . . . .	58
Figure 4.11:	Noise carpets from UPM with particle wake + APSIM . . . . .	59
Figure 4.12:	Acoustic field for the BPF on the shielding surface including incident noise (a), (b) and the sum of incident and scattered noise (c), (d); rotational speed 5400 RPM, flight velocity 12.9 m/s, tilt angle -10° . . . . .	60
Figure 4.13:	Noise carpet including total (incoming and scattered by the shielding) sound pressure level of the blade passing frequency - FW-H + ScatMan for 5400 RPM, flight velocity 12.9 m/s, tilt angle -10° . . . . .	61
Figure 4.14:	Acoustic mesh for BEM calculation . . . . .	61
Figure 4.15:	Integration surface for FW-H and BEM . . . . .	61
Figure 4.16:	Noise carpets including scattering effects for 5400 RPM and flight velocity 12.9 m/s . . . . .	62
Figure 4.17:	Noise carpets showing the difference between SPL calculated with RAMSYS+ACO and measured; 5400 RPM and flight velocity 12.9 m/s . . . . .	62
Figure 5.1:	Analysed tilt angles for quadrotor configurations . . . . .	65
Figure 5.2:	Wake of an isolated rotor at a tilt angle -10° visualised in UPM . . . . .	66
Figure 5.3:	Downwash of a single rotor captured with PIV for tilt -10° . . . . .	67
Figure 5.4:	Rotors side-by-side . . . . .	67
Figure 5.5:	Tandem . . . . .	67
Figure 5.6:	Rotors in oblique alignment . . . . .	67

Figure 5.7: Effects of varying tilt angle on rotor performance in the side-by-side alignment for $d/D=0.96$ . . . . .	68
Figure 5.8: Upwash regions between the rotors in side-by-side interaction, captured with PIV relative to an isolated rotor measurement for $d/D = 0.96$ and $\alpha_R = -10^\circ$ . . . . .	69
Figure 5.9: Effect of side-by-side alignment with tilt $-10^\circ$ on thrust of rotor 1 (UPM) . . . . .	70
Figure 5.10: Effect of side-by-side alignment with tilt $-10^\circ$ on torque of rotor 1, $d/D=0.96$ (UPM) . . . . .	70
Figure 5.11: Change in downwash of rotor 2 in tandem interaction relative to an isolated rotor, captured with PIV for $d/D = 0.96$ and $\alpha_R = -10^\circ$ . . . . .	70
Figure 5.12: Effects of varying tilt angle on the rotor performance in tandem for $d/D = 1.2$ . . . . .	71
Figure 5.13: Effect of tandem alignment on the thrust of rotor 2 (UPM) . . . . .	72
Figure 5.14: Effects of varying tilt angle on the performance of rotors in oblique alignment for $d/D=1.2$ . . . . .	73
Figure 5.15: Downwash of rotor 2 in oblique interaction relative to an isolated rotor, captured with PIV for $d/D=0.96$ and tilt $-10^\circ$ . . . . .	74
Figure 5.16: Effect of diagonal breaststroke alignment with tilt $0^\circ$ on the thrust of rotor 2 (UPM) . . . . .	74
Figure 5.17: Effect of diagonal breaststroke alignment with tilt $0^\circ$ on the torque of rotor 2 (UPM) . . . . .	74
Figure 5.18: Analysed quadrotor configurations . . . . .	75
Figure 5.19: Change in mean thrust of a quadrotor system with varying rotor spacing . . . . .	76
Figure 5.20: Change in mean torque of a quadrotor system with varying rotor spacing . . . . .	77
Figure 5.21: Change in mean thrust of each rotor in the square configuration with varying rotor spacing . . . . .	79
Figure 5.22: Change in mean torque of each rotor with varying rotor spacing for tilt angle $+10^\circ$ . . . . .	80
Figure 5.23: Comparison of the front rotor wake propagation in square bearhug (blue) and square breaststroke (green) . . . . .	80
Figure 5.24: Change in thrust of rotor 2 in the square configuration with $-10^\circ$ tilt (UPM) . . . . .	81

Figure 5.25: Change in thrust of rotor 2 in the square configuration with tilt $+10^\circ$ and $d/D=0.96$ (UPM) . . . . .	82
Figure 5.26: Change in thrust of rotor 1 in the square configuration with $\alpha_R = -10^\circ$ and $d/D = 0.96$ (UPM) . . . . .	82
Figure 5.27: Induced velocity fields of the square breaststroke configuration, $d/D = 1.2, \alpha_R = -10^\circ$ . . . . .	83
Figure 5.28: Change in mean thrust of each rotor in the square breaststroke configuration for $d/D=1.2$ and $\alpha_R = -10^\circ$ . . . . .	84
Figure 5.29: Relative change in azimuthal blade loading for rotor 3 and 4 in the square breaststroke configuration, $d/D=1.2, \alpha_R=-10^\circ$ . . . . .	84
Figure 5.30: Change in mean thrust of each rotor in the diamond configuration with varying rotor spacing for tilt angle $-10^\circ$ . . . . .	85
Figure 5.31: Induced velocity fields of the diamond configuration, $d/D = 1.2, \alpha_R = -10^\circ$ . . . . .	86
Figure 5.32: Change in thrust of rotor 4 in the diamond configuration with tilt $-10^\circ$ (UPM) . . . . .	86
Figure 5.33: Relative change in azimuthal blade loading for rotor 2 in the diamond configuration, $d/D = 1.2, \alpha_R = -10^\circ$ . . . . .	87
Figure 5.34: Change in mean thrust of each rotor in the diamond configuration for $d/D=1.2$ and tilt angle $-10^\circ$ . . . . .	87
Figure 5.35: Change in mean thrust and torque of each rotor in the diamond configuration with varying rotor spacing for tilt angle $+10^\circ$ . . . . .	89
Figure 5.36: Absolute changes of rotor thrust and torque in the diamond configuration depending on the rotor phasing, $d/D=1.2$ . . . . .	90
Figure 5.37: Analysed observer positions relative to the quadrotor centre . . . . .	91
Figure 5.38: Calculated OASPL on a plane 1.35 m below the quadrotor with $-10^\circ$ tilt, UPM+APSIM . . . . .	92
Figure 5.39: Calculated OASPL on a plane 1.35 m below the quadrotor with $-10^\circ$ tilt, FLOWer+ACCO . . . . .	92
Figure 5.40: Harmonic spectra at the observer position $[0,0,-1.35]$ depending on the rotor spacing and phasing . . . . .	93
Figure 5.41: Absolute torque change of rotor 2 for $d/D=1.2$ . . . . .	95
Figure 5.42: Difference between isolated rotor loads measured at front and back position of the square frame . . . . .	96
Figure 5.43: Change of torque of rotor 4 in the square bearhug configuration for $d/D=1.2$ depending on the isolated rotor reference . . . . .	97
Figure 5.44: Definition of the vertical spacing $z$ between the rotors for $d/D=1.2$ 98	

Figure 5.45: Change in mean thrust of the quadrotor with varying vertical rotor offset . . . . .	99
Figure 5.46: Change in mean torque of the quadrotor with varying vertical rotor offset . . . . .	100
Figure 5.47: Change in mean thrust of each rotor in square bearhug configuration with varying vertical rotor offset . . . . .	102
Figure 5.48: Change in thrust of rotor 1 in the square bearhug configuration with tilt $-10^\circ$ and $d/D = 0.96$ (UPM) . . . . .	103
Figure 5.49: Change in thrust of rotor 2 in the square bearhug configuration with tilt $10^\circ$ (UPM) . . . . .	104
Figure 5.50: Wake of the front rotor(s) in square bearhug configuration at $10^\circ$ tilt angle, $d/D = 0.96$ and $z/D = 0.38$ . . . . .	104
Figure 5.51: Change in mean torque of each rotor in square bearhug configuration with varying vertical rotor offset at $\alpha_R = 10^\circ$ . . . . .	105
Figure 5.52: Change of thrust of rotor 4 depending on tilt angle and vertical offset, square bearhug configuration with $d/D=1.2$ . . . . .	106
Figure 5.53: Change in mean thrust of each rotor in square diamond configuration with varying vertical rotor offset . . . . .	107
Figure 5.54: Change in mean torque of rotor 4 in diamond configuration with varying vertical rotor offset at $\alpha_R = 10^\circ$ . . . . .	108
Figure 5.55: Change in thrust of rotor 4 in the diamond configuration with tilt $-10^\circ$ (UPM) . . . . .	109
Figure 5.56: Velocity field in the plane of rotor 4, $\alpha_R = -10^\circ$ and $d/D = 0.96$ (UPM) . . . . .	109
Figure 6.1: Observed effects of aerodynamic interactions on produced thrust and induced torque . . . . .	115
Figure 6.2: Effect of the bearhug alignment on thrust of rotor 1 with varying advance ratio, $\alpha_R = 0^\circ$ , $d/D = 0.96$ (UPM) . . . . .	116
Figure 6.3: Tilt angle effect on torque components predicted by BET . . . . .	117
Figure 6.4: Aerodynamic characteristics of an airfoil at $0.7R$ blade section . . . . .	117
Figure 6.5: Effect of varying tilt angle on rotor thrust and torque at fixed rotational speed 5400 RPM and flight velocity 12.9 m/s for Aero-naut 12x6" . . . . .	118

# List of Tables

Table 2.1: Summary of computational methods . . . . .	12
Table 3.1: Input table for blade model . . . . .	28
Table 3.2: Summary of main computational settings . . . . .	30
Table 5.1: Thrust of a single rotor, 5400 RPM, $V_\infty=12.9$ m/s . . . . .	66



# Nomenclature

## Latin symbols

$a$	(m/s)	Speed of sound
$A_{ij}, B_{ij}, C_{ij}$	(1/m)	Influence matrix
$A_b$	(m <sup>2</sup> )	Total blade area
$B$	(-)	Tip-loss factor
$c$	(m)	Blade chord length
$\bar{c}$	(m)	Mean aerodynamic chord, $\bar{c} = 0.024 \text{ m}$
$c_d$	(-)	Sectional drag coefficient, $c_d = dD/c_{\frac{1}{2}}\rho U^2$
$c_l$	(-)	Sectional lift coefficient, $c_l = dL/c_{\frac{1}{2}}\rho U^2$
$C_p$	(-)	Pressure coefficient
$C_{M_R}$	(-)	Rotor rolling moment coefficient, $C_{M_R} = \overline{M_x}/\rho(\omega R)^2\pi R^3$
$C_{M_P}$	(-)	Rotor pitching moment coefficient, $C_{M_P} = \overline{M_y}/\rho(\omega R)^2\pi R^3$
$C_T$	(-)	Rotor thrust coefficient, $C_T = \overline{T}/\rho(\omega R)^2\pi R^2$
$C_Q$	(-)	Rotor torque coefficient, $C_Q = \overline{Q}/\rho(\omega R)^2\pi R^3$
$d$	(m)	Horizontal rotor spacing
$dD$	(N/m)	Sectional drag
$dL$	(N/m)	Sectional lift
$D$	(m)	Rotor diameter
$f$	(-)	Shape function
$F$	(N)	Aerodynamic force
$H$	(-)	Heavside function
$l$	(m)	Length of a vortex filament
$L$	(s/m)	Gain matrix
$n$	(-)	Number of panels
$M$	(-)	Mach number
$M_x$	(Nm)	Rotor rolling moment, positive to the right
$M_y$	(Nm)	Rotor pitching moment, positive nose-up
$N_b$	(-)	Number of blades



$P$	(W)	Power
$P_e$	(W)	Electric power
$Q$	(Nm)	Torque
$r$	(m)	Radial distance
$r_c$	(m)	Vortex core radius
$\vec{r}_v$	(m)	Position vector of a point on a vortex filament
$R$	(m)	Rotor radius
Re	(-)	Reynolds number
$t$	(s)	Time
$T$	(N)	Thrust
$T_{ij}$	(Pa)	Lighthill stress tensor
$U$	(m/s)	Velocity on the blade element
$U_P$	(m/s)	Velocity component normal to the rotor plane
$U_R$	(m/s)	Velocity component radial along blade in rotor plane
$U_T$	(m/s)	Velocity component parallel to the rotor plane
$v$	(m/s)	Velocity of a fluid
$v_m$	(-)	Mass flow parameter
$v_T$	(-)	Normalized total velocity at the rotor disc centre
$v_z$	(m/s)	Out-of-plane velocity component
$v_0$	(m/s)	Mean (uniform) induced velocity
$v_\Theta$	(m/s)	Tangential (swirl) velocity
$V_\infty$	(m/s)	Free stream velocity
$x_M$	(m)	Microphone array plane coordinate in $V_\infty$ direction
$x_P$	(m)	PIV plane coordinate tilted $-10^\circ$ from $V_\infty$
$X, Y$	(-)	Clustering parameters
$y_M$	(m)	Microphone array plane coordinate perpendicular to $V_\infty$
$y_P$	(m)	PIV plane coordinate perpendicular to $V_\infty$
$y^+$	(-)	Dimensionless wall distance
$z$	(m)	Vertical rotor spacing

## Greek symbols

$\alpha$	( $^\circ$ )	Angle of attack of the profile
$\alpha_R$	( $^\circ$ )	Tilt angle of the rotor plane
$\Gamma$	( $\text{m}^2/\text{s}$ )	Circulation
$\delta$	(-)	Dirac delta function

$\Delta$	(-)	Difference
$\zeta$	(1/s)	Vorticity
$\eta$	(%)	Motor efficiency
$\Theta$	(°)	Twist angle
$\lambda$	(-)	Inflow ratio
$\lambda_2$	(1/s <sup>2</sup> )	Flow field operator
$\mu$	(-)	Advance ratio
$\mu_D$	(m <sup>2</sup> /s)	Doublet strength
$\rho$	(kg/m <sup>3</sup> )	Free stream density
$\sigma$	(-)	Rotor solidity, $\sigma = A_b/\pi R^2$
$\sigma_S$	(m <sup>2</sup> /s)	Source/sink strength
$\nu$	(m <sup>2</sup> /s)	Kinematic viscosity
$\phi$	(°)	Inflow angle
$\Phi$	(m <sup>2</sup> /s)	Velocity potential
$\chi$	(rad)	Wake skew angle
$\psi$	(°)	Azimuth angle
$\omega$	(rad/s)	Angular velocity
$\Omega$	(RPM)	Rotational speed

## Subscripts

bound	Associated with bound circulation
isol	Result for isolated rotor in corresponding conditions
<i>c</i>	First harmonic cosine component
chord	Associated with chord panels
<i>i</i>	Induced
<i>k</i>	Associated with Kutta panel
<i>n</i>	Normal component
<i>r</i>	Radial component
<i>s</i>	First harmonic sine component
surf	Associated with surface panels
<i>t</i>	Tangential component
visc	Result including correction for viscous drag
wake	Associated with wake circulation
'	Fluctuation
0	Profile part

## Other symbols

—	Time-averaged value
$\vec{\cdot}$	Vector
[ ]	Matrix
{ }	Column vector
$\Delta$	Laplace operator
$\nabla$	Nabla (gradient) operator

## Abbreviations

1r	Isolated rotor test cases
2r	Two-rotor configuration test cases
4r	Four-rotor configuration test cases
4r <sub>z</sub>	Four-rotor configuration test cases with vertical spacing
2D	Two-dimensional
3D	Three-dimensional
AIAA	American Institute of Aeronautics and Astronautics
APSIM	Aeroacoustic prediction system based on integral methods
BEM	Boundary element method
BEMT	Blade element momentum theory
BET	Blade element theory
BL	Boundary layer
BOS	Background oriented schlieren
BPF	Blade passing frequency
BVI	Blade vortex interaction
BWI	Blade wake interaction
CEAS	Council of European Aerospace Societies
CF	Clustering factor
CFD	Computational fluid dynamics
CHIEF	Combined Helmholtz integral equation formulation
CIRA	Italian Aerospace Research Center
CORAL	Comprehensive rotorcraft analyses lab
CPU	Central processing unit

---

CU	Carleton University
DEHS	Di-Ethyl-Hexyl-Sebacate
DLR	German Aerospace Center e.V.
EPOS	Easy to use positioning system
ERF	European Rotorcraft Forum
FOV	Field of view
FW-H	Ffowcs Williams-Hawkings
IAG	Institute of Aerodynamics and Gas Dynamics
LE	Leading edge
MPI	Message passing interface
N-S	Navier-Stokes
NACA	National Advisory Committee for Aeronautics (now NASA)
NASA	National Aeronautics and Space Administration
NTUA	National Technical University of Athens
MAV	Micro air vehicle
MEMS	Micro-electrical-mechanical systems
(OA)SPL	(Overall) sound pressure level
OB	Off-body
ONERA	French Aerospace Lab
PANGEN	Panel generation code
RHS	Right-hand side
RM3	Roma Tre
PP	Pitt and Peters inflow model
PIV	Particle image velocimetry
PUMA	Potential unsteady methods for aerodynamics
RC	Remote control
RPM	Revolutions per minute
RTG	Rotor test facility Göttingen
SST	Shear stress transport
TE	Trailing edge
UAM	Urban air mobility
UAV	Unmanned aerial vehicle
UPM	Unsteady Panel Method
(U)RANS	(Unsteady) Reynolds-Averaged Navier-Stokes
VTOL	Vertical take-off and landing
WENO	Weighted essentially non-oscillatory



# 1 Introduction

Over the past decade, multicopters have dominated the unmanned aerial vehicles (UAV) market, finding applications in diverse fields such as surveillance, videography or remote site inspection [117, 129]. Thanks to their vertical take-off and landing (VTOL) capabilities together with high manoeuvrability, multirotors combine the advantages of fixed-wing aircraft and unmanned helicopters. However, it is their ease of use and maintenance, which has left the competition behind and made them the first choice of hobbyists and professionals alike. Ever-increasing interest indicates even a broader use of multicopters in the coming years. Nevertheless, this will not happen without addressing their greatest drawbacks: low efficiency, which results in short flight times, and high noise emissions, which limit their use in urban areas. The answer to both of these problems lies in studies on the aerodynamic interactions between the rotors, leading to a better understanding of how to minimise the negative effects and exploit the positive ones.

Rotor-rotor interactions have an impact on the loads generated and, as a result, neither the performance, nor the noise levels of a multicopter is a simple, linear function of the number of rotors. The interaction effects intensify when wakes propagate close to the rotor plane, as is typical in forward flight. As much of the UAV's operational time can be spent in such conditions, the study of aerodynamic interactions is a key to maximising its performance. For this purpose, a number of variables must be taken into account with the tilt angle of the rotor plane or design choices such as the rotor hub spacing having a major influence. The abundance of possible parameters affecting the rotor-rotor interactions is not the only challenge in predicting the performance of a multicopter. Traditional computational methods have been developed for full-size aircraft, which means that their application to small-scale rotor simulations requires a separate investigation.

The majority of UAV research in the recent years has been devoted to the four-rotor aircraft being the most popular representative of multicopters. So-called quadrotors or quadcopters, are found in two configurations - diamond (also known as plus/'+') or square (cross/'X'), depending on the rotors' alignment relative to the flow direction.

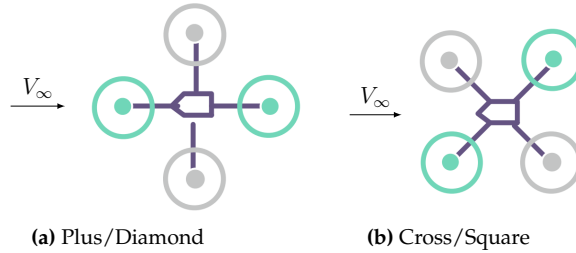


**Figure 1.1:** Quadrotor configurations after [117]

In both cases two pairs of counterrotating rotors, shown in different colours in Fig. 1.1, are used to compensate for the total torque. Recent studies have shown that the diamond configuration shows lower control authority than a cross quadrotor [105, 159], yet it has a significant aerodynamic advantage [12, 61, 64, 102]. Additionally, it has been demonstrated that raising the back rotors in the cross configuration effectively improves their performance as they consequently operate above the wake of the front rotors [59, 85, 144]. It may come as a surprise then that the UAV market is dominated by the traditional cross configuration quadrotors, as in Fig. 1.2a with one of the most popular RC (remote control) models for the year 2023 [136] being equipped with undermounted back rotors (Fig. 1.2b). The existing designs prioritise technical solutions such as a camera placement with an unobstructed field of view, which is more problematic for the diamond quadrotor, or the space for folding arms.

Decisions about aerodynamic design, whether making it the goal for efficiency improvement or a deliberate compromise in favour of other factors, require efficient and robust prediction methods. Navier-Stokes solvers are too computationally expensive and therefore impractical in the early design stages when a wide range of parameters need to be considered. On the other hand, the assumptions of lower-fidelity solvers may not accurately represent the specifics of small rotor aerodynamics.

Therefore, the objective of the present work was to provide a comparison of aerodynamic solvers with different fidelity levels, with a special focus on a potential panel method, for quadrotor flight applications. The basis of the study was an analysis of the applicability of the applied methods in predicting both mean loads and transient forces serving as an input for aeroacoustic tools for an isolated rotor. The following quadrotor analysis considered variations in the rotor plane tilt angle and both horizontal and vertical spacing between the rotors, including cases with particularly high interactions such as nose-up tilt or close rotor positioning with overlapping blades. Diamond and square configurations were analysed to provide an overview of the



(a) DJI Phantom 4 Pro [38]



(b) DJI Mavic 2 Pro [147]

**Figure 1.2:** Examples of the most popular quadcopters in 2023

different interaction effects depending on the mutual rotor alignments. This allows the results to be generalised to flight in side wind conditions, for which, from an aerodynamic point of view, one configuration can effectively change into the other. The two-rotor system cases served as an intermediate step to better understand the interaction effects and possible solver limitations. The cross-validated computational results were compared with experimental data. As a result, the work provided answers to the following questions:

- *Can a potential free wake solver be applied for aeroacoustic and aerodynamic simulation of a small-scale UAV rotor?*
- *Is a potential solver applicable for estimation of interaction effects for a quadrotor in forward flight?*
- *What are the types of aerodynamic interactions in quadrotor configurations?*





## 2 Fundamentals and state of the art

A rotor in forward flight generates unsteady loads and complex vortex structures that interact with each other and with the blades and therefore represents a challenging state for aerodynamic modelling. Depending on the purpose and resources available, certain simplifications can be made to reduce the computational time together with modelling effort. However, this comes at the cost of loss of detail and universality of the solution. In practice, lower fidelity methods for performance prediction provide high accuracy results as long as the assumptions made can be applied to the analysed aerodynamic conditions. For this reason, it is important to have an initial knowledge of the simulated cases and to understand the possible limitations of a selected method in reproducing them.

### 2.1 Rotor in forward flight

Hover and vertical climb represent basic examples of rotor aerodynamics, where the rotor ideally operates in axisymmetric flow conditions. The local velocity and thus the loads on the blades vary only radially due to the rotational motion. Nevertheless, for the initial performance estimation it is sufficient to assume uniform inflow for axial flow conditions. The spanwise variation of the loads determines the strengths of the vortices generated along the blade with a sharp pressure gradient at the tip causing a concentrated, rolled-up blade tip vortex.

During the forward flight the rotor operates in an edgewise flow, which is unnatural for its initial design. A non-axial inflow results in a complex, three-dimensional velocity field. A propulsive force required for forward flight of a rotorcraft is obtained from a horizontal thrust component dependent on the rotor plane tilt angle  $\alpha_R$ . According to the sign convention adopted within this thesis negative values of  $\alpha_R$  correspond to nose-down rotor tilt, whereas positive  $\alpha_R$  stand for nose-up tilt resulting in braking force (Fig. 2.1). The velocity components normal and parallel to the rotor plane can be defined in a dimensionless form as inflow ratio  $\Lambda$  and advance

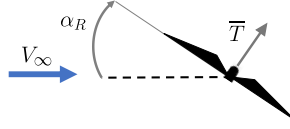


**Figure 2.1:** Tilt angle sign convention

ratio  $\mu$  respectively:

$$\Lambda = \frac{v_i - V_\infty \sin \alpha_R}{\omega R}, \quad (2.1)$$

$$\mu = \frac{V_\infty \cos \alpha_R}{\omega R}. \quad (2.2)$$

As the blade rotates edgewise to the free stream direction, the local velocities become the sum of the rotational and forward motion. As a result, the flow on the rotor is not axisymmetric, i.e. depends on the azimuthal position of the blade. As shown in Fig. 2.2a two sides of the rotor can be defined with respect to the azimuth angle  $\Psi$ . The advancing side of the rotor ( $0^\circ < \psi < 180^\circ$ ), where the velocities add produces more thrust, while the retreating side ( $180^\circ < \psi < 360^\circ$ ) is characterised by reduced total velocity resulting in lower load. In forward flight wake vortices propagate downwards with the induced flow but are also carried rearwards in the free stream direction as shown in a simplified manner in Fig. 2.2b. Additional complexity of the shed wake arises from the cyclic load variation and aerodynamic interactions. The proximity of wake filaments causes tip vortices to roll-up into ‘super vortices’ along the wake edges [53]. Additionally, the wake develops close to the rotor plane, making blade-vortex interactions (BVI) more likely.

A non-uniform inflow typical for moderate forward flight velocities ( $\mu > 0.15$ ) can be approximated with linear (first harmonic) models [27, 29]. In their simplest form, the models capture upwash at the disc front and the decrease of the induced velocity towards the back of the rotor; however, some of them consider both longitudinal and lateral inflow variation. It has been shown that the induced velocity strongly depends on the wake skew angle  $\chi$  (Fig. 2.2b) defined as:

$$\tan \chi = \frac{\mu}{\Lambda}. \quad (2.3)$$

The mean value of  $\chi$  used a centre value in linear models can be found iteratively depending on thrust coefficient  $C_T$  based on a uniform induced velocity  $v_0$  formula

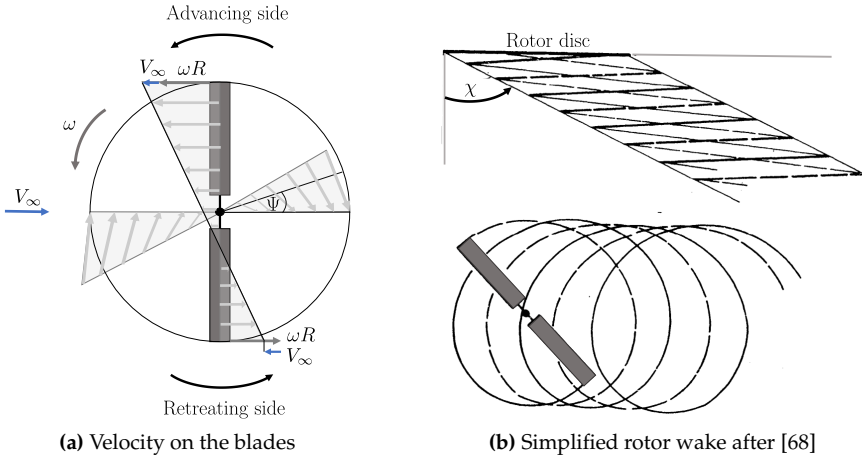


**Figure 2.2:** Rotor in forward flight

by Glauert [51]:

$$v_0 = \frac{C_T}{2\sqrt{\mu^2 + \lambda^2}}. \quad (2.4)$$

The flow characteristics in forward flight have an influence on the rotor aeroacoustics. Rotor aerodynamic noise can be divided into periodic components occurring at harmonics of the blade passing frequency and broadband noise coming from random and non-periodic sources (Fig. 2.3). A major part of the generated noise comes from the periodic components produced by the fluctuating forces on the blades. Another rotational noise component is caused by a non-uniform pressure distribution across the airfoil as a blade of a certain thickness moves through the air. However, except for high tip speeds and in-plane observers, the thickness noise is relatively small compared to that produced by thrust and torque. In forward flight the velocity on blades is asymmetric, giving rise to harmonics of the blade passing frequency. Additionally, blade interactions with vortices shed from preceding blade or adjacent rotor(s), which are likely in forward flight conditions, cause impulsive distortion of the loads generated and add to the harmonic noise components. This in turn, makes an acoustic signature much more complex and more difficult to model. It has been shown that BVI effects are the strongest when the tip vortex passes parallel to the blade, which is the case at positive rotor tilt angles or during descending flight [127].

In contrast to BVI events, blade wake interactions (BWI) represent a considerable source of low frequency broadband noise. In this case the noise is generated by

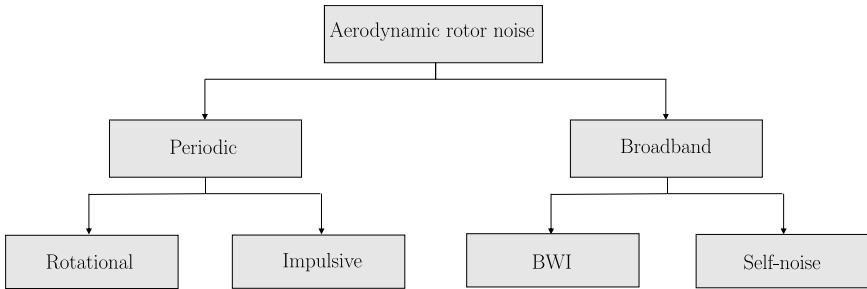


**Figure 2.3:** Aerodynamic rotor noise sources based on [20, 63, 98]

turbulence resulting from interaction with the shear layer [21]. The highest frequencies of the noise spectra are dominated by self-noise depending on the boundary layer characteristics. Typically this type of noise is associated with turbulence at the blade trailing edge causing random force fluctuations [126]. Other mechanisms include laminar vortex shedding, tip vortex formation or flow separation [22].

### 2.1.1 Specifics of small rotor aerodynamics and aeroacoustics

Multicopters have gained popularity due to their vertical take-off and landing (VTOL) and hover capabilities allowing operation in urban areas. Nevertheless, depending on the mission profile, the operation time of small UAVs can be mostly spent in forward flight [138, 152]. Therefore, the optimisation of aerodynamic design with respect to flight in edgewise flow could help to meet the ongoing challenge of increasing the endurance of electric UAVs. On the other hand, the developing UAV market is severely constrained by the public acceptance of the noise. While most multicopters today are powered by electric motors, it is the rotor that represents UAV's main noise source [55, 60].

Although extensive studies have been conducted on rotors operating under axial-flow conditions [36, 54, 107, 108, 148], their results are not applicable to forward flight with higher advance ratios. At the same time, the mechanisms acting on a small rotor under such conditions are not yet fully understood and cannot be directly derived from the full-size helicopter rotor. The main difference lies in the blade planform shape, as multicopters are typically driven by fixed-pitch blades with nonlinear twist distribution and strong chord variation along the span [36]. The control of a vehicle is realised only by adjusting the rotational speeds of the selected rotors, thus generating forces and associated moments for the desired manoeuvre. Using a quadrotor as an example, forward flight is achieved by the difference in RPM between the front

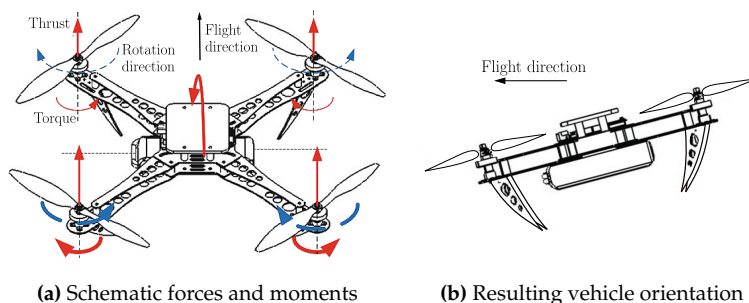


**Figure 2.4:** Forward flight of a quadrotor after [117]

and back rotors resulting in a nose-down tilt of the vehicle, as shown in Fig. 2.4. The variation of inflow angles typical of UAV rotor operation has a significant influence on the forces and moments produced [137], following nonlinear dependencies [74]. The corresponding effects are also reflected in the acoustic signature of the rotor. Intense blade vortex interactions and separation occurring at higher nose-up tilt angles give rise to broadband noise components as shown by Lößle et al. [91].

The use of rigid blades indicates another special feature of multicopter rotors, which is the lack of compensation for the advancing and retreating side effects. In the case of a hinged helicopter rotor the imbalance of forces across the rotor disc in forward flight is reduced by cyclic flapping and feathering blade motion, otherwise bending stresses at the blade root and large rolling moments would make the flight impossible [46]. For small-scale rotors the uncompensated forces do not affect the mechanics and flight dynamics to the same extent. At the same time, the use of rigid blades makes the control more straightforward and greatly reduces mechanical complexity. Nevertheless, the imbalance of forces has an impact on the wake produced, with the strong advancing side vortex propagating steeper downwards and the weaker retreating side vortex remaining closer to the rotor plane. An accurate representation of this effect is necessary to capture interactions between multicopter rotors. Wake asymmetry increases with higher thrust fluctuations, which is the case for lower rotor tilt and higher advance ratio as shown by Krebs et al. [79] (Fig. 2.5). Cerny et al. [28] investigated the complex three-dimensional flow on the rigid blades caused by non-axial inflow. Effects such as flow separation and radial flow become periodic under such conditions, resulting in increased pitch and yaw moments.

Due to velocity summation on the rotor blades in forward flight (Fig. 2.2a), a helicopter performance is limited by the transonic effects likely to occur on the

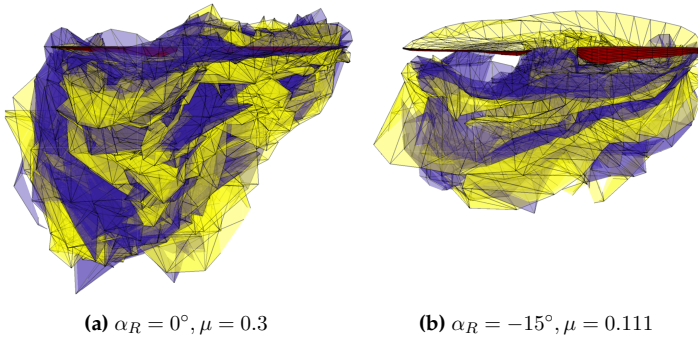


**Figure 2.5:** Asymmetry of the rigid rotor's wake in forward flight viewed from the front [79]

advancing side of the rotor. In contrast, a typical advancing side tip Mach number of a small UAV does not exceed 0.3 [158], making its flight free from detrimental shock wave effects and high-speed impulsive noise sources. Nevertheless, additional complexity arises from Reynolds scaling between helicopter rotors ( $Re$  usually of the order of  $10^6$ ) and UAV rotors, which typically operate at  $Re$  in the range of  $10^4 - 10^5$  [158] or  $10^3 - 10^4$  in the case of micro air vehicles, characterised by maximum dimensions of up to 15 cm [1]. Mechanisms such as separation bubbles, laminar boundary layer separations and transitions typical of low Reynolds number flows lead to nonlinear trends even before the critical angle of attack is reached and result in performance degradation. Accordingly, extensive studies of small rotors' performance [17, 35, 36] indicate that UAV rotors exhibit reduced efficiency compared to larger models. Moreover, it was demonstrated that small rotors are sensitive to changes in the local Reynolds number, and thus Reynolds scaling plays an important role in the flow models [35, 56, 99]. The MAV rotor study by Ramasamy et al. [123] showed experimentally that vortex sheets shed by a small rotor are relatively thicker and more turbulent, which contributes to efficiency losses. Additionally, the viscous effects were found to affect the formation and roll-up of the vortices, resulting in increased tip vortex core sizes.

The complexity of low Reynolds number flows is also reflected in small rotors' aeroacoustics [52]. Although the main noise sources remain the same as those for helicopter rotors, the balance between tonal and broadband noise contributions in the acoustic pressure signature can be considerably affected. The low Reynolds number effects described above, together with enhanced wake interactions, increase the unsteadiness at the blade edges and thereby amplify higher frequency noise

components. As a result, noise prediction for small-scale rotors poses a challenge for traditional methods developed for fully turbulent flows [24].

Last but not least, the nearness of rotors in multicopters implies strong aerodynamic interactions, atypical for helicopter configurations. Wakes of neighbouring rotors mutually affect the rotor inflow and direct blade-vortex interactions lead to rapid local changes in the loads generated and thus represent a significant noise source. As a result, neither the aerodynamic performance nor the aeroacoustics of a multicopter is a simple function of the number of rotors. All things considered, the choice of an appropriate prediction method is challenging in terms of adequately estimating the performance of an isolated small-size rotor as well as capturing the interactions between the rotors in a full configuration.

## 2.2 Low- and mid-fidelity methods for forward flight calculations

Although URANS simulations provide the highest reliability for a wide range of conditions, the general experimental trends can be successfully captured by low-fidelity tools [138]. Methods based on potential flow represent a complexity level between blade element theory and RANS solvers. Their great advantage is the ability to simulate unsteady conditions, while ensuring time efficiency [79]. Potential solvers usually include a free wake method, as described in [88] but can be also extended with a viscous particle wake [135], couplings with BL (boundary layer) codes or post-processing corrections for viscosity and compressibility. A comparison summarising main features of the methods described in the following sections can be found in Table 2.1.

### 2.2.1 Blade element theory

In the simplest way, the rotor can be thought of as a disc that generates thrust by driving a mass of air through its plane. The relationship between the force produced and the velocity induced to the flow in the process can be found using the laws of conservation of mass, momentum and energy. This approach, called a momentum theory, requires an additional empirical correction to be applied for forward flight cases [138]. A solution of higher complexity, including radial and azimuthal load distribution and consideration of different blade designs, can be obtained with the blade element theory (BET).



BET	Potential methods + Free wake			N-S CFD	
<ul style="list-style-type: none"> <li>✓ Easy implementation</li> <li>✓ Viscosity and compressibility effects included in airfoil characteristics</li> <li>✗ Limited to 2D quasi-steady flows, no wake interference effects resolved</li> <li>✗ Inflow model and airfoil performance data necessary</li> <li>✗ Corrections to airfoil data necessary for post-stall regime</li> </ul>	<ul style="list-style-type: none"> <li>✓ No volume grid</li> <li>✓ Unsteady flows</li> <li>✓ Captures mutually and self-induced vortex effects and BVI</li> <li>✗ Corrections needed for compressibility and viscous effects: profile drag, separation, empirical models for vortex core, vortex decay,...</li> <li>✗ Free wake sensitive to numerical instabilities</li> </ul>	<ul style="list-style-type: none"> <li>✓ Limited number of unknowns, easy implementation</li> <li>✗ Limited in capturing 3D effects, simple geometries</li> <li>✗ No thickness effect</li> </ul>	<ul style="list-style-type: none"> <li>✓ Captures 3D flow effects</li> <li>✓ More accurate geometry representation</li> <li>✗ No thickness effect</li> </ul>	<ul style="list-style-type: none"> <li>✓ Thickness effect included, easy coupling with BL codes</li> <li>✓ Arbitrary geometries including non-lifting bodies</li> <li>✗ High number of unknowns</li> </ul>	<ul style="list-style-type: none"> <li>✓ High accuracy and universality with turbulence and transition effects included</li> <li>✓ Complex geometries, flexibility in boundary conditions</li> <li>✗ Grid-based and prone to numerical dissipation</li> <li>✗ Complex modelling including turbulence models, mesh generation, ...</li> <li>✗ Highly computationally expensive</li> </ul>

Longer computational time and higher fidelity →

**Table 2.1:** Summary of computational methods

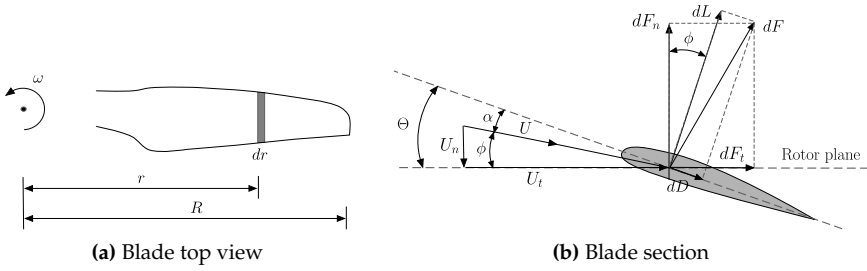


**Figure 2.6:** Velocities and forces on a blade element

In the BET method, as shown in Fig. 2.6, the blade is divided into spanwise sections, for which the lift and drag forces are calculated separately using the following expressions:

$$dL = \frac{1}{2} \rho U^2 c_l dr, \quad (2.5)$$

$$dD = \frac{1}{2} \rho U^2 c_d dr. \quad (2.6)$$

The lift and drag coefficients,  $c_l$  and  $c_d$ , can be found in the aerodynamic characteristics of the airfoils as a function of the angle of attack  $\alpha$ , as well as Reynolds and Mach numbers. In turn, the angle of attack of a section depends on the blade pitch  $\Theta$  and inflow angle  $\phi$  according to the following relationship:

$$\alpha = \Theta - \phi. \quad (2.7)$$

For a fixed-pitch rotor the value of  $\Theta$  is known directly from the geometrical twist of the blade. On the other hand, calculation of the inflow angle  $\phi$  requires an estimation of the out-of-plane  $U_n$  and in-plane  $U_t$  velocity components:

$$\phi = \arctan \frac{U_n}{U_t}, \quad (2.8)$$

which means adding a loop with an external induced velocity model to the solution process. Forces acting perpendicular and parallel to the rotor disc can be then expressed relative to the inflow angle:

$$dF_n = dL \cos \phi - dD \sin \phi, \quad (2.9)$$

$$dF_t = dL \sin \phi + dD \cos \phi \quad (2.10)$$

and the resulting incremental thrust  $dT$  and torque  $dQ$  depends on the number of blades  $N_b$ :

$$dT = N_b dF_n, \quad (2.11)$$

$$dQ = N_b dF_t r. \quad (2.12)$$

In forward flight, the velocity on the blade is a function of azimuth, and thus the calculation of loads on each section must be repeated for a range of azimuthal positions. The resulting loads on the rotor disc are the sum of  $dT$  and  $dQ$  along the blade for the entire rotation.

Of the aerodynamic tools described in the literature, those based on the blade element theory are the simplest and most time-efficient, yet for moderate flight conditions they show accuracy comparable to higher-fidelity solvers. For this reason, BET tools are commonly used for an initial load and noise estimation during the design process [55, 148]. However, the quality of BET calculations depends on the accuracy of the airfoil polar data, which is particularly challenging at low Reynolds numbers [13, 52]. At low advance ratios a fixed-pitch rotor typically operates partially in the post-stall regime, which means that airfoil data corrections are required to properly capture the rotor aerodynamics. These include extrapolation models for higher angles of attack and methods to recreate rotational effects [94].

Another factor strongly affecting the solution is the applied inflow model. A combination of blade element and momentum theory (BEMT) offers good agreement with experimental results for axial flow conditions [54]. However, forward flight calculations, for which a simple momentum theory is no longer applicable, usually require coupling the BET method with more complicated inflow models taking into account non-uniform velocity distribution across the rotor disc [32, 106, 111]. Nevertheless, the reduction in computational cost compared to the higher-fidelity tools remains significant.

## 2.2.2 Potential and vortex methods

BET methods, even though valuable for initial estimates, are limited to 2D, quasi-steady flow effects and do not capture the wake influence on the generated loads, which is particularly important in forward flight. The wake complexity in such conditions including mutual interactions between vortices or interactions between vortices and blades cannot be reconstructed with prescribed wake models. This means that, in order to properly represent the wake, the propagation of vortices must be included in the solution process. High-fidelity CFD methods provide accurate,

unsteady results by directly solving entire flow fields. On the other hand, even these methods are not error-free, with numerical vorticity dissipation being a prime example. The issue arising from numerical discretization can be avoided by using grid-free tools called vortex methods.

The assumption of incompressible flow, well justified especially in case of small rotor flight conditions, reduces the Navier-Stokes vorticity transport equation to the following form in a Lagrangian framework:

$$\frac{D\vec{\zeta}}{Dt} = (\vec{\zeta} \cdot \nabla)\vec{v} + \nu\Delta\vec{\omega}, \quad (2.13)$$

where  $\vec{\zeta}$  stands for vorticity,  $\vec{v}$  is the velocity of a fluid particle and  $\nu$  is kinematic viscosity. The left-hand side term of the equation above describes convection, while right-hand side terms represent strain (vortex stretching) and viscous diffusion, respectively. For many practical applications, wake structures produced by the viscous effects can be expected to be much smaller in scale than those caused by potential (inviscid, incompressible, irrotational) flow. As shown next, the assumption of potential flow ensures a significant reduction in the computational effort while providing an unsteady solution. First of all, the wake can be represented by discrete vortex filaments moving as material lines. This property, used in vortex methods, allows the behaviour of vortices in a simple convection form:

$$\frac{d\vec{r}_v}{dt} = \vec{v}, \quad \vec{r}_v(t=0) = \vec{r}_{v0}, \quad (2.14)$$

where  $\vec{r}_v$  is the position vector of the point on the vortex filament and  $\vec{r}_{v0}$  its initial position vector. The above equation is the basis of commonly used free vortex wake model, where, as the name indicates, vortex filaments propagate freely and deform according to the local velocity field at each time step. This allows the representation of complex wake behaviour, such as mutually and self-induced vortex effects or blade-vortex interactions (BVI). The estimation of the velocity field determining wake propagation is calculated by applying the Biot-Savart law. The law states in the generalised form that the velocity  $\vec{v}$  induced by segments  $d\vec{l}$  of the vortex filament at an arbitrary point at a distance  $\vec{r}$  can be described as:

$$\vec{v} = \frac{\Gamma}{4\pi} \int \frac{d\vec{l} \times \vec{r}}{|\vec{r}|^3}, \quad (2.15)$$

depending on the vortex circulation  $\Gamma$ . Viscous effects of vortex decay and growth due to diffusion are usually accounted for by additional empirical models and were

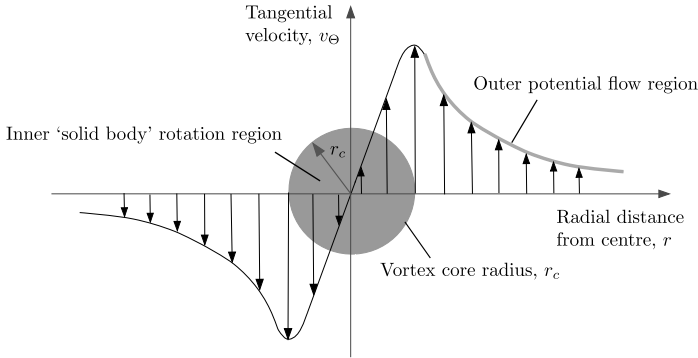


**Figure 2.7:** Scheme of tangential (swirl) velocity profile of the tip vortex after [88]

shown to influence rotor performance prediction [14]. The filament straining effect can be represented as a correction to the Biot-Savart calculations, yet in many cases its impact is relatively small [89]. Another issue requiring external modelling is the flow representation in the vortex core, where the vortex resembles solid body rotation rather than potential flow (Fig. 2.7). The tangential (swirl) velocity  $v_\Theta$  of the potential vortex is expressed as:

$$v_\Theta = \frac{\Gamma}{2\pi} \frac{1}{r}, \quad (2.16)$$

which reaches infinity for  $r \rightarrow 0$ . This property, apart from being untrue for real viscous flows, causes stability issues in cases where wake filaments are close together or cross solid bodies, e.g. for blade-vortex interactions. For this reason, it is common practice to describe the flow inside the vortex core using models known from the literature, such as the examples presented in Fig. 2.8 [14]. The choice of a vortex model and corresponding vortex core size can have a considerable impact on the results for cases with high wake interactions [133, 163]. At the same time a balance between exact modelling and numerical stability has to be considered [84].

The wake shed by the blade in the free wake model is divided into trailed vorticity, caused by the variation of lift (circulation) along the blade span, and shed vorticity, resulting from the change of lift with time (azimuthal step), as shown in Fig. 2.9. A rolled-up tip vortex resulting from a strong circulation gradient at the blade tip plays a major role in the model as it has the greatest impact on the rotor aerodynamics as well as the largest contribution to the induced flow. In Fig. 2.9, the wake is coupled with the most basic, two-dimensional blade model, called a lifting line. In this approach the blade is represented by horseshoe vortices distributed spanwise along the quarter-

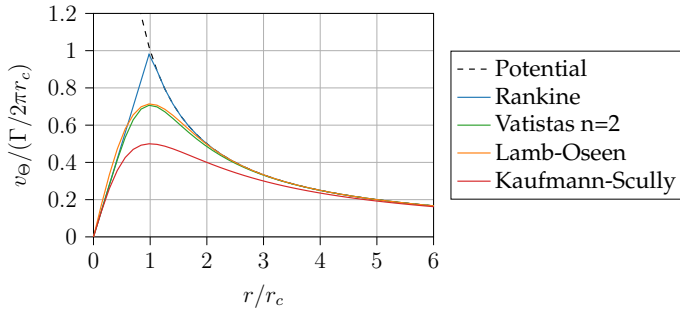


**Figure 2.8:** Examples of vortex core models

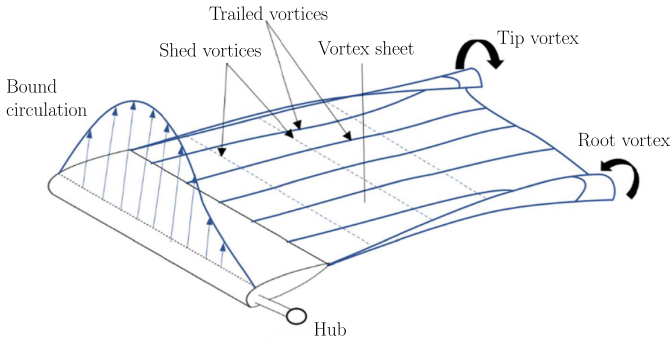


**Figure 2.9:** Blade wake scheme after [82]

chord. The relationship between the bound circulation  $\Gamma$  and the lift produced per unit span is then expressed by the Kutta-Joukowski theorem for the blade section  $dr$ :

$$dL(r) = \rho U(r) \Gamma_{\text{bound}}(r) dr. \quad (2.17)$$

As only a single vortex element is applied to each blade section, the ability of a lifting line method to reproduce 3D flows is severely limited. The chordwise flow distribution can be captured by the lifting surface model, traditionally implemented as a vortex lattice method (Fig. 2.10a). In this case the blade is modelled as a vortex sheet along the mean blade surface, which allows representation of geometrical properties such as blade sweep and camber. However, thickness effects and flow around more complicated geometries including non-lifting bodies can only be resolved using panel methods [69]. Besides more accurate flow representation, reproducing body thickness has the additional advantage as the code can be coupled with boundary layer solvers

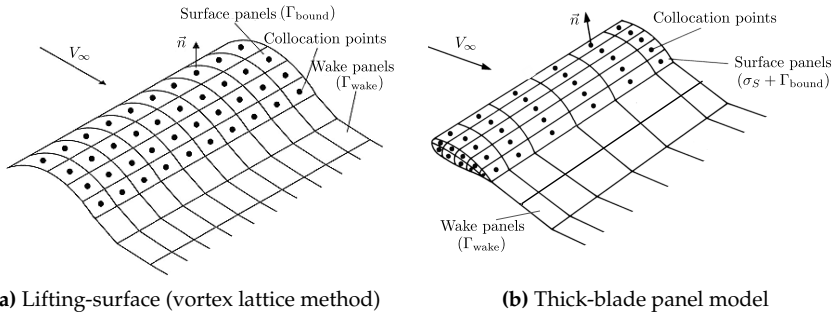


**Figure 2.10:** Blade models with free wake based on [83]

to include viscous effects, or with aeroacoustic tools to estimate the thickness noise.

The base principle of presented potential methods is the recreation of flow around a body using a combination of elementary solutions to the Laplace's equation. According to the potential theory, the velocity field can be then described as a gradient of a scalar function  $\Phi$ :

$$V = \nabla\Phi. \quad (2.18)$$

In panel methods the blade thickness can be modelled using a distribution of sources and sinks on the upper and lower blade surfaces, while lift is reproduced with vortices usually applied to the chord or camber surface (Fig. 2.10). Alternatively, a distribution of doublet panels can be used as an equivalent to vortex filaments, as described by Wie et.al. [149]. The numerical solution process then consists of determining the singularity strengths using a boundary condition of no flow through the body. In a general form, the no-penetration condition set at collocation points reduces the problem to solving a set of linear, algebraic equations for the unknown strengths  $\gamma$ :

$$[A_{ij}]\{\gamma_i\} = \{RHS_i\}. \quad (2.19)$$

The influence coefficient matrix  $A_{ij}$  describes effectively the normal velocity induced at the  $j$ th collocation point by the singularity strength  $\gamma_i$  on the  $i$ th blade element and depends only on the blade geometry. Remaining velocity components are collected in the right-hand side vector matrix  $RHS$ . The resulting distribution of strengths on the blade is directly linked to the strengths of the vortices in the shed wake.

A bridge between the blade and wake model, ensuring a unique and physical flow around the trailing edge, is added to the solution process with the Kutta condition. It has been shown that a proper specification of the Kutta condition is crucial

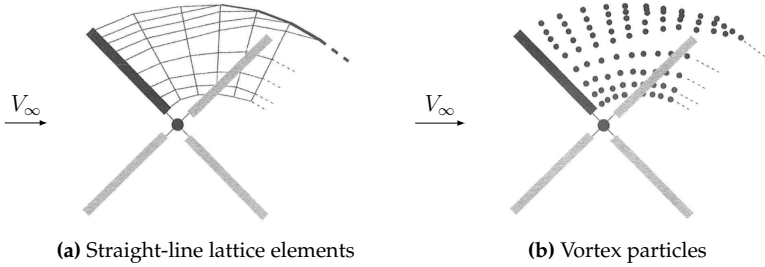


**Figure 2.11:** Vortex wake representations including tip vortex roll-up [88]

because of its significant impact on the resulting circulation distribution [9, 62]. Usual implementations assume tangential flow or continuous pressure at the trailing edge.

After computing the singularities' strengths and the resulting velocity field, potential methods can be further used for secondary computations such as estimation of loads and moments. A common practice is to determine the pressure coefficient  $C_p$  by means of the Bernoulli equation for unsteady flow:

$$C_p = 1 - \frac{v_t^2}{V_\infty^2} - \frac{2}{V_\infty^2} \frac{\partial \Phi}{\partial t}, \quad (2.20)$$

where  $V_t$  is the velocity component tangential to the body surface.

As an alternative to vortex lines consisting of straight elements, the wake can be represented as vortex particles 'blobs' (Fig. 2.11). The advantage of this approach is the lack of connectivity between vortex elements, which allows improved modelling of wake mixing and viscous effects [6, 143]. The viscous particle methods with the examples described in [6, 162] solve for all terms of Eq. 2.13.

### 2.2.3 Aeroacoustic computations

The loads evaluated by the described aerodynamic methods can be used as an input for aeroacoustic tools based on various forms of the Ffowcs Williams and Hawkings method [43]. The FW-H equation was derived from the Navier-Stokes equations for the density fluctuation  $\rho'$  in a waveform and is considered to be the most appropriate approach for the calculation of rotor noise. Assuming an impenetrable body surface described with  $f(\vec{x}, t) = 0$ , the classical form of the equation can be written as:

$$\frac{\partial^2 \rho'}{\partial t^2} - a^2 \frac{\partial^2 \rho'}{\partial x_i^2} = \frac{\partial^2}{\partial x_i \partial x_j} [T_{ij}] H(f) + \frac{\partial}{\partial t} [\rho_0 v_n \delta(f)] - \frac{\partial}{\partial x_i} [l_i \delta(f)], \quad (2.21)$$



where  $a$  stands for the speed of sound. The right-hand side of the equation contains the sources terms responsible for the noise generation, which are consecutively: a quadrupole term as a product of the fluctuating Reynolds stresses in the Lighthill tensor  $T_{ij}$ , the thickness noise generated by the normal surface velocity  $V_n$  and the loading noise depending on the aerodynamic forces  $l_i$ . Due to the Dirac delta function  $\delta(f)$ , the last two terms only act on the blade surface, while the quadrupole term with the Heavside function  $H(f)$  has a non-zero value in the outside flow. Unlike the linear terms, which generate tonal noise, the quadrupole (vortex) term is likely to contribute to the broadband noise at high frequencies due to velocity fluctuations caused by small-scale turbulence. Nevertheless, the quadrupole term is often neglected in low Mach number applications [57]. While the thickness noise contribution is mainly dominant in the rotor plane due to its highly directional, monopole nature, the loading noise represents a dipole source, which is significant out of the rotor plane.

A common implementation of Eq. 2.21 in the aeroacoustic tools involves the use of the integral formulation from the Green's function solution developed by F. Farassat [44], presented in a discretised form in [45]. The Farassat formulation describes thickness and loading noise terms, collectively known as rotational noise, for an observer at a distance  $r$  from the surface and includes near-field and far-field terms in the order of  $1/r^2$  and  $1/r$  respectively. The input includes the description of the body geometry and motion together with loads described as blade surface pressure or sectional forces depending on the aerodynamic solver. As an alternative to a physical blade surface, the FW-H equation can be solved on a permeable integration surface. This approach has a significant advantage for cases where a larger contribution from nonlinear terms is expected as all sources enclosed by  $f$  can be resolved by surface terms without computationally expensive volume integration [18]. A disadvantage of this approach is the need for a high accuracy solution of the flow field from an aerodynamic solver.

## 2.3 Aerodynamic interactions in multirotor configurations

The close proximity of the rotors, typical of multicopter configurations, indicates that many of the UAV's flight states are affected by rotor-rotor interactions. As shown by Niemiec et al.[105] traditional low-fidelity tools such as BET can be used for initial estimation of the multicopter dynamics. However, their accuracy of aerodynamic and aeroacoustic prediction is severely compromised by the neglect of interactions

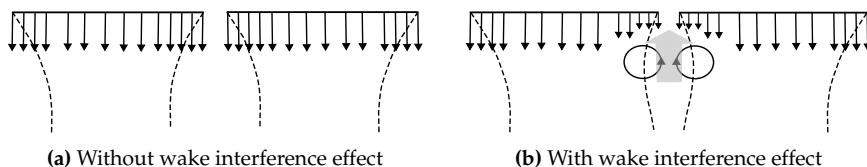


**Figure 2.12:** Schematics of wake interference effect between two rotors in hover after Lee et al. [86]

between rotor wakes [5]. For this reason, given the low density of current batteries and noise emission restrictions, a proper prediction of interaction effects is a key issue for multicopters and requires the use of more sophisticated modelling tools.

Even before the popularity of small UAVs, research into interactional aerodynamics was of great importance for co-axial or tandem helicopter configurations. It has been shown that the performance of co-axial or partially overlapped rotor systems in hover can be evaluated using modified BEMT tools [88, 134]. However, this approach does not take into account the influence of the lower rotor on the upper rotor and, above all, ignores the effects occurring for rotors positioned close side-by-side, out of the slipstream of the neighbouring rotor(s). Contrary to the momentum theory, such an alignment cannot be considered as a system of isolated rotors due to an upwash induced by tip vortices in the inboard region (Fig. 2.12). At the same time, its influence cannot be generalised, with some studies showing an increase in the rotors' performance [37, 53, 86, 89, 134] and others indicating a detrimental effect [6, 84, 100, 131, 156, 161].

Another unresolved issue concerns the influence of the Reynolds number on aerodynamic interactions in axial flow. Shukla and Komerath [131] showed experimentally that the close proximity of two rotors in hover causes a decrease in their efficiency at lower rotational speeds. The explanation for this was found in the stronger vortex-vortex interactions due to their lower circulation and slower downwash convection as shown in Fig. 2.13. Their subsequent study [130] showed the degradation in performance trends for overlapping bi-rotor configurations compared with the high Reynolds number data. On the other hand, Alvarez et al. showed an increase in detrimental effects at higher Reynolds numbers [6]. One possible reason for the discrepancy in the results is a difference in blade loading distribution between the experiments. In a study by Ramasamy [122], rotors with highly twisted blades, i.e. with lower tip loading showed mitigated detrimental interactions compared to cases where untwisted blades were used. However, a following investigation by Alvarez et al. [5] found no influence of the loading distribution on the interaction effects.

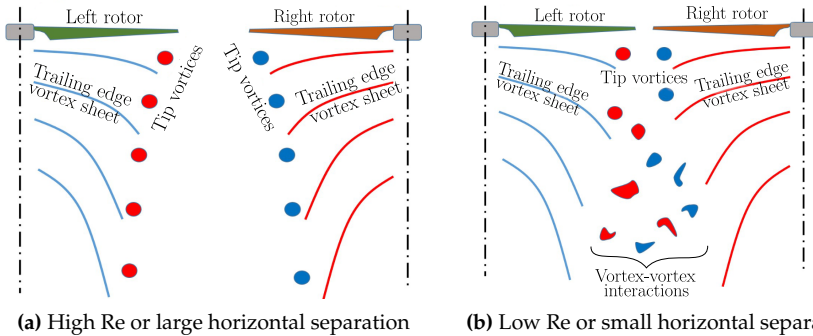


**Figure 2.13:** Interactions between rotors in hover depending Reynolds number by Shukla et al. [131]

Even in cases where negligible changes in averaged performance were observed due to interactions, their impact on the produced noise levels and noise directivity can be significant. Zhou et al. [161] investigated twin-rotor hover cases where the proximity of the rotors resulted in small changes in the thrust coefficient (within 2%), however a considerable increase in the thrust fluctuations was observed with reduced hub spacing. This in turn, together with turbulent flow interactions, increased the aeroacoustic noise levels by up to 3 dB. De Vries et al. showed a change in sound pressure levels up to 10 dB for a system of three rotors in axial flight with an efficiency loss of barely 1.5% [34]. Studies by Lee and Lee [84] and Ko et al. [73] confirmed that increasing the spacing between the rotors reduces unsteady loading noise caused by interactions.

However, as demonstrated by Hwang et al. [64] in their numerical investigation of quadrotors, the effect of interactions on performance is limited in hover but becomes significant during the forward flight. A considerable drop in efficiency is observed for the rotors positioned downstream, i.e. in the wake of the front rotors. In a simpler case, the same applies to the back rotor in a two-rotor configuration known as a tandem. Early research into rotor-rotor interference showed that the back rotor operates in increased axial flow, which according to momentum theory, results in increased induced power [72]. Using a blade element theory, it can be stated that the downwash increases the inflow angle on the back rotor and thus reduces its angle of attack. The effect can also be seen in particle image velocimetry (PIV) studies by Atte et al. [8] and Stokkermans et al. [134], where the skew angle of the back rotor is steeper than that of the front rotor, even though it produces less thrust (Fig. 2.14). The greatest influence can be observed for cases where the wake of the upstream rotor(s)

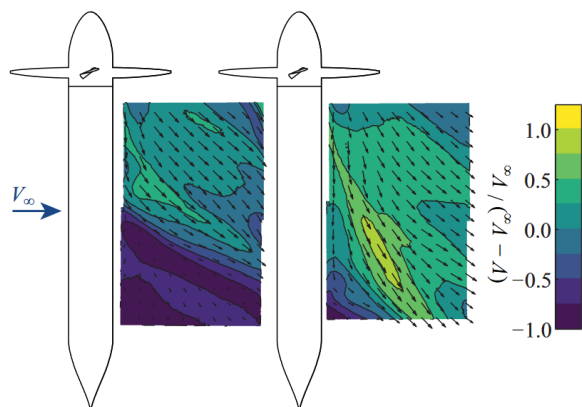


**Figure 2.14:** Time-averaged PIV flowfield of a tandem configuration at  $\mu = 0.69$  by Stokkermans et al. [134]

passes close to the rotor plane, which is the case for the higher positive tilt angles [12]. Healy et al. [59] in a numerical study of a tandem configuration, showed how the disc loading and advance ratio affect the wake skew angle of the front rotor, resulting in higher efficiency losses for the downwash rotor at higher flight speeds and lower disc loadings. Changes in the multirotor wake propagation depending on the advance ratio were also demonstrated experimentally using particle image velocimetry (PIV) by Throneberry et al. [139].

Another important factor affecting the inter-rotor interactions is the wake geometry. For a fixed-pitch rotor in forward flight the advancing side tip vortex is stronger but propagates downward more quickly, while the weaker tip vortex on the retreating side remains closer to the rotor plane. The asymmetry of the wake leads to asymmetric interactions, which are particularly evident in the diamond (plus) configuration. In this case the side rotors are affected differently by the wake of the leading rotor, which cannot be reproduced with a uniform inflow assumption [93]. Misiorowski et al. [102] in the numerical study of a diamond quadrotor, showed that rolled-up tip vortices of the front rotor have an asymmetric, beneficial effect on the performance of the side rotors. As a result, the diamond alignment shows an improved efficiency compared to a square (cross) configuration. This conclusion was demonstrated in CFD simulations by Hwang et al. [64], also using a potential method in the study of Barcelos et al. [12]. However, the plus configuration requires larger control inputs to compensate for the additional moments and indicates a 30% lower control authority as estimated by Niemiec and Gandhi [106].



(a) Volocopter VoloCity [146]



(b) EHang EH216 [42]

**Figure 2.15:** Urban air mobility designs

A negative impact of the downwash on the back rotors in the square configuration can be reduced by increasing the horizontal rotor spacing, as shown in the wind tunnel measurements and flight tests of Atte et al. [8]. However, for the tandem configuration, Healy et al. [59] demonstrated that increasing the vertical offset was a more effective solution. The study by Lee et al. proved that increasing the horizontal spacing has a negligible effect compared to introducing vertical separation, especially at higher advance ratios [85]. The numerical study of the SUI Endurance quadcopter by Diaz and Yoon [144] showed a 63% thrust increase achieved by undermounting the front rotors. An alternative approach was suggested in the following investigation by Healy et al. [58], which shows that outward longitudinal canting of the rotors can reduce the lift deficit on the back rotor together with the pitching moment. However, changing the rotor canting has an effect on the noise directivity which must be taken into account [160].

The introduction of the vertical offset allows the design of overlapping rotors and thus more compact configurations, which in turn increases the aerodynamic interactions. A few studies have been conducted for such cases, mostly focusing on hover [86, 130] or axial flight performance [113]. Nevertheless, overlapping rotors are also applicable in edgewise flow conditions, as in the case of the novel overlapped quadrotor design tested by Chen et al. [29].

Research on multirotor interactions is not limited to small UAVs. Configurations with a larger number of rotors have attracted much interest due to urban air mobility (UAM) concepts, such as the EHang EH216 with 8 pairs of co-axial rotors or the Volocopter VoloCity with 18 rotors (Fig.2.15). It has been shown that the use of a larger number of slower rotating rotors has an aeroacoustic advantage over a traditional helicopter configuration [66, 67]. For the same reason, the influence of the number of rotors on the system performance and aeroacoustics is also a topic

of investigation for UAVs. A decrease in first harmonics noise levels for a larger number of rotors was observed by Tinney and Sirohi [140] due to lower rotor RPM and thus reduced loading and thickness noise. Similar results were obtained for larger diameter rotors. However, in a study by Intaratep et al. [65] the hover efficiency of a multirotor decreased with the number of rotors, while the overall sound pressure level (OASPL) remained almost identical, with only an increase in the broadband noise component.

Noise control for multirotor configurations can be achieved by phase synchronisation [125, 132, 160], shown to be an effective method of tonal noise reduction with negligible impact on the rotor performance. The concept seems unrealistic for fixed-pitch rotors, controlled by differential RPM, yet it can be applied to vehicles with a larger number of rotors by synchronising rotor pairs or for variable-pitch rotors.

Although the complexity of the multirotor flow can be captured by CFD codes [155], the consideration of interaction effects in the initial steps of the aircraft design process is only possible by using lower-fidelity tools. Pinti et al. [114] proposed a solution to analyse the influence of different longitudinal and vertical spacings in the tandem configuration, where the low-fidelity tool was used for identifying the key parameters to perform more accurate high-fidelity calculations in the next step. Conley and Shirazi [31] validated the multirotor performance results from two mid-fidelity tools with experimental data. As shown, such methods can offer a compromise between computational cost and accuracy. Nevertheless, the reliability and possible error margins of lower cost simulations need to be investigated for the wide range of design parameters.



## 3 Tools and methods<sup>1</sup>

### 3.1 Blade geometry and model preparation

A 2-bladed, fixed-pitch KDE-CF125-TP 12.5"×4.3 rotor with a diameter of 0.318 m and solidity of 0.075 was used. The KDE-CF series includes carbon-fibre rotors, popular in UAVs and among researchers [23, 61, 124]. Computational models were prepared based on a 3D-scanned blade, divided into a series of spanwise cuts (Fig. 3.1). Figure 3.2 shows the obtained twist and chord distributions. Due to the inaccuracies of a scanned surface, the measured blade cuts were approximated with hydraulically smooth airfoil shapes. For this purpose, the cross-sections were imported as points into the dedicated Python code which identifies the airfoil thickness, maximum camber and maximum camber position. Based on the parameters obtained, the sections were replaced with arbitrary 4-digit NACA profiles [2]. An additional advantage of this approach was an easy implementation of the defined NACA profiles into the XFOIL code calculating the airfoil aerodynamic characteristics [39]. The accuracy of the approximation was the lowest for the last measured cut, which did not resemble the aerodynamic profile as a result of the blade manufacturing process. Nevertheless, its contribution to the generated loads is assumed to be negligible due to tip-losses. The cross-sections used as an input for the preparation of blade models are presented in Table 3.1.

The code allowed the definition of a trailing edge shape depending on the computational method, for which the blade model was used. To reproduce a blunt trailing edge shape for CFD (FLOWer) calculations each blade cross section was first approx-

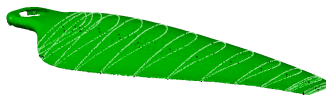


**Figure 3.1:** Scanned blade with cross-sections

---

<sup>1</sup>Parts of this chapter were published in [75–77].



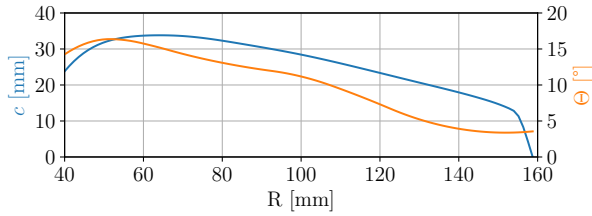


**Figure 3.2:** Twist and chord distributions

$y/R$	$c$ [mm]	$\Theta$ [°]	NACA	$x_{LE}$ [mm]	$z_{LE}$ [mm]
0.256	23.8	14.25	3621	9.5	-1.59
0.314	31.4	16.27	4415	10.73	-2.05
0.352	33.2	16.25	3516	11.22	-2.05
0.404	33.8	15.35	4414	11.75	-1.76
0.448	33.6	14.32	4414	11.93	-1.5
0.544	31.4	12.58	4513	11.84	-0.75
0.641	28.4	11.18	5512	11.18	0.18
0.737	24.7	8.41	4511	10.07	1.18
0.833	20.6	5.22	3411	8.41	2.4
0.93	16.4	3.56	3410	5.76	3.32
0.981	13.3	3.68	2609	3.26	3.79
0.993	11.4	3.95	1609	1.49	3.78
1	9	5.48	2811	-0.52	3.88



**Table 3.1:** Input table for blade model

imated by a NACA profile with a longer chord, which was then shortened to the length of a scanned profile or to the defined trailing edge thickness (Fig. 3.3).

An original blade adapter from the manufacturer allowed blade folding and was designed to be mounted directly onto a motor (Fig. 3.4a). The adapter was redesigned for the experiment to lock the blade in position and was not included in the simulations. The blade models were prepared with a  $0.3R$  root cut-out, except for a CFD model with a simplified blade connection (Fig. 3.4b). Stiff blades with no lead-lag freedom were assumed in the calculations.

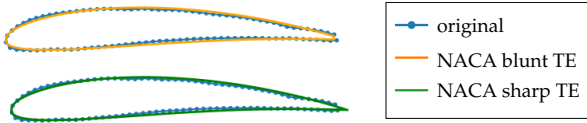
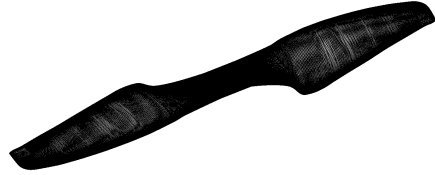


**Figure 3.3:** Example - trailing edge shapes of recreated profiles



**(a)** Original rotor mounting [70]



**(b)** Blades connection in the CFD model

**Figure 3.4:** Blades connection in the KDE rotor

## 3.2 Computational tools

The experimental results from the isolated rotor test campaign (1r) and multirotor experiment with bi-rotor (2r) and quadrotor configurations (4r) were validated using several computational tools described in the following sections. For clarity, a summary of the main computational settings is presented in Table 3.2.

### 3.2.1 BET and FW-H code

A blade element theory (BET) code was the most simplified and the least computationally expensive of the methods applied. In BET, steady lift and drag values are calculated for spanwise blade sections at different azimuthal positions and then integrated for the whole blade and one full rotation as described in Section 2.2.1. An inflow angle and a corresponding angle of attack can be determined iteratively from a loop with an inflow model. A dedicated Python code used in this study included a linear inflow model developed by Pitt and Peters [30, 115]. According to the applied method the induced velocity distribution can be described by mean and cyclic components:

$$v_i = v_0 + \frac{r}{R}(v_c \cos\psi + v_s \sin\psi), \quad (3.1)$$

	Configurations	Blade model	Wake model	Flow assumptions	Time step	Aeroacoustic tool
<b>BET</b>	1r	15 elements airfoil characteristics	-	viscous, compressible	1°	APSIM
<b>UPM</b>	1r, 2r, 4r, 4r <sub>z</sub>	15x98 elements thick blade	free wake, vortex lattice, hybrid <sub>1r</sub>	potential	2°	APSIM (1r,4r)
<b>RAMSYS</b>	1r, 4r, 4r <sub>z</sub>	15x50 elements thick blade	free wake, vortex lattice	potential	2°	ACO (1r)
<b>PUMA</b>	1r, 4r, 4r <sub>z</sub>	45 elements lifting line	free wake, vortex lattice	potential, airfoil polars: viscous and compressible	5°	KIM (1r)
<b>CORAL</b>	4r	15x20 elements lifting surface	free wake, hybrid	potential	4°	-
<b>FLOWer</b>	1r, 2r, 4r	2.4 million elements thick blade	URANS	viscous, compressible, rotational	1° (1r,2r,4r) 0.5° (4r)	ACCO (1r,4r)

Table 3.2: Summary of main computational settings

where  $v_0$  stands for a uniform induced velocity, while  $v_c$  and  $v_s$  represent fore-to-aft and side-to-side inflow variations. For the steady state cases considered, the inflow depends on the aerodynamic coefficients of thrust, pitching and rolling moment ( $C_T, C_{M_R}, C_{M_P}$ ) in a linear fashion presented below:

$$\begin{Bmatrix} v_0 \\ v_s \\ v_c \end{Bmatrix} = [L] \begin{Bmatrix} C_T \\ C_{M_R} \\ C_{M_P} \end{Bmatrix}. \quad (3.2)$$

Using the unsteady actuator disc theory, Pitt and Peters proposed the following form of the gain matrix  $L$ :

$$L = \begin{bmatrix} \frac{1}{2v_T} & 0 & \frac{15\pi \tan \frac{\chi}{2}}{64v_m} \\ 0 & -\frac{4}{v_m(1+\cos\chi)} & 0 \\ \frac{15\pi \tan \frac{\chi}{2}}{64v_T} & 0 & \frac{4\cos\chi}{v_m(1+\cos\chi)} \end{bmatrix}, \quad (3.3)$$

with the mass flow parameter  $v_m$  described as:

$$v_m = \frac{\mu^2 + \lambda(\lambda + v_0)}{v_T} \quad (3.4)$$

and

$$v_T = \sqrt{\mu^2 + \lambda^2}. \quad (3.5)$$

The wake skew angle  $\chi$  was estimated depending on the advance ratio  $\mu$  and inflow ratio  $\lambda$  as described in Section 2.1.

For the application of low speed forward flight of the helicopter rotor Chen proposed to limit the inflow estimation to the thrust effect [30]. This approach, called PP1 within this work, results in a lateral variation of the induced velocity as presented in Fig. 3.5a. In contrast, the full coupling, including in addition the influence of pitching and rolling moments (PP2), captures both lateral and longitudinal components of the inflow distribution (Fig. 3.5b). The presented mean aerodynamic loads were obtained using the PP2 model, while a comparison and evaluation of the two approaches for a UAV rotor application was included based on the transient loading result.

Viscous aerodynamic characteristics for the identified NACA profiles were generated using XFOIL, including variation of Mach number ( $M$ ) between 0.05 and 0.4. Corresponding Reynolds numbers at each cross-section were applied to an automated script for XFOIL input generating profile performance data for angles of attack between  $-10^\circ$  and  $15^\circ$  with  $0.1^\circ$  increments. A separate code was used in the next step to

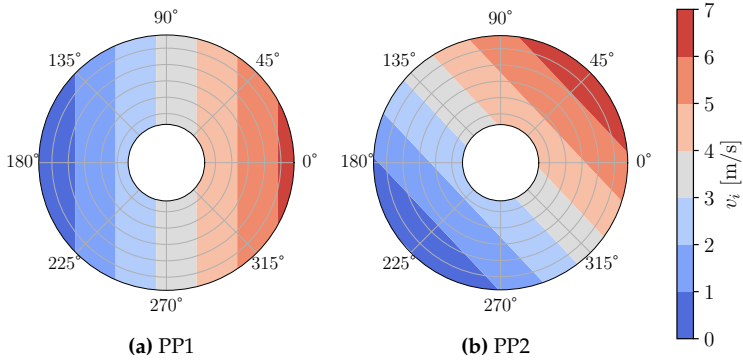


**Figure 3.5:** Induced velocity distribution with Pitt and Peters model for 5400 RPM, 12.9 m/s, tilt  $-10^\circ$

identify the linear region and extrapolate the obtained lift and drag coefficients for higher angles of attack with the Viterna post-stall model [96] (Fig. 3.6). The BET code did not include a wake model. Calculations were performed for 15 spanwise and 360 azimuthal elements.

Two methods of including tip-loss effects were investigated, either by adding Prandtl's function to the solution or by estimating a tip-loss factor  $B$  as a constant value (as described in [88] typically between 0.95 and 0.98). Prandtl's method led to an underestimation of the thrust values for a rotor operating in a strong upwash (at positive tilt angles), therefore in the presented results a factor  $B$  was simply approximated as 0.97 and the mean thrust values were reduced by a factor  $B^3$  for forward flight cases [68].

As the final step, the resulting sectional load distribution was used as an input to a coupled aeroacoustic prediction code based on the Ffowcs Williams-Hawkings (FW-H) equation with the formulation described in [55]. The acoustic pressure at the observer positions was calculated as the sum of the sectional load contributions from each spanwise blade element for a selected azimuthal resolution. The frequency spectrum was calculated using the Welch algorithm. Only the loading noise was considered in the acoustic calculation as the analysed observer positions were below the rotor plane where no significant thickness noise contribution is expected. The near-field loading noise component was negligible in the results.

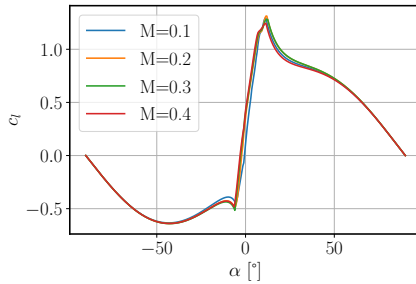


**Figure 3.6:** Viterna extrapolation of lift coefficient for higher angles of attack used in the BET code

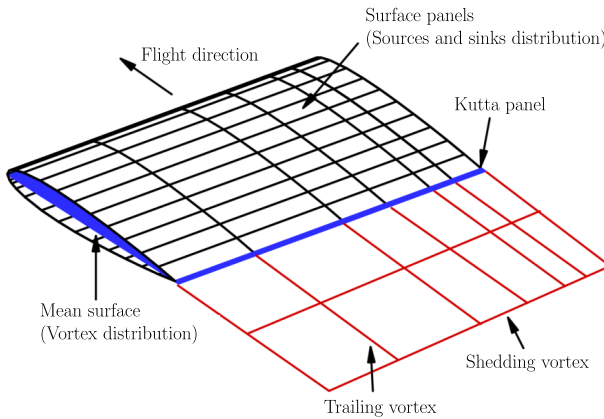


**Figure 3.7:** Numerical model used in UPM

### 3.2.2 UPM and APSIM

UPM is an unsteady free wake panel method developed at DLR allowing the simulation of flows with arbitrary body shape and motion [4, 153]. Lifting bodies in UPM are modelled as a distribution of sources and sinks ( $\sigma$ ) on the blade surface, taking into account the displacement effect and the vortex distribution  $\Gamma$  (equivalent to doublets) along the mean surface simulating the lift (Fig. 3.7). The weighting function of the doublet strength is prescribed over the blade chord and is proportional to the local profile thickness. In UPM, the Kutta condition is ensured by a Kutta panel, represented as a zero-thickness elongation of the trailing edge along its bisector. An iterative scheme to ensure pressure equality at the Kutta panel was used in the calculations, allowing unsteady pressure terms to be considered. In UPM an impermeable

boundary condition is defined using the Neumann formulation. As a result, a system of algebraic equations is formulated to find unknown singularities' strengths:

$$\sum_{j=1}^{n_{\text{surf}}} A_{ij} \sigma_j + \sum_{j=1}^{n_{\text{chord}} + n_k} B_{ij} \Gamma_j = RHS - \sum_{j=1}^{n_{\text{wake}}} C_{ij} Z_j, \quad (3.6)$$

$$i = 1, 2, 3, \dots, n_{\text{surf}} + n_k,$$

where  $A_{ij}$ ,  $B_{ij}$ ,  $C_{ij}$  are influence coefficients and  $n_{\text{surf}}$ ,  $n_{\text{chord}}$ ,  $n_k$  stand for the number of panels on the blade surface, mean surface and Kutta panel respectively. Based on the obtained strengths and corresponding velocities, the loads on the blades can be estimated using the unsteady Bernoulli equation. The effects of aerodynamic interactions between the rotors are represented while defining an impermeable surface and tangential flow conditions for each rotor and while computing induced velocities at wake corner points, including the strengths from the other bodies and wakes at each time step.

The circulation of the trailed wake panels  $Z$  is determined by the Kutta panel for each azimuthal increment and remains constant for the shed row to satisfy the condition of no pressure gradient (no lift) in the wake. Even though the number of unknowns remains the same throughout the simulation, the influence coefficients must be recalculated and an increasing number of wake panels  $n_{\text{wake}}$  at each time step means an increasing number of Biot-Savart computations. As a result, the wake evolution is the most computationally expensive part and the simulation time grows quadratically with the azimuthal and spanwise resolution of the panels. The computation time in UPM is reduced by parallel execution via OpenMP on multiple cores. In addition, a fixed number of wake filaments can be set to accelerate computations in cases where older vortices have a negligible influence on the results. While for the isolated rotor the wake could be limited to three revolutions, multirotor cases required longer wakes to capture rotor-rotor interactions. For this reason, the spanwise panel resolution, determining number of wake panels shed at each step, was crucial to control the computational benefit of the potential method. In the present study, the blade was modelled with 15 spanwise panels as a finer resolution would result in a computation time increase by a factor of 5 with only a 2% decrease in the estimated thrust coefficient (Fig. 3.8).

The final blade model consisted of 1425 panels with 95 chordwise elements. A cosine distribution was applied to the chordwise panels to refine the mesh towards the leading and the trailing edge. To satisfy the Kutta condition, real blade sections were replaced by NACA profiles with a sharp trailing edge, resulting in an inaccurate

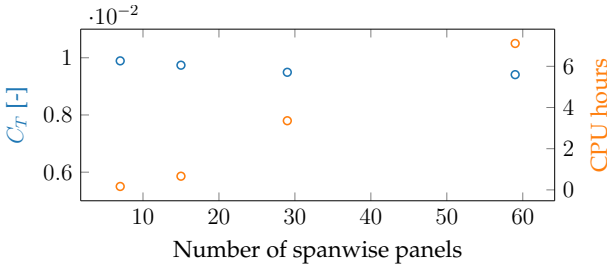


**Figure 3.8:** Influence of the number of spanwise panels on the results of an isolated rotor

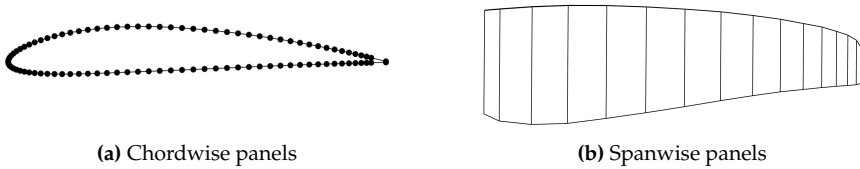


**Figure 3.9:** Panel distribution in UPM

representations of the blade thickness for approximately the last 4% of the blade chord. For this reason, the panel resolution was refined up to  $0.96c$ , followed by a single TE panel (Fig. 3.9a). In the radial direction the panels were clustered towards the blade root and tip according to the expected spanwise circulation gradients. Due to the low rotational velocities at the blade root wake panels are likely to accumulate and cause numerical issues if the blade panel distribution is too dense in this region. To overcome this problem an asymmetric clustering factor (CF) was applied based on [7]:

$$CF = \frac{(Y + 2X) \frac{Y+1}{Y-1} \left(\frac{n_i}{N} - X\right) \frac{1}{1-X} - Y + 2X}{(2X + 1) \left(1 + \frac{Y+1}{Y-1} \frac{n}{N} - X \frac{1}{1-X}\right)}, \quad (3.7)$$

where  $n_i$  stands for the section number and  $N$  for the total number of sections.  $X$  and  $Y$  are parameters controlling panel distribution asymmetry and refinement toward the ends, respectively. The values of  $X = 0.3$  and  $Y = 1.08$  were selected, resulting in the distribution shown in Figure 3.9b. The presented blade model was produced using a panel generation code PANGEN. The geometry input was prepared by interpolation between defined cross section parameters for an arbitrary panel distribution.

Another crucial decision for the selected blade model was the choice of the step size and number of revolutions which ensured capturing the aerodynamic effects.



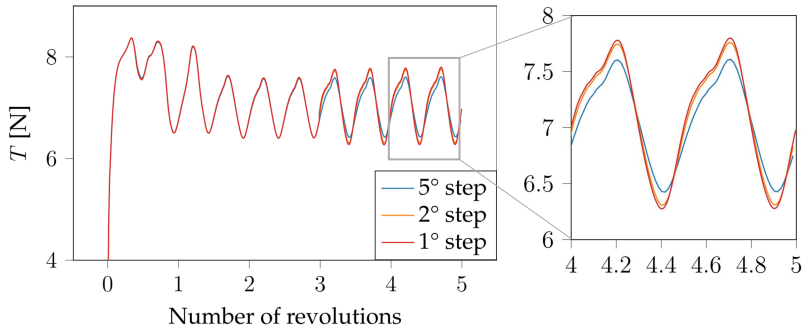


**Figure 3.10:** Thrust convergence study depending on the time step size (tilt  $-10^\circ$ , 5400 RPM and flight velocity 12.9 m/s)

UPM settings allow the decrease of the time step size during the simulation in order to reduce CPU time while resolving sufficiently long wakes. Figure 3.10 shows changes in the calculated thrust for the initial step size of  $5^\circ$ , reduced after 3 revolutions. The applied grid delivered a convergent result with thrust fluctuations reaching periodicity already after 4 rotations for all step sizes considered. Reducing the step size below  $2^\circ$  did not result in a significant change in the signal magnitude or shape. This observation was also true for multirotor simulations with high interactions, however, for these cases up to 12 rotor revolutions were required to reach a convergent solution.

The full span wake was modelled with a vortex lattice, yet additional calculations were performed using a particle wake method, where the vortex filaments are replaced by point vortices after a defined number of time steps (Fig. 3.11) [142]. The particle model solves the vorticity transport equation derived from the incompressible Navier-Stokes equations [151] as described in Section 2.2.2. As there are no links between neighbouring particles, this approach provides an improved solution for cases where the wake interferes with solid bodies.

Optionally a roll-up model based on [19, 120] can be used in UPM for a more accurate representation of concentrated tip vortices. Vortex roll-up is particularly important for aeroacoustic computations to capture strong BVI interactions as a result of the blade passing through a single vortex rather than a full wake sheet. The model is implemented as a post-processing step to the free wake computation and by default it does not modify the full wake trajectory. For this reason, in the results presented, the roll-up model was only used for cases that served as input for aeroacoustic

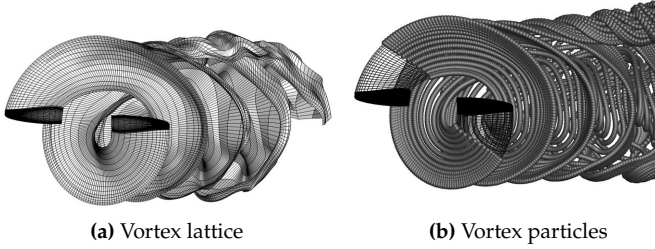


**Figure 3.11:** Wake representations in UPM

simulations. The vortex core size of the inner wake was defined as  $0.8\bar{c}$  and that of the tip vortex as  $0.3\bar{c}$ , where  $\bar{c}$  is the reference length defined as the mean aerodynamic chord. The radii sizes were chosen based on the selected spanwise panel distribution, the applied vortex model and the stability requirements. Relatively high values were dictated by the Rankine vortex core model, which estimates higher velocity peak than other models for a given core radius as shown in Fig. 2.8. In addition, the given values ensured a stable solution even for multirotor cases with intense interactions. The Squire vortex growth model was applied to the tip vortices [14], while the velocities induced by the inner vortices were calculated using the linear growth model described as:

$$r_c = r_{c0}(1 + \psi/360), \quad (3.8)$$

where  $r_{c0}$  stands for the initial core size. It should be noted that the applied settings of the vortex core model and vortex growth were optimal or the only options in the UPM version (283) available at the start of the presented work. In order to maintain consistency, the applied settings remained unchanged, although additional options have been implemented in newer UPM versions.

Viscosity and compressibility effects can be included in the post-processing. In the presented results, a simple viscosity correction was applied to improve the prediction of torque values. The contribution of the profile torque  $C_{Q_0}$  was estimated using the following equation [68]:

$$C_{Q_0} = \frac{\sigma C_{d_0}}{8} (1 + 1.5\mu^2 - 0.37\mu^{3.7}), \quad (3.9)$$

where the zero-lift section drag coefficient  $C_{d_0}$  had a value of 0.0075.  $\sigma$  and  $\mu$  stand for the rotor solidity and the advance ratio, respectively.

UPM generates output files dedicated for a coupled aeroacoustic code APSIM

(Aeroacoustic Prediction System based on Integral Methods) [153, 154]. APSIM considers linear sound propagation in the free far-field and includes two integral formulations of the FW-H equation for a permeable and an impermeable surface. The latter approach, based on the Farassat 1&1A formulation [43], was used in this study. Quadrupole noise is neglected with the assumption of shock-free flow. The input included the pressure distribution together with the blade surface coordinates from the last rotation calculated in UPM. Due to a constant phasing between the rotors, the input from one rotation was sufficient to capture the interactions for multirotor cases. The aeroacoustic computation in APSIM is performed in the time domain at given observer locations and the pressure time signals are then Fourier-analysed to obtain the frequency spectrum.

### 3.2.3 PUMA and KIM

PUMA (potential unsteady methods for aerodynamics) is an unsteady lifting line / free wake solver developed at ONERA since 2013. It includes a coupling between an aerodynamic module and a kinematic module. The aerodynamic module uses the lifting line method with a free wake model based on Mudry theory [104], which describes the unsteady evolution of a wake modelled by a potential discontinuity surface. It can handle some 3D corrections for blade sweep through local Mach number and angle of attack corrections, and 2D unsteady nonlinear aerodynamics effects through dynamic stall models [87, 141]. Moreover, different time discretizations are available in order to balance between accuracy, numerical stability and computational time. The kinematic module employs a rigid multi-body system approach using a tree-like structure with links and articulations. It enables any arbitrary motion between the different elements. PUMA is usually used for any aerodynamic study of fixed wings and rotating wings configurations which require low computational cost or a large amount of parametric investigations like pre-design studies. It has also been successfully applied for helicopter rotors wake in interactions with obstacles [15, 48] and for rotor / rotor interactions [16].

In this study, the 2D airfoil characteristics, the same as the ones used in the BET method, were included to account for viscosity and compressibility effects. The lifting line was divided into 45 radial stations for wake emission using a square root distribution. A time step of  $5^\circ$  was used for the unsteady computation over 8 rotor revolutions.

The KIM code [116, 121] is used to determine the noise emission by solving the Ffowcs-Williams and Hawkings integral with an advanced time formulation. The

noise source considered is the surface pressures on the blades but since the PUMA code only provides the spanwise distribution of loads, those quantities need to be reconstructed. An empirical pressure distribution, typical for a rotor blade section, is set on the suction side. The pressure level is then set so that once integrated the loading in terms of local thrust and torque prescribed by the PUMA code is recovered.

### 3.2.4 CORAL

CORAL is a joint effort of Roma Tre (RM3) University, National Technical University of Athens (NTUA) and Carleton University's Rotorcraft Research Group (CU) under the coordination of Kopter Germany, a member of Leonardo group. It includes tools for the combined aeroelastic and aeroacoustic analyses of helicopter configurations [109]. The aerodynamic part of the code consists of models of varying fidelity including free wake vortex particle modules and an URANS hybrid CFD module. Application of each of the modules depends on the scope of the analyses, in terms of time efficiency and/or accuracy. The free vortex wake models solve the inviscid-incompressible-unsteady flow equations around lifting/or non-lifting bodies which can be treated either as lifting lines, lifting surfaces or thick panel bodies (lifting and non-lifting). The CFD module is a hybrid one based on the strong coupling of an Eulerian and a Lagrangian [110] model. The Eulerian part solves the compressible flow equations on meshes (structured and/or unstructured) confined in a limited space around the solid bodies. Both fully resolved and actuator line representations [133] of lifting bodies can be considered in the analyses. The Lagrangian part is based on particle representations (particles carrying mass, vorticity, dilatation etc.) and solves the flow equations in material formulation in the far field.

The presented results were prepared with the lifting surface modelling option with no correction from airfoil polars and a step size of  $4^\circ$ . The hybrid wake consisted of a vortex lattice for the first  $1/6$  of the revolution and was then converted into vortex particles. The blade model consisted of 20 spanwise and 15 chordwise elements. A comparison between the lifting surface model from CORAL and thick blade model used in UPM is presented in Fig. 3.12.

### 3.2.5 RAMSYS and ACO suite

The CIRA aerodynamic simulations were carried out by using the medium-fidelity code RAMSYS [145], which is an unsteady, inviscid and incompressible free wake vortex lattice boundary element methodology (BEM) solver for multi-rotor, multi-body configurations developed at CIRA. It is based on Morino's boundary integral formu-

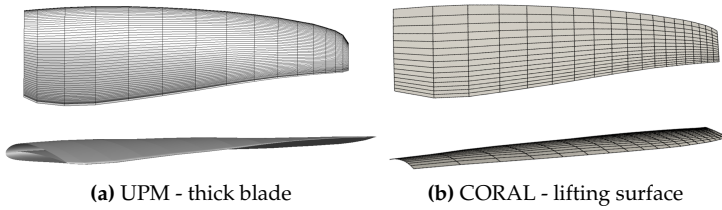


**Figure 3.12:** Applied blade models

lation [103] for the solution of Laplace’s equation for the velocity potential, while the wake is modelled according to the novel formulation proposed by Gennaretti and Bernardini [50]. The surface pressure distributions are evaluated by applying the unsteady version of Bernoulli equation, which is then integrated to provide the forces and moments on the configuration and the surrounding obstacles. A computational acceleration is obtained by applying the module for symmetrical flows and geometries implemented in the solver and the parallel execution via the OpenMP API. The applied blade model consisted of 15 spanwise and 50 chordwise elements. The simulations were performed for 6 rotor revolutions with time step of  $2^\circ$ .

The aeroacoustic simulations were carried out by using the ACOustic suite developed at CIRA and consisting of several tools for the evaluation of noise generation and propagation. The ACO-FWH solver was used for computing the acoustic free-field generated by the rotor blades. It is based on the FW-H formulation [47] described in [25, 26]. The advanced-time formulation of Farassat 1A is employed, and the linear terms (the thickness and loading noise contributions) are computed through integrals on the surrounding surface or moving blades (impermeable/rigid surface formulation). Moreover, the space derivatives of the linear terms are also evaluated through a numerical differentiation for coupling the free-field solution computed with FW-H with scattering solvers [10]. In particular, the coupling of the FW-H code with the Boundary Element Method is enabled through a boundary surface defined in terms of pressure and normal derivative of the pressure. The FW-H code automatically extrapolates a secondary boundary surface along the normal direction to each panel of the primary boundary surface where the acoustic pressure is computed and the corresponding derivative is evaluated through finite difference techniques among the two surfaces. The quadrupole contribution due to the nonlinear terms distributed in the perturbed field around the blade is neglected. The computational acceleration is obtained by a parallel execution via the MPI API. The simulation of the aeroacoustic free field was carried out by using the aerodynamic database evaluated by RAMSYS,

and consisting of the rotor blade pressure distributions.

The ACO-FAM solver was used for the simulation of the acoustic scattering field. It is based on the numerical solution of the convected Helmholtz equation which can be handled with an integral boundary element method [11]. In particular, ACO-FAM implements a combined Helmholtz integral equation formulation (CHIEF) which is solved with a collocation boundary element method. The ACO-ENV solver implements the acoustic propagation of a generic noise source through a ray approximation as described in [112]. This solver allows for the computation of several noise metrics starting from the definition of the flight trajectory and the noise source database encompassing the flight envelope. Moreover, it is able also to account for single reflections and attenuation by barriers or buildings. Single reflections are managed through an analytical mirroring of the source whereas the attenuation is managed through semi-analytical formulations [81, 95].

### 3.2.6 FLOWer and ACCO

For high fidelity simulation the numerical process chain used at the IAG was applied. CFD results were generated with the structured code FLOWer, originally developed by DLR [80] and further developed at the Institute of Aerodynamics and Gas Dynamics at the University of Stuttgart [78]. FLOWer solves three-dimensional, compressible Reynolds-averaged Navier-Stokes (RANS) equations, allowing transient flow solutions (URANS). Acoustic coupling was provided by IAG's FW-H solver ACCO [71] with usage of the data output of FLOWer.

A second order dual time stepping for temporal evolution was used with a time step of  $1^\circ$  to resolve the acoustic waves for isolated rotor study. For the aeroacoustic computations of 4r cases the step size was reduced to  $0.5^\circ$ . Furthermore, the Menter-SST (1r) and the Wilcox  $k-\omega$  [150] (2r,4r) turbulence models were applied to close the URANS equations. For spatial discretization the surface of the rotor was meshed with elements of 0.1% of the chord length in the streamwise direction. To recognize tip effects mesh refinement up to 1% of the radius in the spanwise direction was set. Using the Chimera technique a separate background mesh was created utilizing hanging grid nodes to reduce the numerical expense. Furthermore, in all background volume cells the WENO scheme of 6<sup>th</sup> order was carried out for numerical stability and reduced dissipation. In the surface region the dimensionless wall distance was kept low at  $y^+ < 1$ . The  $\lambda_2$ -criterion for vortex visualisation of an isolated rotor and applied numerical setup are shown in Figure 3.13 and 3.14, respectively. The setup for a quadrotor configuration consisted of of 32.4 million cells with 2.4 million in 8

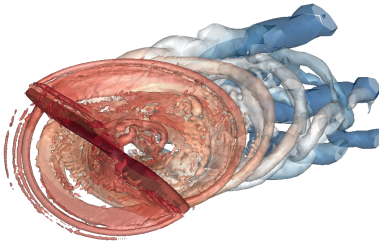


**Figure 3.13:** Wake of an isolated rotor visualised in FLOWer using  $\lambda_2$ -criterion

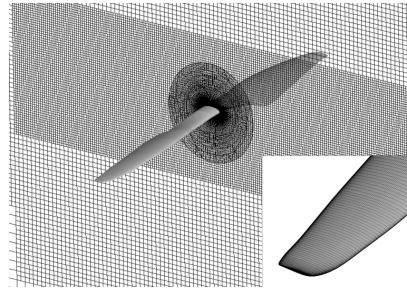
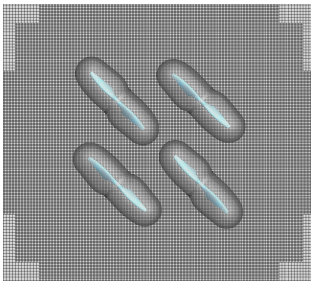
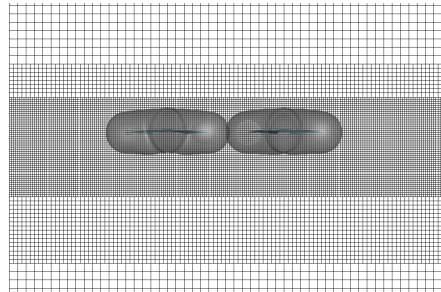


**Figure 3.14:** Numerical setup for 1r in FLOWer – background and rotor mesh with Chimera interpolation



(a) Top view



(b) Side view

**Figure 3.15:** Computational mesh for 4r in FLOWer

blade meshes and 8.7 million in the background. The Cartesian off-body (OB) mesh was refined downwash below the blades to capture the rotor wake (Fig. 3.15).

The acoustic computations of 1r were performed in ACCO using the cylindrical permeable integration surface (red in Fig. 3.16) to enclose all sound sources. The selection of the spatial discretization in the background mesh was based on the resolution of the first harmonic wave length, with 20 cells discretizing the wave length of the blade passing frequency (BPF). To avoid excessive dissipation the integration surface is placed in the finest grid area without cell size changes. The aeroacoustic calculations for 4r were based on pressure data on the physical blade surface from the last 2 rotations.

The scattering effects from the shielding element (Fig. 3.17) were computed using the Boundary Element Method (BEM) tool ScatMan [41] developed at the Institute of Aerodynamics and Gas Dynamics [40]. Within the ScatMan tool, the sound propa-

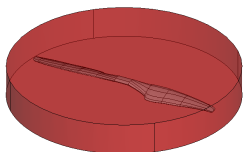


**Figure 3.16:** Integration surface for acoustic coupling as input for ACCO and physical surface of the rotor blade

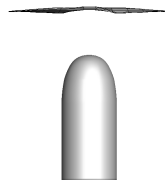


**Figure 3.17:** Rotor with a shielding element implemented in the Scatman tool

gation in the frequency domain is described by the Helmholtz equation, expanded with Green's second theorem resulting in the Helmholtz-Kirchoff equation [40]. To include ScatMan in the numeric tool chain consisting of FLOWer and ACCO, the shielding had to be discretized in triangle elements. ACCO in the first step calculates the incident sound pressure at the discrete points on the surface of the shielding as well as in a small distance above each surface point. Afterwards, the ambient conditions are added resulting in the complete solution consisting of an acoustic and scattering field.

### 3.3 Experimental setups

The experimental data was acquired during the isolated rotor (1r) and multirotor (2r, 4r) test campaigns described in the following sections.

#### 3.3.1 Isolated rotor test campaign<sup>2</sup>

The experiment included aerodynamic and aeroacoustic measurements and was conducted in the Rotor test facility Göttingen (RTG) of the German Aerospace Center (DLR). The RTG is an Eiffel-type wind tunnel with an open test section. The 1.6 m high and 0.8 m wide nozzle was used to achieve flow velocities of up to 24 m/s. The KDE 12.5x4.3" rotor with a horizontal axis was mounted on a rotatable base to allow variation of the rotor tilt angle, as shown in the sketch of the experimental setup in Figure 3.18. The aeroacoustic array consisted of 512 MEMS (micro-electrical-mechanical systems) microphones (Fig. 3.19) and was fixed positioned 1.35 m below the rotor and parallel to the rotor plane at 0° tilt angle.

The sensitivity of the applied microphones was estimated to be +/- 1 dB. Starting and stopping of the wind tunnel, rotor control, base rotation and aeroacoustic

<sup>2</sup>An extensive description of the 1r test campaign by F. Lößle can be found in [92] and [90].



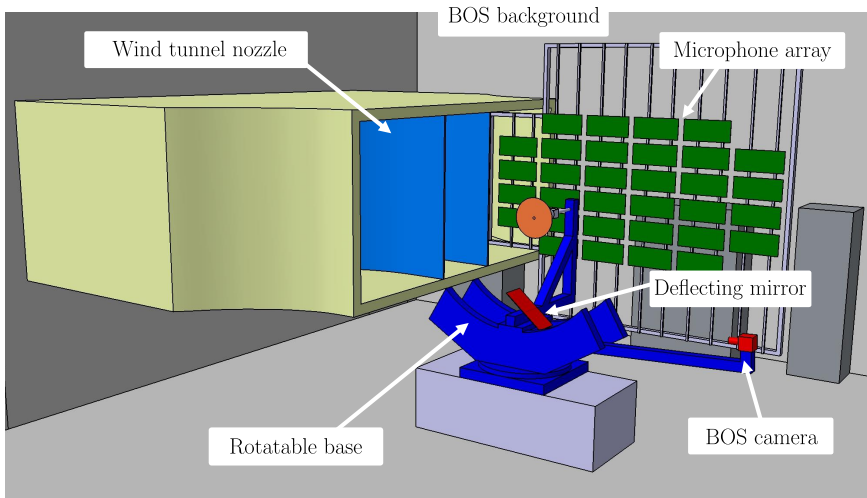


**Figure 3.18:** Experimental setup

measurements were performed using a dedicated LabView script. The presented noise levels were corrected based on the measurements with a loudspeaker emitting white noise to compensate for the effects connected with room acoustics. The analysis was focused on the tonal noise of the blade passing frequency as it was dominant in the measured spectra. Additionally, for most of the studied test cases the higher frequency components did not exceed the wind tunnel noise.

Thrust and torque were measured with a strain-gauge and piezoelectric balance, respectively. The drive unit assembly included axial ball bearings to avoid excessive side forces and moments acting on the strain-gauge sensor and was covered by a 3D-printed aerodynamic shielding. An impact of the mechanical friction in the bearings on the results was minimised by calibrating the balance prior to the measurements. The mounting of the rotor ensured free inflow with a slight blockage of the downwash. Nevertheless, the influence of the shielding on the rotor loads was found to be negligible in the initial UPM calculations. Zero measurements without a running rotor were taken before and after actual measurements to compensate for the sensor drift as well as the forces and moments generated on the shielding exposed to the flow. The velocity at the nozzle was measured with a Prandtl probe and the ambient conditions were monitored with pressure and temperature sensors.

A background oriented schlieren (BOS) setup was used to visualise tip vortices of rotors for selected cases. The BOS method uses the refraction of the light caused by the

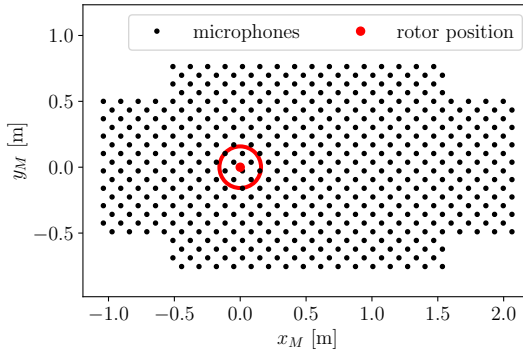


**Figure 3.19:** Microphone positions relative to the rotor plane

density gradient in the vortical flow. The refraction is registered on the background as a shift in the initial pattern, which can be then used for the vortex visualisation by cross-correlating the images. A detailed description of BOS techniques and applications was presented by Raffel [118]. Capturing of the small-scale rotor vortices required maximizing the sensitivity of the setup by setting large and equal distances between the rotor and the camera as well as between the rotor and the background [128]. For this reason the dotted background was attached to the ceiling, 2.9 m above the rotor, while the camera, mounted on the arm the rotor base, registered an image deflected by  $90^\circ$  through the mirror (Fig. 3.18). In order to reduce the image blur, the background was illuminated by four LED lights. DaVis software from LaVision was used for image processing.

### 3.3.2 Multirotor test campaign

The quadrotor experiment was conducted in the RTG wind tunnel with the setup developed from an isolated rotor campaign and presented in Fig. 3.20. The same fixed-pitch, two-bladed KDE 12.5x4.3" rotors were used, driven by 180 W Maxon EC-i 52 brushless motors with ENC 16 EASY encoders (Fig. 3.21). Custom blade adapters were used to facilitate the mounting of the rotors on the shafts and to eliminate lead-lag movement. The rotors were operated with a constant rotational speed of 5400 RPM, at a wind velocity of 12.9 m/s. In order to reduce the impact of the wind tunnel shear layer while maintaining the required flow velocity, the nozzle width was increased to 1.2 m. The rotors were mounted horizontally on a frame with threaded holes, which enabled the variation of the rotor spacing in 7 steps with the largest

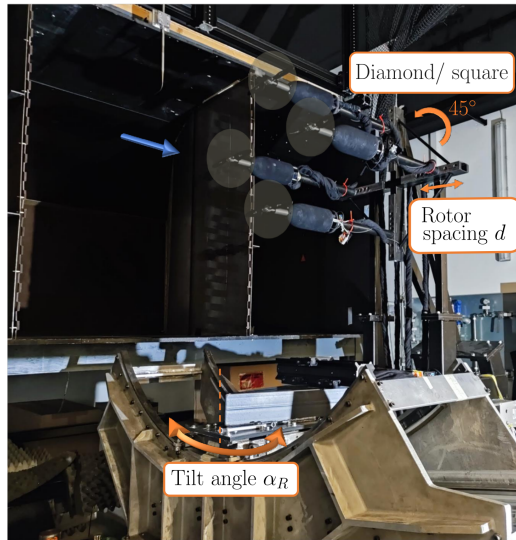


**Figure 3.20:** Experimental setup with investigated parameters

distance of  $1.68 D$  between the rotor hubs and the closest positioning with  $0.26 D$  rotor overlap. The mounting shafts ensured a distance of  $0.8 \text{ m}$  between the frame and the rotor plane, while the frame itself was designed to further minimise the downwash blockage. The frame support was prepared in two variants that changed the frame orientation relative to the flow by  $45^\circ$ , corresponding to alternating between square and diamond quadrotor configurations (Fig. 3.22).

The support structure was mounted on the rotatable platform. The rotor plane tilt angle was varied between  $-30^\circ$  and  $30^\circ$  with negative angles representing a nose-down (forward) tilt of the rotor plane and positive angles meaning a nose-up (backward) tilt. The rotation of the base and rotor control was achieved by a modified Labview script from the isolated rotor test campaign. Data was recorded at each test point for 10 seconds with a sampling rate of  $50 \text{ kHz}$ . Zero measurements without a rotating rotor were taken before and after the actual test cycles.

A relative phasing between the rotors, particularly important for overlapping hub spacings was adjusted by setting an initial position of each rotor as shown in Fig. 3.23. A simultaneous start of all rotors with the same acceleration was achieved using the EPOS270/10 controllers, with the motor encoders following an external ‘master’ trigger signal. Besides the quadrotor configurations, the measurements were performed for single rotors or two-rotor systems. Changes in the number of operating

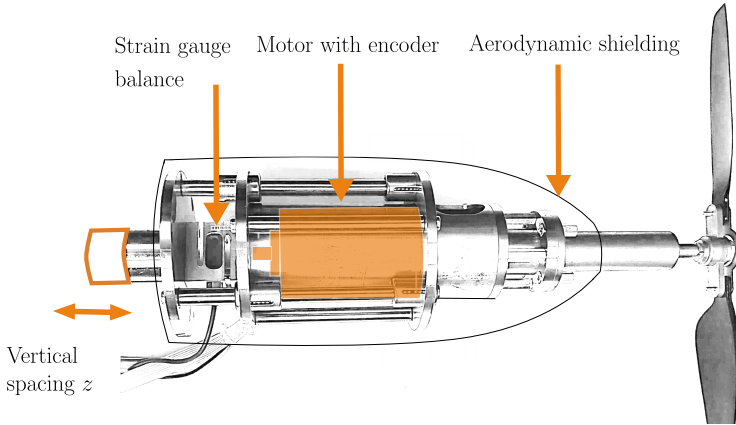


**Figure 3.21:** Setup of the drive unit

rotors were controlled in the LabView script.

The thrust of each rotor was measured using a one-axis strain gauge sensors KD40s from ME Messsysteme mounted as shown in Fig. 3.21. In order to improve the accuracy of the measurements, the balances were calibrated at the beginning of each test day. Calibration was performed with a slightly oversized nut mounted on the rotating motor shaft to simulate vibrations on the sensor comparable to those occurring with an operating rotor. In contrast to the isolated rotor experiment, no piezoelectric balances were used and torque values were derived from electrical power consumption measured for each rotor separately. Motor tests conducted by EBM-Papst showed that each motor used in the experiment had the same efficiency  $\eta$  as a function of the mechanical torque  $\bar{Q}$ , as shown in Fig. 3.24. Based on these results, the mechanical power  $P$  was calculated from the measured electrical power  $P_e$  through an iterative process (called here Method 1). In another approach (Method 2) suggested in [49] the mechanical power was derived from a dynamometer calibration assuming a constant rotor efficiency of 93% and additional losses on control electronics of 22.68 W:  $P = 0.93(P_e - 22.68)$ . As shown in Fig. 3.25, both results agreed within 1% accuracy and matched within the measurement error of 2.5% the torque values measured with a piezoelectric balance in the previous campaign.

The influence of varying the vertical distance between the rotors was investigated for the horizontal hub spacings  $d/D = 0.96$  and  $d/D = 1.2$ . Both the back rotors in the square bearhug configuration and the most aft rotor in the diamond configuration were raised above the front rotors' plane. For this purpose, a vertical offset  $z$  in

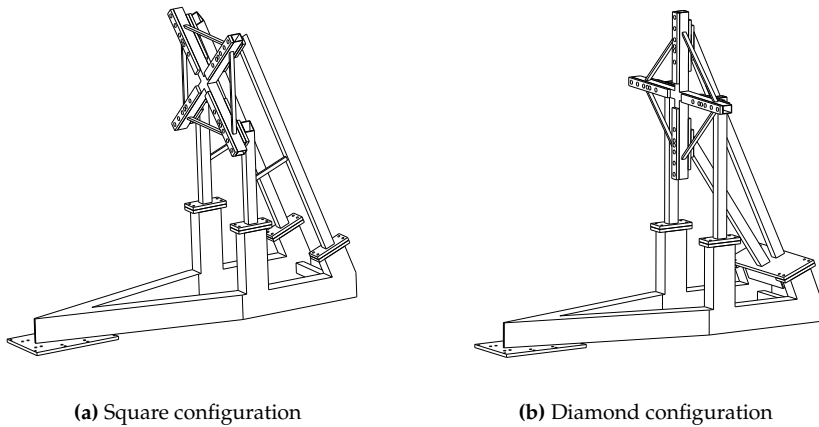


**Figure 3.22:** Frame support variants

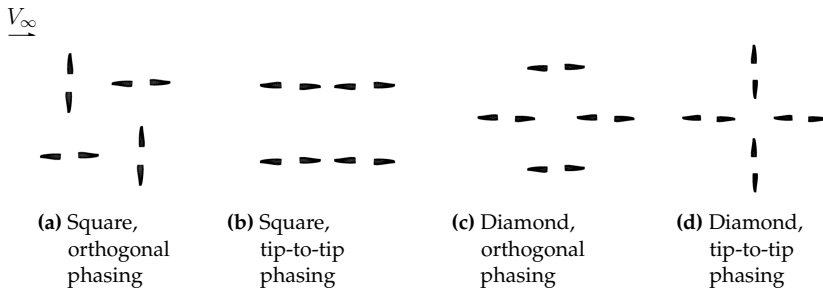


**Figure 3.23:** Initial blade positions depending on the rotor phasing

the steps of  $0.12 D$ ,  $0.26 D$ ,  $0.38 D$  was applied using metal distance rings of corresponding heights at the rotor mounting shown in Fig. 3.21. The maximum vertical offset of  $0.38 D$  at the horizontal spacing  $d/D = 1.2$  was not analysed for the square configuration due to interference between the raised aerodynamic shieldings and the front rotors' wakes.

Downwash velocities for a reduced set of test points were measured by means of particle image velocimetry (PIV). In the PIV method velocity in the flow is evaluated based on the displacement of seeding particles registered between images taken with the known time interval. Particles introduced into the flow are pulse illuminated with a light sheet generated by a laser and optics. Using a single camera for the particle image recording allows the evaluation of two velocity components in the illuminated plane, while all three components can be measured with a stereo-PIV setup including

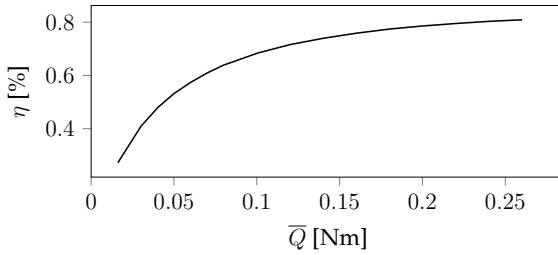


**Figure 3.24:** Motor efficiency as a function of torque at 5400 RPM

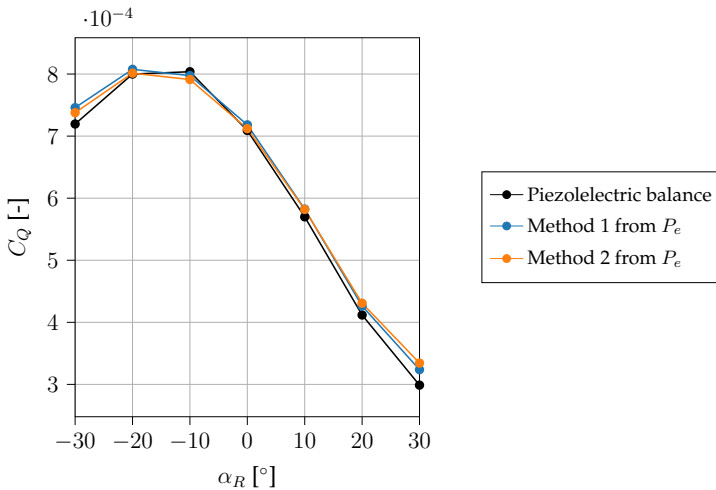


**Figure 3.25:** Torque coefficient measured and derived from electric power consumption

two cameras. The method was described in detail by Raffel et al. [119] and Adrian and Westerweel [3].

For the multirotor experiment, a stereo-PIV setup was used to evaluate the out-of-plane velocity component on a plane 75 mm below the quadrotor. For this purpose, a light sheet parallel to the rotor plane located at  $-10^\circ$  tilt angle was generated by two lasers with a wavelength of 532 nm and a combined pulse energy of 200 mJ. The downstream placement of the light sheet was selected to minimise the area of objects in the field of view, for which the velocity data could not be evaluated. Two types of seeding generators were placed next to the wind tunnel nozzle to ensure a homogenous distribution of the DEHS (Di-Ethyl-Hexyl-Sabacate) particles in the test

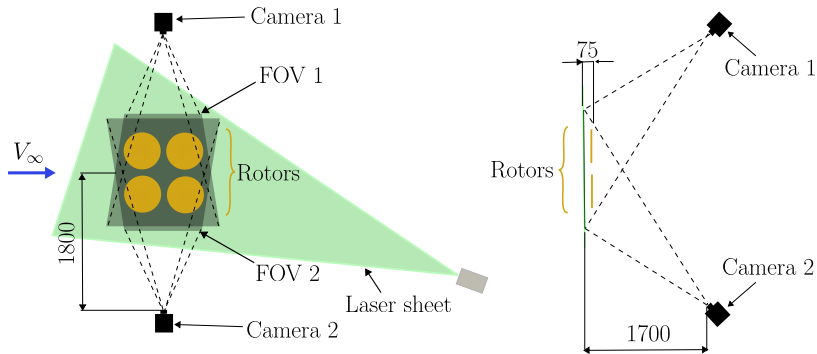


**Figure 3.26:** PIV setup presented for the square configuration with a top view (left) and side view (right) relative to the rotor plane

section. Two generators equipped with PIVcts1000 nozzles produced particles with an approximate diameter of  $2\mu\text{m}$ , while the other two delivered particles with a size of ca.  $0.9\mu\text{m}$  using Laskin-nozzles PIVpart45.

Two PCO.edge cameras with a resolution of  $2560 \times 2160$  pixels, equipped with lenses with a focal length of 35 mm were used for image recording (Fig. 3.26). The cameras were positioned at  $43^\circ$  angle to the plane and were stereo-calibrated prior to the measurements using a 3D calibration plate with defined mark spacing and plane separation. The analysed field of view of two cameras had approximate dimensions of  $750 \times 800$  mm, enough to capture the flow field under all four rotors in square and diamond configuration.

The cross-correlation of the images was performed in the DaVis software using an iterative approach, reducing the interrogation window size from  $48 \times 48$  pixels in the initial pass to  $16 \times 16$  pixels in the final pass. Given the applied window overlap of 75 %, this results in a spatial resolution of 3.35 vectors/mm in the vector fields. The images were acquired with a recording frequency slightly below 3.75 Hz, leading to a small phase offset of the rotor in each PIV image. The frequency offset was adjusted to result in approximately 1000 images evenly distributed over the rotor azimuth. Areas lacking illumination due to the shadows of the rotor axes and areas covered by the rotors were masked out before averaging the captured data for each test case and appear as white regions in the presented velocity maps. Masking was based on a cumulative criterion including stereo reconstruction errors, correlation values and expected velocity range.

## 4 Isolated rotor study<sup>3</sup>

The isolated rotor tests considered variations in flight velocity, rotor RPM and tilt angle. The aeroacoustic study was limited to cases presenting the effect of varying the rotor tilt between  $-30^\circ$  and  $30^\circ$  with a fixed flight velocity of 12.9 m/s and rotation speed of 5400 RPM, corresponding to the advance ratio of 0.146. Vortex trajectories were detected with the background oriented schlieren (BOS) method to improve understanding of the obtained trends and discrepancies in the results. Scattering effects from the shielding, rotor base and ground were simulated and compared with the experimental results for the blade passing frequency (BPF).

### 4.1 Aerodynamic loading prediction

Figures 4.1, 4.2, 4.3 present respectively the effect of change in the rotor RPM, flight velocity and tilt on the time-averaged thrust and torque.

The comparison indicates that general tendencies captured in the measurements were reproducible using all computational tools, yet some differences can be noticed in terms of the accuracy. It is worth mentioning that for moderate flight velocities the BET solution offered good loading estimation, even with simplified assumptions considering tip-loss factor. As the same 2D airfoil characteristics were used as an input for BET and PUMA, the loading calculated with these both methods is similar in Fig. 4.1-4.2 and for low tilt angles in Fig. 4.3. The accuracy of these solvers became worse for low advance ratios (Fig. 4.2), which can be explained by the limitations of XFOIL for calculating cases with very small Reynolds numbers ( $Re < 10^5$ ) and the omission of rotational effects in the airfoil data. For most of the analysed points an underprediction of torque values is expected from potential flow solvers, like UPM or RAMSYS, caused by the neglect of viscosity effects. A post-processing correction in UPM estimating the contribution of profile drag, considerably improved the agreement between calculated and measured torque values. The assumption of

---

<sup>3</sup>Parts of this chapter were published in [77].



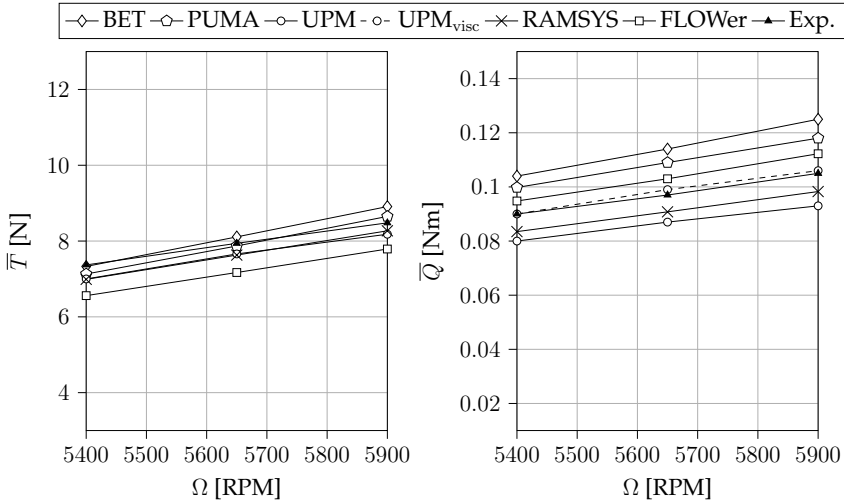


**Figure 4.1:** Effect of varying rotational speed on rotor thrust and torque at fixed tilt angle  $-10^\circ$  and flight velocity  $12.9 \text{ m/s}$

inviscid flow led to an underestimation of torque by at least 10% for most of the cases presented.

With the rotor tilted nose-up, the interaction with vortices becomes dominant and the lines from BET and PUMA diverge, as the BET code did not include a wake model in the solution (Fig. 4.3). Nevertheless, the BET torque estimation was closer to the experimental data at higher positive tilt angles. This counter-intuitive result could arise from the sensitivity of PUMA solver to airfoil data imperfections for the cases with intensified blade-wake interactions, which did not affect basic BET calculations.

The increase in interaction effects between positive and negative rotor tilt angles can be observed in Fig. 4.4 presenting wake visualisations and from unsteady loads depicted in Fig. 4.5. For negative tilt angles, as in Fig. 4.4a, the horizontal component of the velocity induced by the rotor is in the direction of the free stream velocity and the vertical component pushes the wake downwards away from the rotor. This combination of velocities causes a rapid convection of the wake downstream. As a consequence, there is little interaction between the wake and the rotor, the unsteadiness is moderate and so are the effects on the loads acting on the rotor disc (Fig. 4.5a). Figure 4.4b shows the wake developed at a positive tilt angle. In this case, the horizontal component of the velocity induced by the rotor is opposite to the free stream velocity. This not only reduces the convection process downstream but also

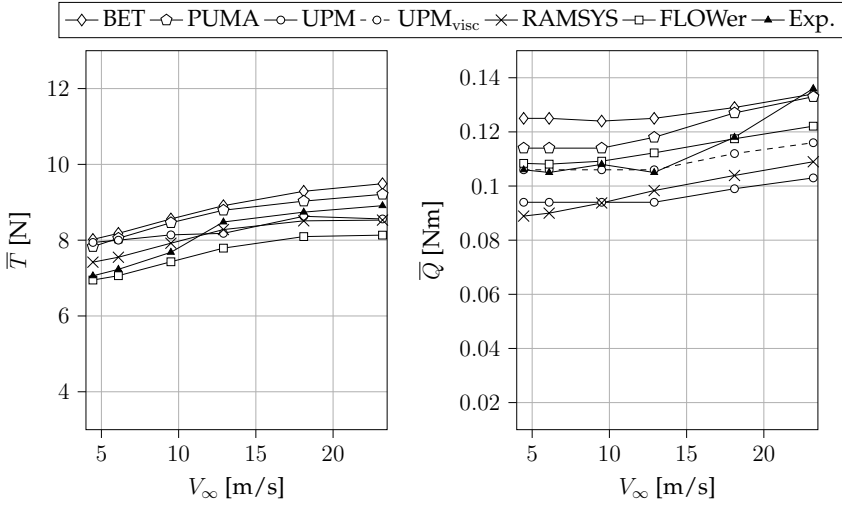


**Figure 4.2:** Effect of varying flight velocity on rotor thrust and torque at fixed tilt angle  $-10^\circ$  and rotational speed 5900 RPM

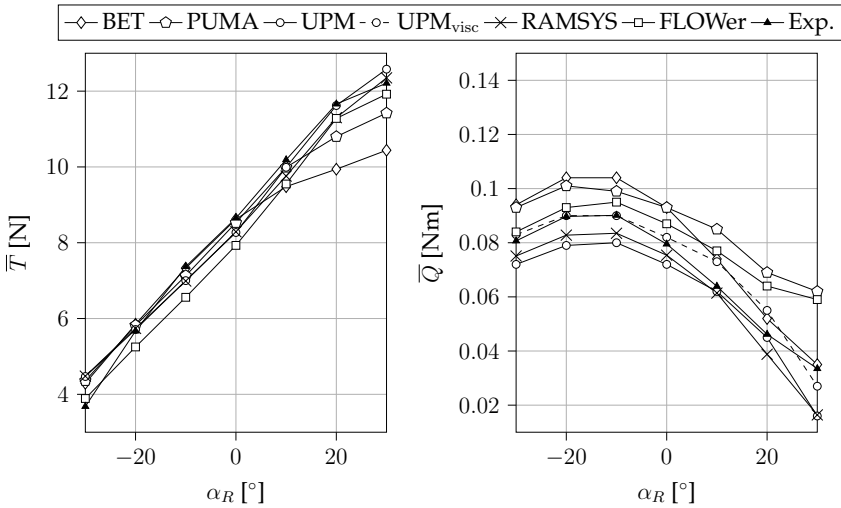


**Figure 4.3:** Effect of varying tilt angle on rotor thrust and torque at fixed rotational speed 5400 RPM and flight velocity 12.9 m/s

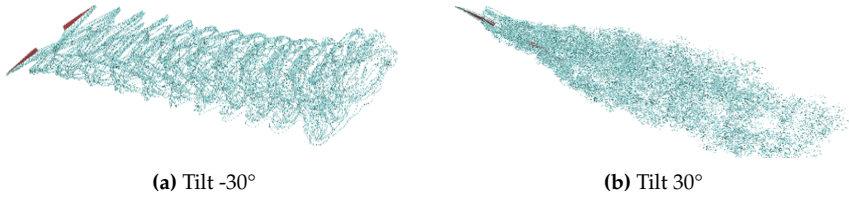


**Figure 4.4:** Rotor wake system development for different tilt angles (RAMSYS)

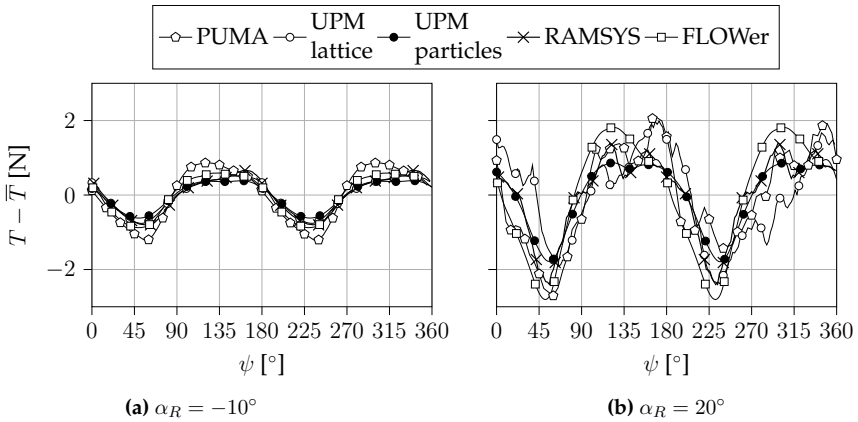


**Figure 4.5:** Thrust fluctuations during one rotation for rotational speed 5400 RPM and flight velocity 12.9 m/s

causes the wake to be fully ingested by the rotor disc with the resulting generation of high interaction effects giving rise to unsteady loads (Fig. 4.5b). The flight regime of a rotor operating in strong upwash transitions towards the windmill state, where the blades are driven by the flow, explaining the rapid decrease in torque values in Fig. 4.3.

Additionally, Fig. 4.5 presents a comparison of unsteady loading for chosen tilt angles calculated in UPM with vortex lattice and vortex particles. Although the discrepancy between the time-averaged thrust values calculated with these both methods was negligible, an apparent difference can be noticed in thrust fluctuations for positive angles of attack (here 20°), for which the particle method offers a more stable solution. This can be explained by the lower sensitivity of the point vortices in the particle method to interactions with solid bodies due to the lower order modelling of the vortical flow compared to the vortex lines in the lattice representation.

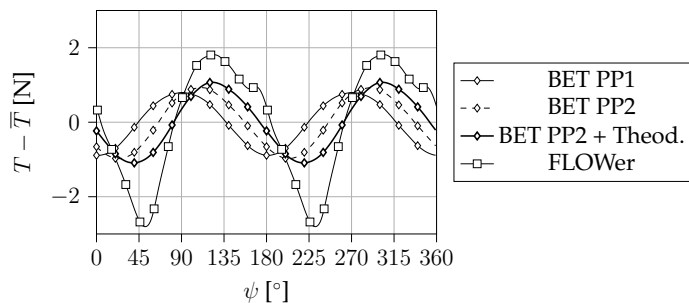


**Figure 4.6:** Time signal of thrust for tilt  $20^\circ$  during one rotation with 5400 RPM and flight velocity 12.9 m/s

The increase in loading fluctuations due to wake interactions cannot be captured by the BET method, as shown in Fig. 4.6 compared to the FLOWer result. Moreover, the loading calculated using BET differs in phase compared with results from other methods, whereby the observable shift depends on the assumptions of the inflow model. While for a trimmed helicopter rotor it is justified to neglect the influence of the rolling moments in the applied model by Pitt and Peters (result PP1 in Fig. 4.6), the forces produced by a fixed-pitch UAV rotors in forward flight are always unbalanced between the retreating and advancing sides. This means that for the latter, a simplified linear model with a longitudinal gradient of the induced velocity should be replaced by a Pitt and Peters model including both longitudinal and lateral components based on the aerodynamic rolling and pitching moments as shown in Fig. 3.5 (result PP2). For the assumption PP1, according to the BET, the maximum thrust is reached around azimuth  $90^\circ$ , which is where the calculated relative velocity coming from the rotational motion of the blade and flight velocity reaches the highest value. In case of PP2, including the lateral inflow gradient, the maximum peak appears around  $20^\circ$  later, more to the front of the rotor, which agreed better with the results from other methods. The remaining phase offset was due to unsteady effects not covered by a simplified linear inflow model. The phase delay could be partially corrected by means of Theodorsen's theory, which accounts for the unsteady development of lift, as described in [88]. In Fig. 4.6 the phase shift resulting from Theodorsen's function was averaged across the disc for each blade section and used to correct the initial result. The applied correction helped to include a case-dependent time delay in the BET solution; however, it did not ensure complete agreement with other solvers. In this study, the Theodorsen's function served only as a quick estimation, as the main objective was to estimate the possible effects of the basic BET assumptions.

## 4.2 Noise prediction

The aerodynamic results indicate that the effect of the tilt variation, with the other parameters held fixed, had the largest effect on the rotor loads (compare Fig. 4.1, 4.2 and 4.3). For this reason, the aeroacoustic study was focused on cases with a constant velocity of 12.9 m/s and a rotation speed of 5400 RPM with a range of rotor tilt angles, as analysed in Figure 4.3. Noise carpets were generated based on the calculated loads, using several acoustic solvers described in Section 4. The focus of the analysis was put on the blade passing frequency as it had a dominant influence on the noise levels.

The noise directivity pattern for the nose-down tilt cases was similar for all of the computational methods (Fig. 4.7). However, the accuracy of the results depended on fidelity levels of the tools used, with the ACCO solution being closest to the experimental data. The noise carpet calculated with BET+FW-H showed qualitative agreement with the other methods in terms of the noise directivity and the position of the maximum noise level. This indicates that the wake had no great influence in this range of tilt angles and the phase discrepancy observed for the unsteady load calculated with BET did not considerably affect the quality of the result.

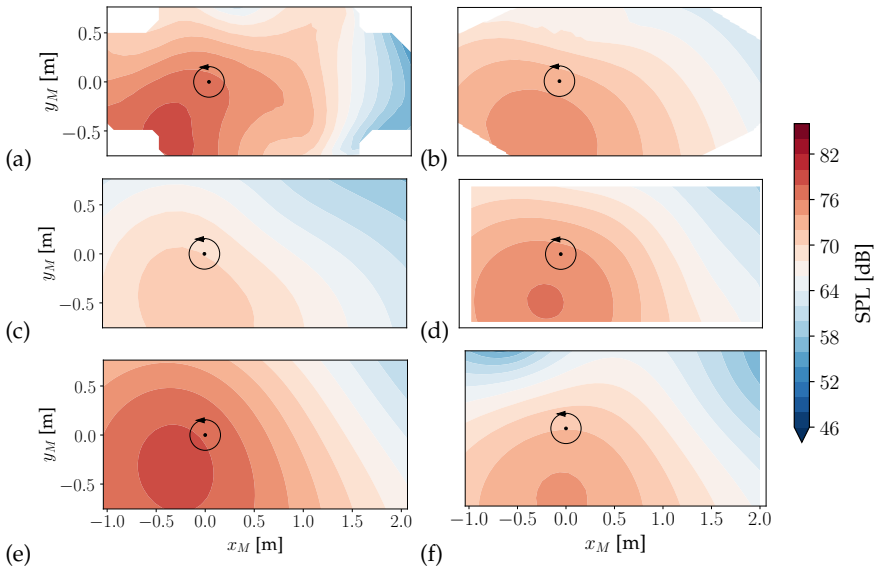


**Figure 4.7:** Noise carpets of the BPF, 5400 RPM, flight velocity 12.9 m/s, tilt angle  $-10^\circ$ . (a) Experiment, (b) UPM+APSIM, (c) BET+FW-H, (d) FLOWer+ACCO, (e) PUMA+KIM, (f) RAMSYS+ACO

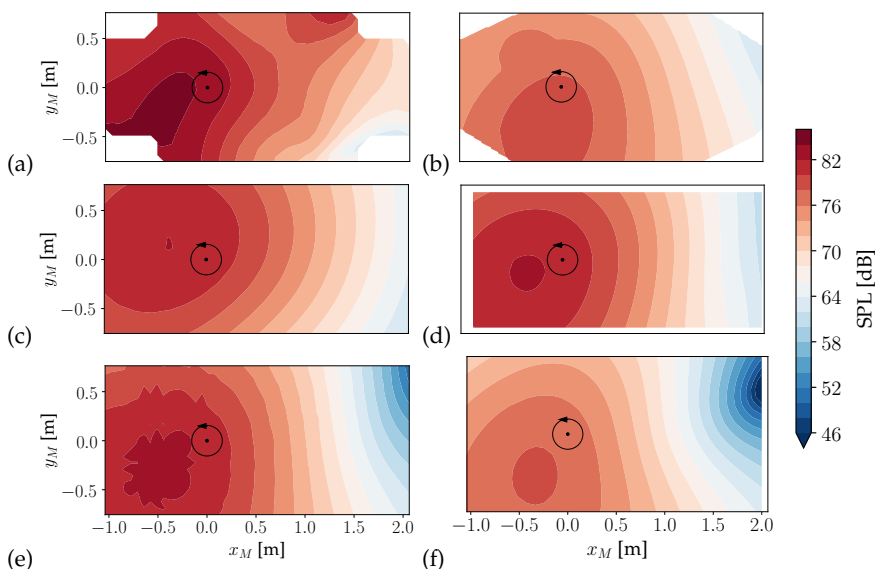


**Figure 4.8:** Noise carpets of the BPF, 5400 RPM, flight velocity 12.9 m/s, tilt angle  $20^\circ$ . (a) Experiment, (b) UPM+APSIM, (c) BET+FW-H, (d) FLOWer+ACCO, (e) PUMA+KIM, (f) RAMSYS+ACO

As expected, for higher positive tilt angles the loading increased and so did noise levels on all calculated carpets. However, the difference in directivity between the outcome of BET and other methods can be noticed (Fig. 4.8). This tendency no longer occurred for the highest nose-up tilt of the rotor as presented in Fig. 4.9. An explanation of this phenomenon can be found in vortex trajectories detected in BOS pictures and also visible in UPM visualisations (Fig. 4.10). The marked positions of the tip vortices for moderate positive tilt angles were always located in the proximity of the blades, strongly affecting rotor loading (Fig. 4.10a, 4.10b). For  $30^\circ$  the vortices tend to move away from the rotor plane, therefore, the result of BET neglecting the wake influence again agreed with the measurement. This observation could also explain why the highest noise levels were measured for a tilt angle of  $20^\circ$  even though the highest loading can be observed for  $30^\circ$  tilt.

With the rotor tilted nose-up, more differences in the calculated noise levels can be observed between the analysed methods, which is related to the increased unsteadiness in the flow and the decrease in the stability of the numerical solutions. For these cases, a discrepancy can also be observed between the aeroacoustic results based on solutions prepared with vortex lattice and vortex particles in UPM (compare

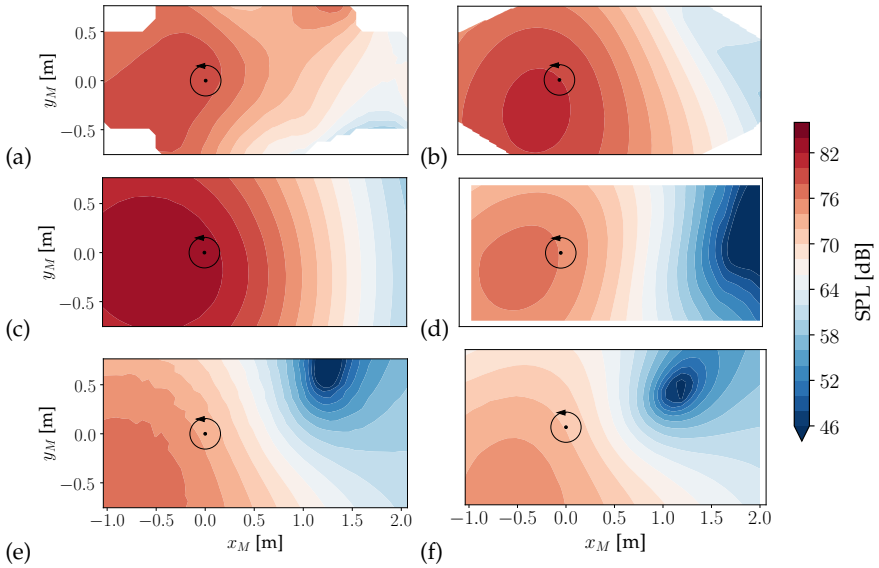


**Figure 4.9:** Noise carpets of the BPF, 5400 RPM, flight velocity 12.9 m/s, tilt angle 30°. (a) Experiment, (b) UPM+APSIM, (c) BET+FW-H, (d) FLOWer+ACCO, (e) PUMA+KIM, (f) RAMSYS+ACO

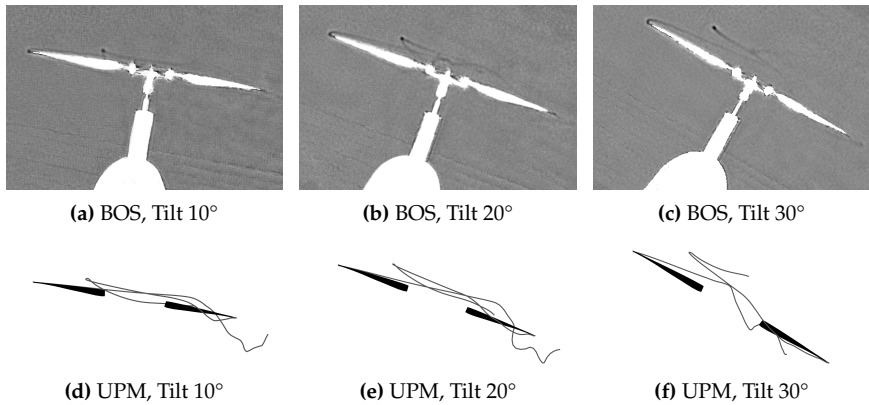


**Figure 4.10:** Vortex trajectories detected in BOS pictures and UPM wake visualisations

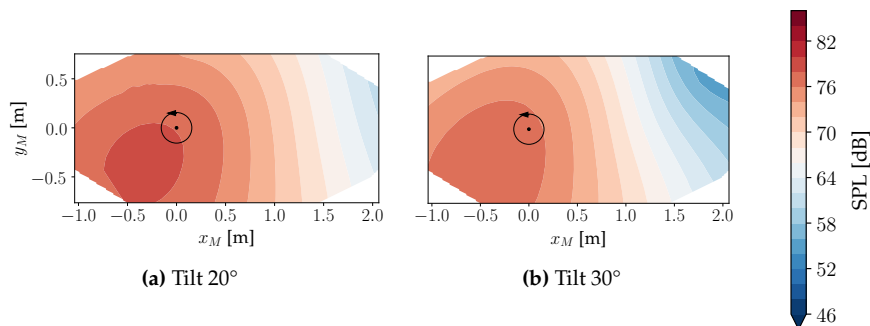


**Figure 4.11:** Noise carpets from UPM with particle wake + APSIM

Figures 4.8b and 4.9b with 4.11), as high time derivatives of the thrust did not appear in the latter (Fig. 4.5).

### 4.3 Scattering effects

Although the calculated noise carpets showed satisfactory agreement with the experimental data in the vicinity of the rotor, none of them fully captured the measurement results, with the largest deviations observed further behind the rotor. Reasons for this can be found by evaluating the influence of scattering effects at the aerodynamic shielding, rotatable rotor base and ground.

#### 4.3.1 Influence of the shielding

An acoustic study was carried out to observe the influence of the scattered field caused by the aerodynamic shielding placed beneath the rotor during the measurements. For 5400 RPM and velocity 12.9 m/s a case with tilt angle of  $-10^\circ$  was chosen for the investigation as in these conditions rotor wake was expected to interfere the most with the shielding. Calculations were conducted using ScatMan tool described in Section 3.2.6 with an assumption of a hard shielding surface ( $v_n = 0$ ).

Figure 4.12 shows that acoustic wave reflection caused an increase of up to 2 dB for the BPF on the upstream side of the shielding surface, as well as decrease of around the same value on the downstream side. However, as the dimensions of the shielding are an order of magnitude smaller than the wavelength of the blade passing frequency (3.8 m) sound waves reflected by the shielding caused a negligible deviation in the noise field, which can be observed comparing Figure 4.13 with the baseline numerical



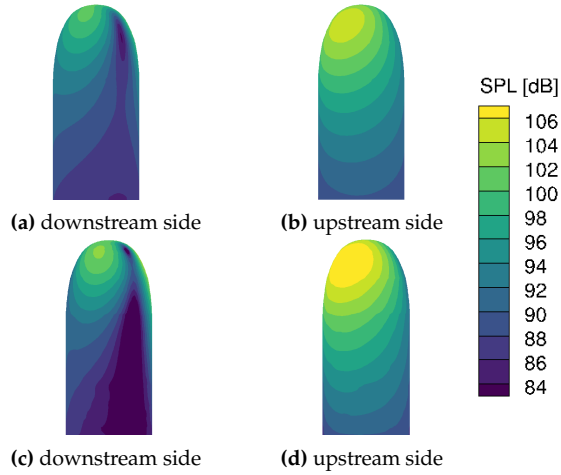


**Figure 4.12:** Acoustic field for the BPF on the shielding surface including incident noise (a), (b) and the sum of incident and scattered noise (c), (d); rotational speed 5400 RPM, flight velocity 12.9 m/s, tilt angle  $-10^\circ$

approach in Figure 4.7d. Additionally, as the presence of the shielding did not cause a change of more than 3% in the thrust values computed for chosen cases in UPM, the baseline approach to neglect its aerodynamic and aeroacoustic influence in the calculations is justifiable.

### 4.3.2 Installation and ground proximity effects

Further scattering effects were evaluated using ACO-FAM solver as described in Section 3.2.5. The computational setup included the part of the ground and the platform on which the rotor was mounted and Fig. 4.14 depicts the mesh surfaces involved in the BEM calculation. More specifically, the blue surface represents the platform, the bottom black surface is the ground and the green surface is the microphone carpet. The discretisation of the elliptic FW-H boundary surface surrounding the rotor, in black, is shown in detail in Fig. 4.15. All surfaces have been discretized to guarantee at least 6 points per wavelength at the maximum frequency of interest.

Firstly, the aerodynamic pressure solution on the isolated rotor blades was computed by RAMSYS and used by the solid formulation of ACO-FWH to calculate the acoustic pressure and its normal derivative on the elliptical surface surrounding the rotor (Fig. 4.15), the latter being achieved by the automatic numerical differentiation explained in Section 3.2.5. Then, the FW-H surface was used by the BEM code to

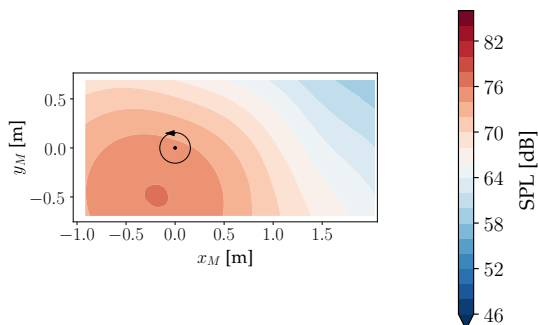


**Figure 4.13:** Noise carpet including total (incoming and scattered by the shielding) sound pressure level of the blade passing frequency - FW-H + ScatMan for 5400 RPM, flight velocity 12.9 m/s, tilt angle  $-10^\circ$

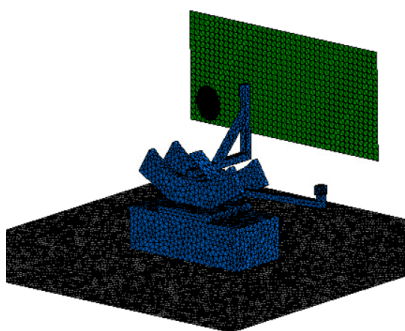


**Figure 4.14:** Acoustic mesh for BEM calculation

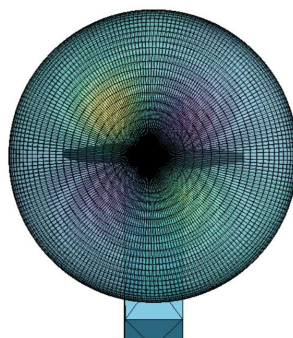


**Figure 4.15:** Integration surface for FW-H and BEM

compute the incident field and the scattering surfaces (ground and the platform) were treated as rigid walls. Calculations were performed for tilt angles  $-10^\circ$  and  $20^\circ$ , 5400 RPM and flight velocity 12.9 m/s. As the dimensions of the analysed objects are of the order of the acoustic wavelength, their influence can be observed in the noise carpets of the blade passing frequency. The acoustic fields including scattering effects (Fig. 4.16) show a visible difference in both noise directivity and noise levels compared to the baseline results from Fig. 4.7f and Fig. 4.8f. Nevertheless, the differential maps in Fig. 4.17 indicate no significant improvement in the agreement with the measurements. The slight improvement in the results due to the inclusion of reflections is limited to the area on the advancing side of the rotor for both tilt angles.

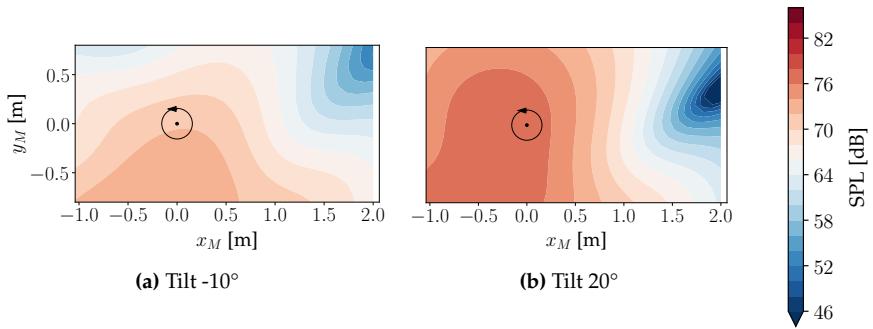


**Figure 4.16:** Noise carpets including scattering effects for 5400 RPM and flight velocity 12.9 m/s

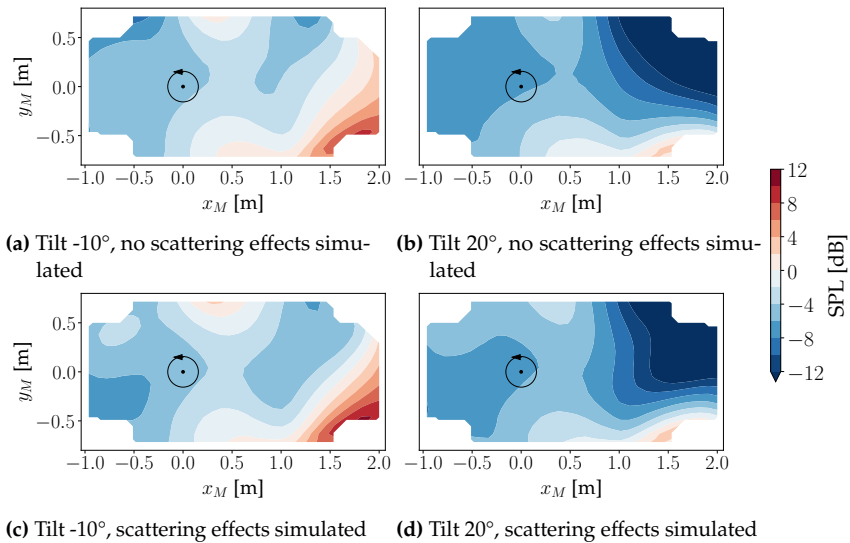


**Figure 4.17:** Noise carpets showing the difference between SPL calculated with RAMSYS+ACO and measured; 5400 RPM and flight velocity 12.9 m/s

## 4.4 Summary

The performed aeroacoustic and aerodynamic calculations showed that in most cases the measurement results were reproducible with satisfactory agreement by all the computational methods, regardless of their fidelity level. The simplest and most time-efficient BET shows compatibility with other tools for moderate flight velocities and rotor tilt angles, when it comes to time-averaged results, yet the code is not a reliable tool for reproducing transient loading. The BET approach loses credibility in cases where a three-dimensional wake influence becomes dominant, such as flow with a nose-up tilt of the rotor. An accurate result for such conditions can be achieved with methods including the wake in the solution, of which codes incorporating viscous effects (such as FLOWer, UPM with particle wake) offer more stability. The BET solution regained applicability for the highest analysed positive tilt angle of  $30^\circ$ , when wake vortices move further downstream of the blades.

The airfoil characteristics used in BET and PUMA allow the inclusion of the influence of compressibility and viscosity in the solution. However, one must be aware of XFOIL limitations in terms of accuracy for low Reynolds numbers and the lack of consideration of rotational effects in this approach.

Mid-fidelity solvers based on potential flow (UPM, RAMSYS) ensured high accuracy of thrust values for cases, where the blades do not operate at stall conditions. However, the assumption of inviscid flow leads to significant underprediction of torque. A simple post-processing correction accounting for profile drag significantly improved the quality of results.

Except for the BET+FW-H solution for  $20^\circ$  tilt angle, the calculated noise carpets of the blade passing frequency agreed with the measurement when it comes to the location of the highest noise level. Deviations in the results were more apparent for positive tilt angles and occurred in the area further downwash behind the rotor hub. Objects such as the rotor base or the ground with dimensions comparable to the wavelength caused reflections that affected the acoustic results. Although the noise carpets including scattering effects still do not explain all deviations in the acoustic measurements, they clearly demonstrate the importance of reflection analysis, even at low frequencies.



## 5 Multirotor configurations study<sup>4</sup>

The quadrotor analysis was focused on two tilt angles representing a regular orientation of a multicopter in forward flight ( $-10^\circ$ ) and in a braking mode ( $+10^\circ$ ) (Fig. 5.1). For the latter strong interactions arise from self-induced and mutual effects as rotor wakes propagate in the rotor plane. The main analysis included variation of horizontal spacing between the rotors at different tilt angles extended with an investigation of two-rotor systems. In the next step the impact of the vertical offset between the front and back rotors was studied for selected horizontal spacings depending on the tilt angle. Diamond and square quadrotor configurations were analysed, with a change in rotor rotation direction for the latter (bearhug/breaststroke). Orthogonal rotor phasing was the default in the test cases presented, while an influence of changing to tip-to-tip phasing was discussed separately.

A constant rotational speed of 5400 RPM of all rotors and a flight velocity of 12.9 m/s was maintained for all test points. The conditions analysed correspond to a rotor advance ratio of 0.146 with a tip Mach number of 0.259 and a Reynolds number in the order of  $10^4$  to  $10^5$  across the rotor disc.

The interaction effects were evaluated relative to the results of an isolated rotor based on the differences in the thrust and torque values ( $\bar{T}$  and  $\bar{Q}$ ), which, with the latter implying changes in power consumption, are the most important parameters in assessing the UAV's performance. The rotor efficiency in forward flight was evaluated from the power loading defined as  $\frac{\bar{T}}{\bar{P}} = \frac{\bar{T}}{\omega\bar{Q}}$ .



**Figure 5.1:** Analysed tilt angles for quadrotor configurations

<sup>4</sup>Parts of this chapter were published in [75, 76].

## 5.1 Reference results of an isolated rotor

Selected results of single rotor performance from the measurements and calculations presented in the previous section served as a reference for the analysis of interaction effects in multirotor configurations operating in corresponding flight conditions (Table 5.1).

Knowledge of the velocity field generated by an isolated rotor is crucial for understanding the mutual impact of rotors on each other's performance. Computational results show that the analysed fixed-pitch rotor in forward flight sheds an asymmetric wake due to the imbalance of forces across the rotor disc (Fig. 5.2). With a rotor tilted forward, a strong, wide vortex from the advancing side quickly propagates downward, while a weaker tip vortex from the retreating side remains in the vicinity of the blades. The effect is also visible in the induced velocity field captured by the PIV in Fig. 5.3, with a strong advancing side downwash inboard (in blue) and asymmetric upwash regions (in orange) on the outboard blade areas resulting from the rolled-up tip vortices from both sides. All of these features influence the interaction effects between the rotors depending on their mutual positions.

		Experiment	UPM	FLOWer	RAMSYS	PUMA	CORAL
Thrust [N]	-10°	7.37	7.13	6.43	7.048	7.13	6.41
	+10°	10.19	10.08	9.38	9.73	9.91	9.09
Torque[Nm]	-10°	0.09	0.081*	0.095	0.083*	0.099	0.074*
	+10°	0.064	0.057*	0.075	0.061*	0.082	0.055*

\*inviscid

Table 5.1: Thrust of a single rotor, 5400 RPM,  $V_\infty=12.9$  m/s

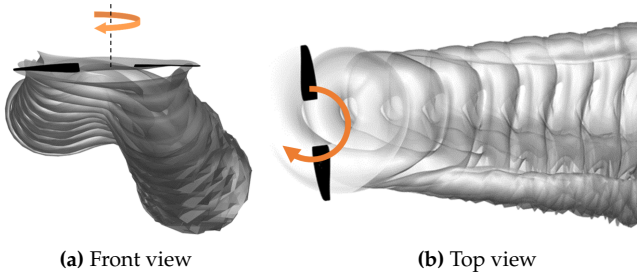


Figure 5.2: Wake of an isolated rotor at a tilt angle -10° visualised in UPM

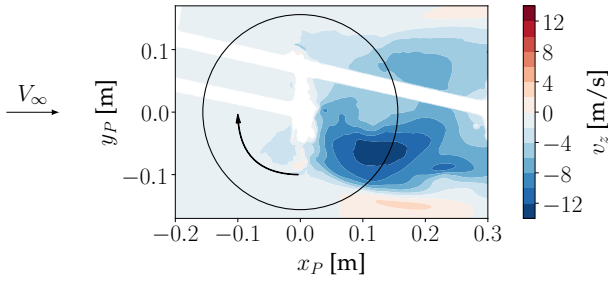


Figure 5.3: Downwash of a single rotor captured with PIV for tilt  $-10^\circ$

## 5.2 Two-rotor configurations

The analysis of two-rotor configurations served to improve the understanding of the nature of the interaction effects and to provide an initial assessment of the ability of selected solvers (UPM and FLOWer) to reproduce these effects. Therefore, the influence of variations in tilt angle and rotor spacing on the rotor performance was primarily investigated. The selected alignments of two rotors represent parts of quadrotor systems in square and diamond configurations (Fig. 5.4-5.6).

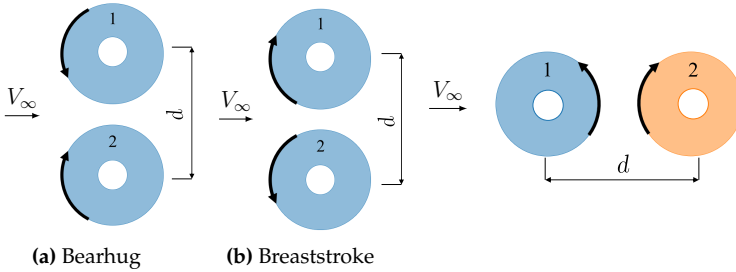


Figure 5.4: Rotors side-by-side

Figure 5.5: Tandem

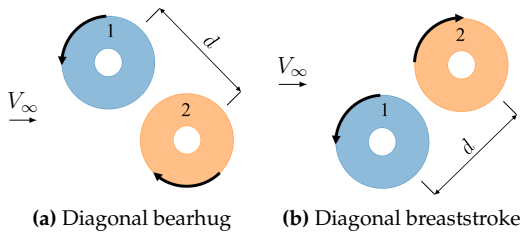


Figure 5.6: Rotors in oblique alignment



The observed changes in rotor performance due to interactions were explained based on velocity fields measured with PIV.

### 5.2.1 Side-by-side alignment

Two counterrotating rotors were aligned side by side with either their advancing or retreating sides meeting, forming the bearhug or breaststroke configuration respectively (Fig. 5.4). By definition this system is symmetrical relative to the flow, so the same effects affect each rotor. Therefore, the presented results apply to both rotor 1 and 2. The side by side arrangement has a beneficial influence on rotor performance (Fig. 5.7) with up to 10% thrust gain and about 20% torque reduction compared to an isolated rotor case for  $d/D = 0.96$ . The effect is the strongest at  $\alpha_R = 10^\circ$  with wakes passing the rotor plane and weakens as the vortices propagate higher at increased nose-up tilt. The potential solver UPM shows good agreement with experimental results and FLOWer as for the thrust increase evaluation, while it tends to strongly overestimate the interaction effects on torque at high positive tilt angles.

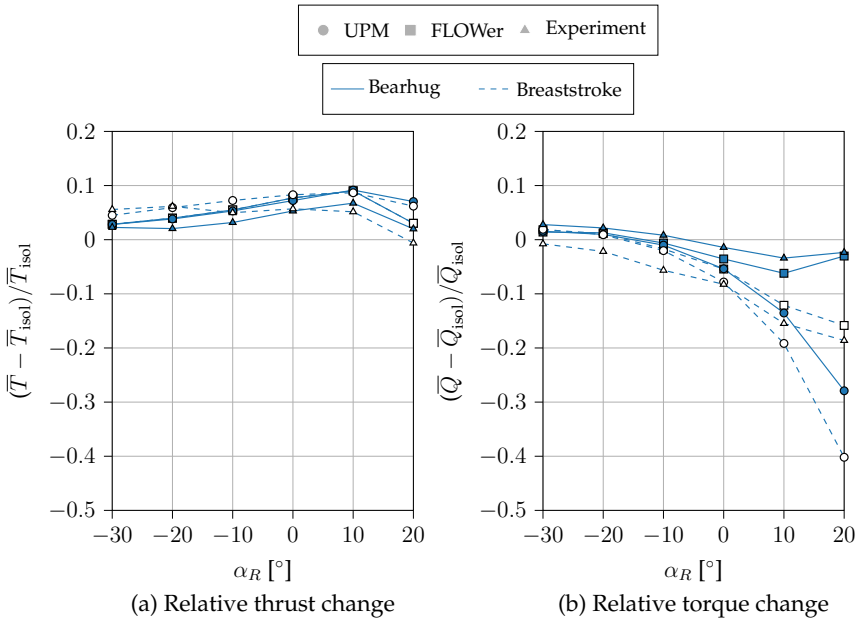


**Figure 5.7:** Effects of varying tilt angle on rotor performance in the side-by-side alignment for  $d/D=0.96$

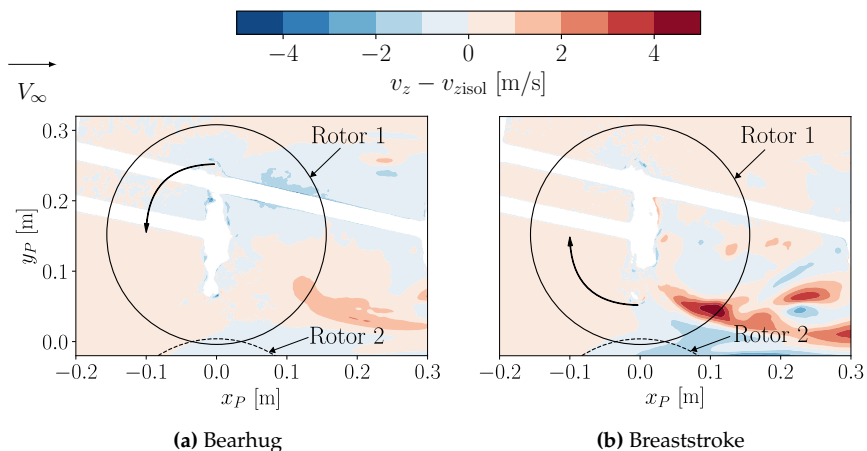


**Figure 5.8:** Upwash regions between the rotors in side-by-side interaction, captured with PIV relative to an isolated rotor measurement for  $d/D = 0.96$  and  $\alpha_R = -10^\circ$

The velocity distribution shown in Fig. 5.8 with respect to an isolated rotor shows upward flow regions between the rotors (in red) caused by an interaction of their rolled-up tip vortices. The generated upwash leads to a simultaneous increase in thrust and decrease in induced drag at neighbouring azimuthal positions for both rotors (Fig. 5.9, 5.10). Differences between the bearhug and breaststroke results are apparent for high-interaction cases such as closer rotor positions and positive tilt angles, where the breaststroke configuration, with stronger advancing side vortices interacting (Fig. 5.8b), is more favourable. Considerable beneficial effects occur for very close rotor spacings around  $d/D = 1$  (compare Fig. 5.9a, 5.9b), yet a deeper overlap of the blades causes detrimental interactions with the inboard downwash of the neighbouring rotor.

## 5.2.2 Tandem

In a tandem configuration rotor 2 is positioned behind rotor 1 relative to the flight direction (Fig. 5.5). As shown in the PIV plane in Fig. 5.11, the front of rotor 2 is affected by the downwash from rotor 1 (in blue), while at  $90^\circ$  and  $270^\circ$  azimuth it may locally operate in the upwash from the tip vortices of the preceding rotor (in orange).

The proximity to rotor 2 has a beneficial, yet negligible impact on the front rotor's performance as shown for  $d/D=1.2$  (Fig. 5.12). On the other hand, even for cases with a nose-down tilt of the rotor plane, rotor 2 is heavily affected by the downwash of the

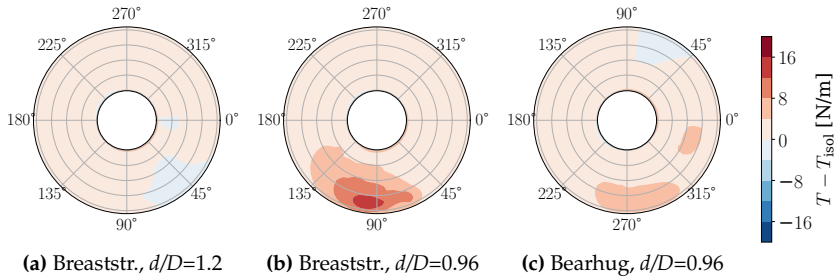


**Figure 5.9:** Effect of side-by-side alignment with tilt  $-10^\circ$  on thrust of rotor 1 (UPM)

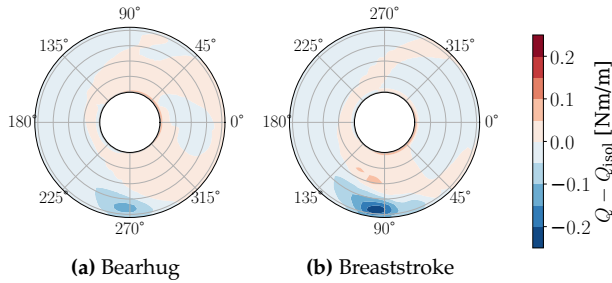


**Figure 5.10:** Effect of side-by-side alignment with tilt  $-10^\circ$  on torque of rotor 1,  $d/D=0.96$  (UPM)

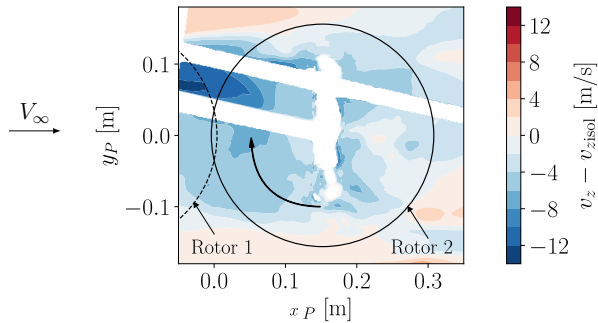


**Figure 5.11:** Change in downwash of rotor 2 in tandem interaction relative to an isolated rotor, captured with PIV for  $d/D = 0.96$  and  $\alpha_R = -10^\circ$

preceding rotor causing a considerable reduction in its efficiency with a minimum 10% loss. The interaction effects intensify with decreasing distance between the rotors, however, the increase in tilt angle has a greater influence, leading to a thrust reduction

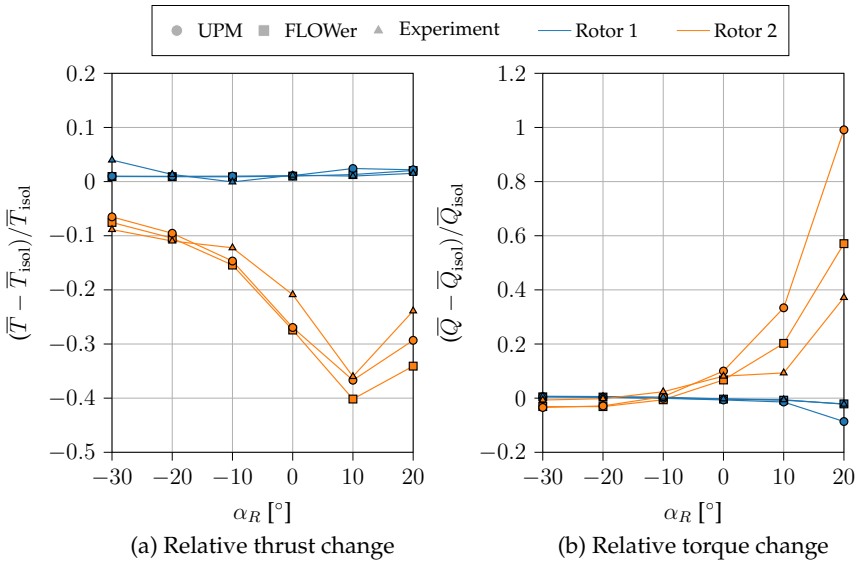


**Figure 5.12:** Effects of varying tilt angle on the rotor performance in tandem for  $d/D = 1.2$

of roughly 40% for rotor 2 at  $10^\circ$  tilt (Fig. 5.12a, 5.13). In this case, rotor 2 is located directly in the wake of the preceding rotor and is affected by the strong downwash, particularly from the advancing side of rotor 1. As the advancing side tip vortex of rotor 1 reaches the plane of the rear rotor an upwash region can be observed around azimuth  $90^\circ$  of rotor 2, yet it does not significantly improve its performance (Fig. 5.13d). At nose-up tilt angles above  $10^\circ$  the detrimental effect on the back rotor begins to diminish again. At  $-10^\circ$  tilt angle, rotor 2 is mainly affected by the retreating side vortex of rotor 1, as it propagates above the advancing side vortex and closer to the rotor plane for nose-down tilt conditions (Fig. 5.13a, 5.13b, 5.13c).

FLOWer and UPM results show similar tendencies as the experiment when it comes to the thrust changes, yet both tools overestimate the relative torque increase for rotor 2 at higher positive tilt angles (Fig. 5.12b).

### 5.2.3 Oblique alignment

In the oblique alignment, rotor 2 is located behind rotor 1, on its retreating side for the ‘diagonal bearhug’ or its advancing side for the ‘diagonal breaststroke’ (Fig. 5.6). The interaction with the tip vortices of the preceding rotor has a positive impact

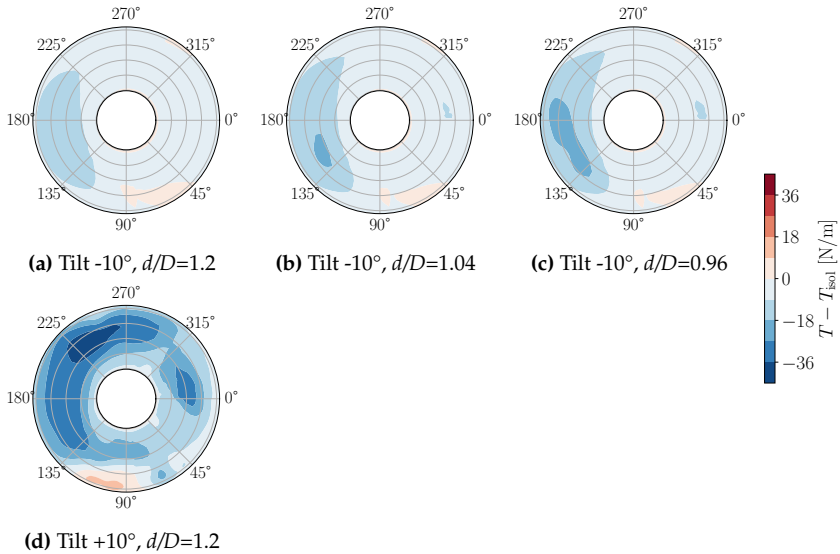


**Figure 5.13:** Effect of tandem alignment on the thrust of rotor 2 (UPM)

on rotor 2 for both configurations, especially at higher nose-up tilt angles up to  $10^\circ$ . (Fig. 5.14c, 5.14d). The effect is greater and observable already for moderate tilt angles for the diagonal bearhug alignment, as the retreating side tip vortex of rotor 1 propagates closer to the rotor plane. The advancing side tip vortex in the diagonal breaststroke configuration produces the strongest upwash on rotor 2 at around  $\alpha_R = 10^\circ$ , leading to the local stall on its blades, which cannot be captured by the potential solver UPM overestimating the positive effect at this angle. The impact of the interaction on the front rotor is less pronounced; however, a slight improvement in its efficiency can be observed with a simultaneous thrust gain and torque reduction of up to 5% for  $20^\circ$  tilt (Fig. 5.14a, 5.14b). In contrast to the front rotor's trend, the interaction effect on thrust of the rear rotor decreases sharply for tilt angles above  $10^\circ$  and for  $\alpha_R = 20^\circ$  its thrust is again comparable to that of an isolated rotor. The decrease in torque of about 5% is still visible in the measurements for this test case.

A positive effect on the rear rotor in the oblique alignment decreases not only at higher positive tilt angles but also at closer rotor spacings as rotor 2 starts to operate partially in the downwash from the inner wake of rotor 1 (blue in Fig. 5.15). The effect is dominant in the diagonal breaststroke configuration due to the influence of a stronger and wider advancing side vortex. As a result, regions of locally reduced thrust and increased torque appear alongside areas with improved efficiency, as

shown for  $0^\circ$  tilt in Fig. 5.16 and Fig. 5.17 for the diagonal breaststroke configuration.

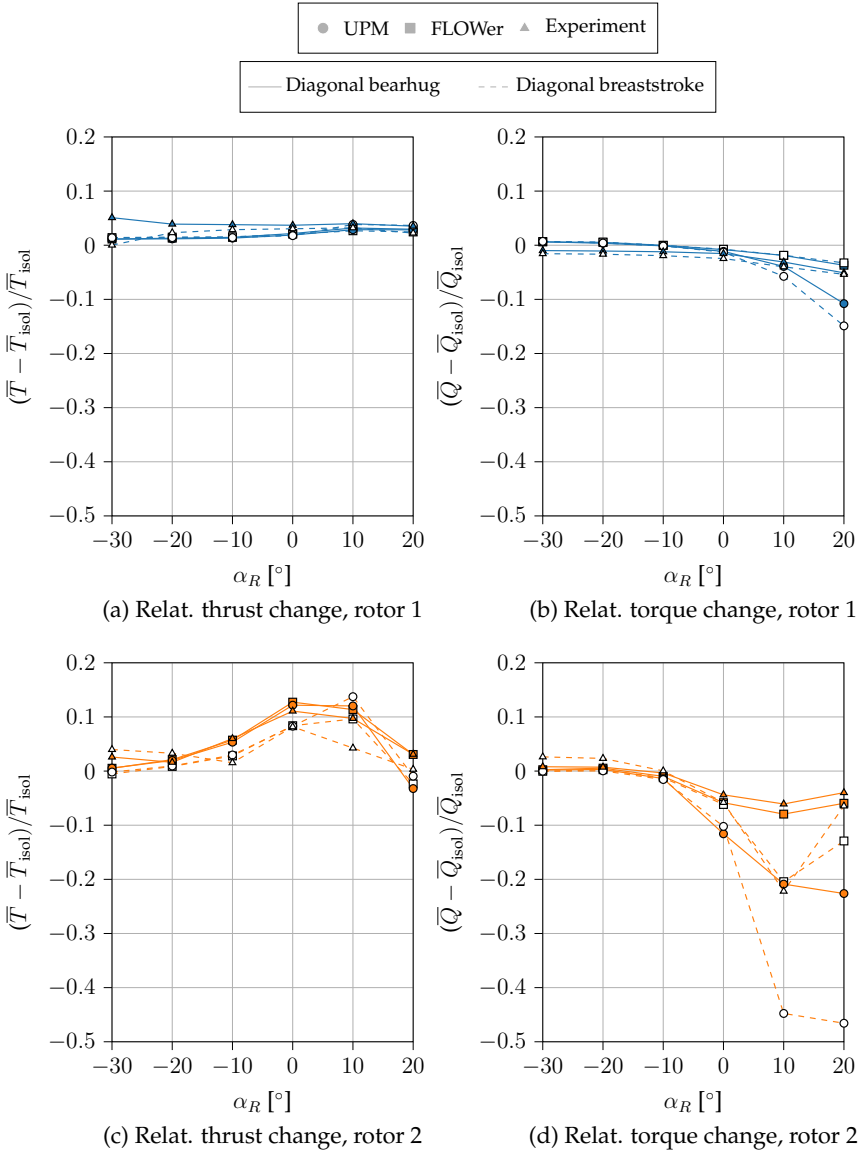


**Figure 5.14:** Effects of varying tilt angle on the performance of rotors in oblique alignment for  $d/D=1.2$

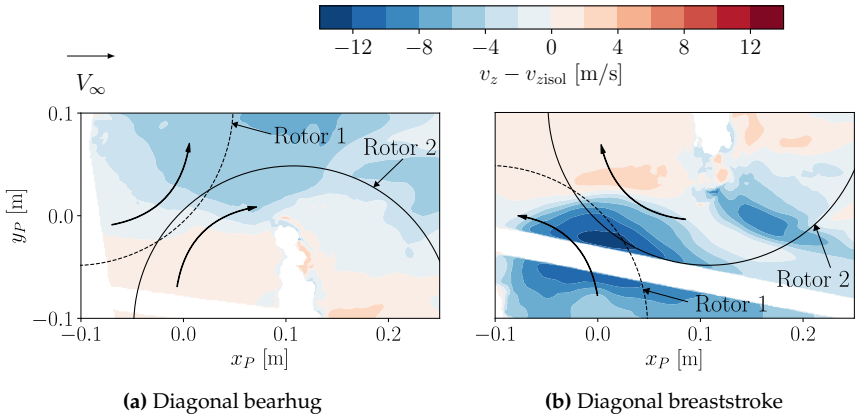


**Figure 5.15:** Downwash of rotor 2 in oblique interaction relative to an isolated rotor, captured with PIV for  $d/D=0.96$  and tilt  $-10^\circ$

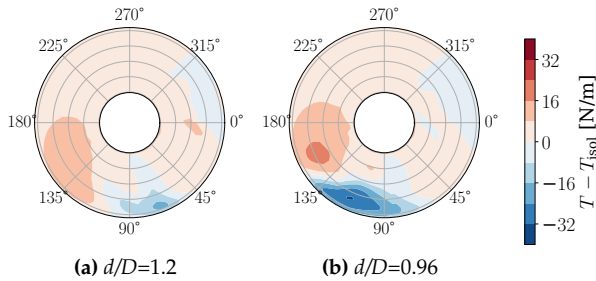


**Figure 5.16:** Effect of diagonal breaststroke alignment with tilt  $0^\circ$  on the thrust of rotor 2 (UPM)

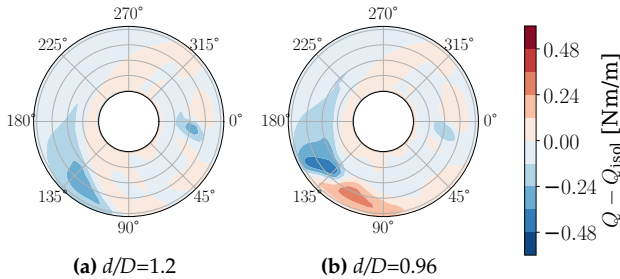


**Figure 5.17:** Effect of diagonal breaststroke alignment with tilt  $0^\circ$  on the torque of rotor 2 (UPM)

### 5.3 Quadrotor configurations

The studied quadrotor configurations included the diamond and square rotor alignments with a change of rotor rotation direction for the latter (bearhug/breaststroke), as shown in Fig. 5.18.

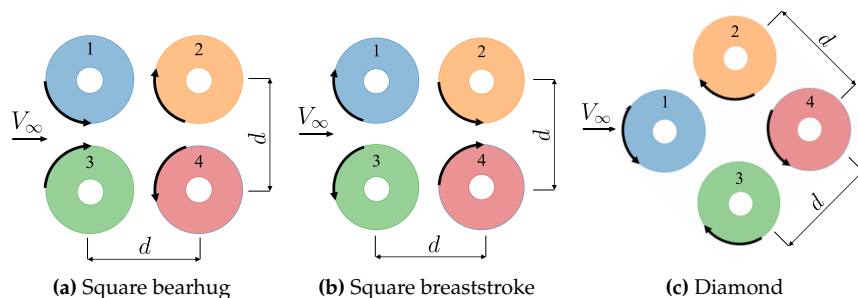


**Figure 5.18:** Analysed quadrotor configurations

The analysis of the interaction effects for each configuration was done based on a comparison of the total thrust and torque generated by the quadrotor system with that obtained for four isolated rotors (Fig. 5.19, 5.20). All the applied computational methods and measurements show the same trends due to the change in hub spacing for a nose-down tilt angle of  $-10^\circ$ , with a maximum difference of 4% between the exact values. The results indicate that the interactions in the square alignment are detrimental for all of the rotor spacings, with a blade overlap of less than  $0.2 D$  being approximately 3% more beneficial than wider rotor separations. Rotor positioning with a deep overlap of  $0.24 D$  leads again to a reduction in thrust of up to 10%, yet also a reduction in torque of around 5% occurs in this case. For larger hub spacings and the nose-down tilt of the rotor plane the interaction effects on torque are negligible.

While a loss of around 4% of thrust can be observed for both square systems already at a spacing of  $1.68 D$ , the bearhug configuration becomes slightly more efficient than the breaststroke configuration as the rotor spacing decreases. At a positive tilt angle of  $10^\circ$ , the performance of both square systems significantly declines for larger rotor spacings due to a 15% thrust reduction and a simultaneous increase in torque of around 10%. Interestingly, the performance of the bearhug and breaststroke configurations improves continuously as the rotor spacing decreases, with the optimum reached at  $0.84 D$ . Moreover, under these conditions the breaststroke configuration shows a better efficiency than the bearhug system.



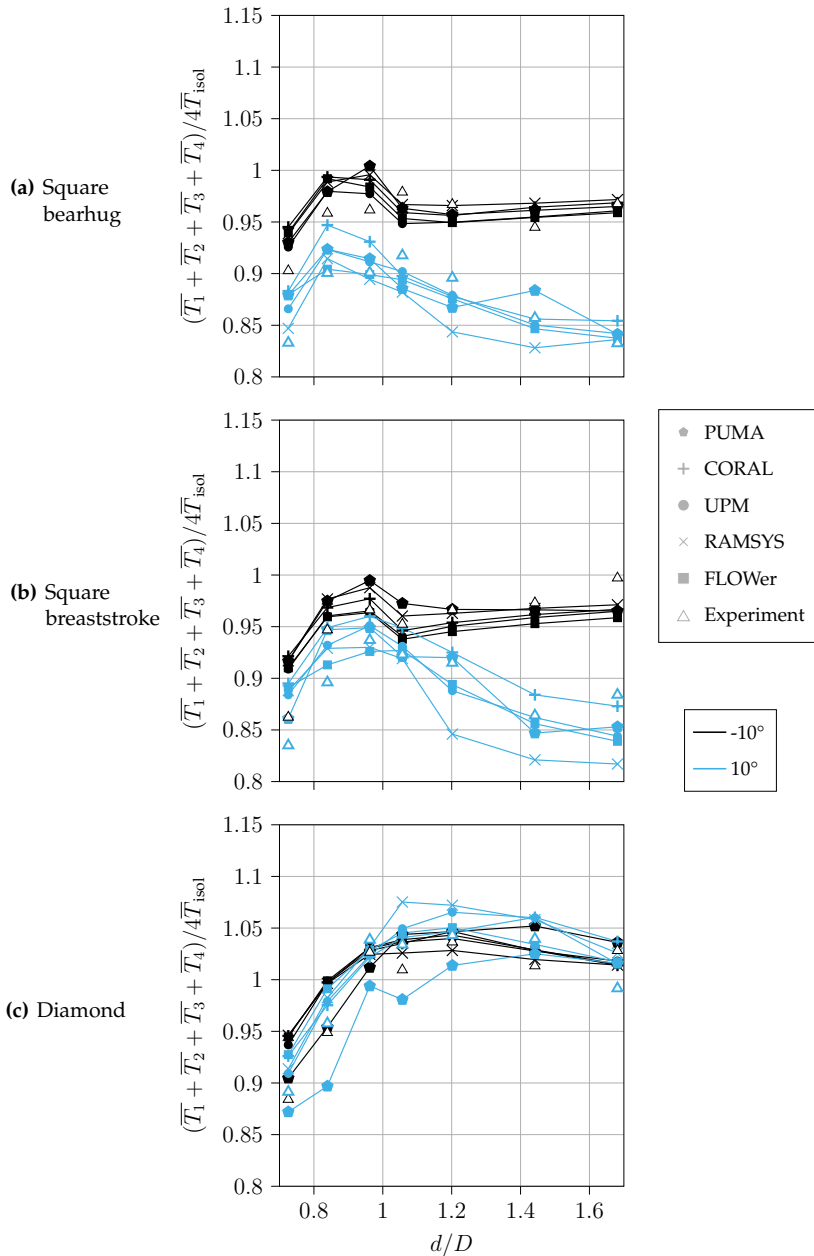


**Figure 5.19:** Change in mean thrust of a quadrotor system with varying rotor spacing

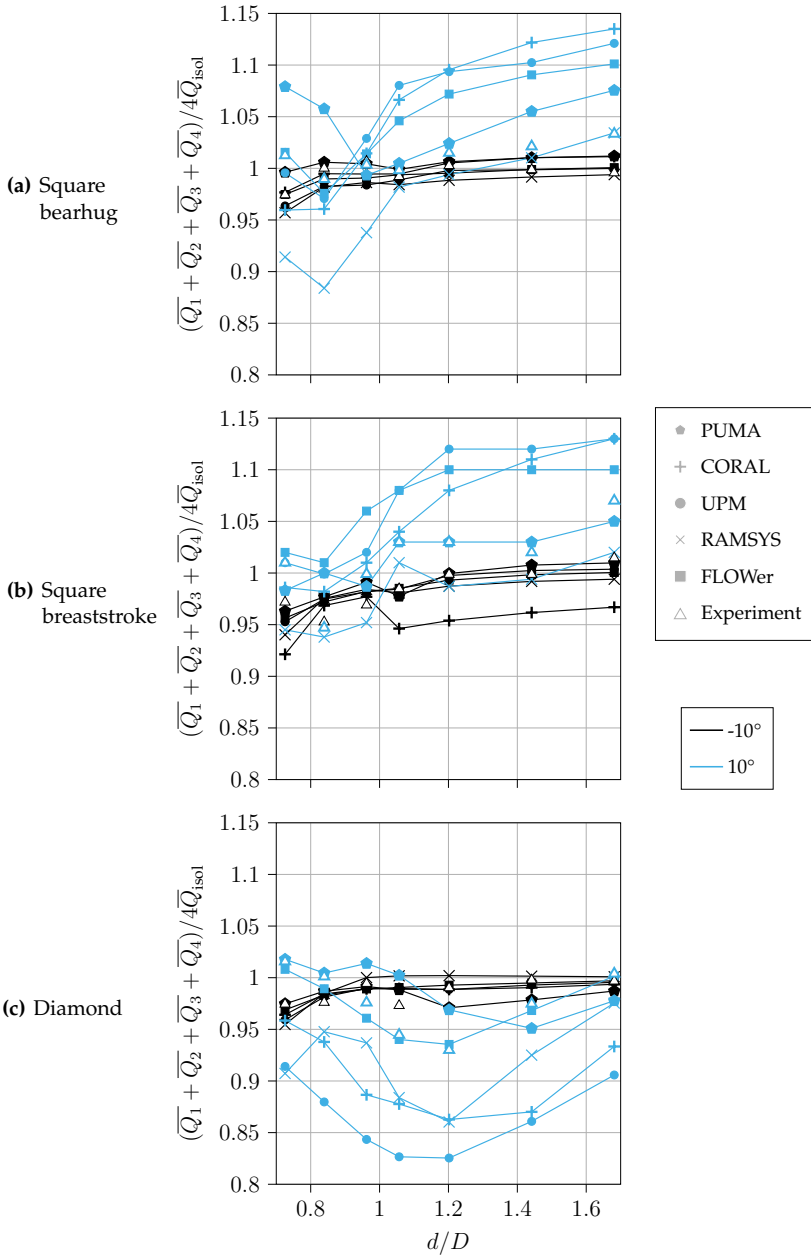


Figure 5.20: Change in mean torque of a quadrotor system with varying rotor spacing

In contrast to the square configurations, the results for the diamond system indicate beneficial interaction effects for rotor spacings larger than  $d/D=0.84$ . The optimum is reached around  $1.2D$ , where the quadrotor produces 5% more thrust than the isolated rotors. As the hub spacing decreases, the performance of the diamond system deteriorates, and for positions with the greatest overlap its efficiency is comparable to that of the square configurations. At  $+10^\circ$  tilt, the effect on rotor thrust remains similar to that of the nose-down tilt case, yet a reduction in torque can be observed with the minimum occurring at a spacing of  $1.2D$ .

Although all computational tools are again in agreement when it comes to capturing the trends at the positive tilt angle, a greater discrepancy is observable in terms of the exact values. The results differ by a maximum of 8% for the thrust change and up to 15% for the torque.

### 5.3.1 Square configurations

The effects described for the quadrotor system can be explained by analysing the performance change of each rotor individually (Fig. 5.21,5.22). As the square alignment is aerodynamically longitudinally symmetric, both the front and both back rotors show the same changes in efficiency due to interaction effects. The system performance is mainly affected by the downwash from the front rotors, which reduces the thrust produced by rotors 2 and 4 by up to 20% at a tilt angle of  $-10^\circ$  (Fig. 5.21a, 5.21b).

Similar to the tandem configuration, decreasing the rotor spacing worsens the performance, yet increasing the tilt angle has a major influence. For a positive tilt angle of  $+10^\circ$  the thrust produced by the rear rotors drops by up to 40% (Fig. 5.21c, 5.21d). Interestingly, at a negative angle for the hub spacings less than  $1.2D$  the efficiency of the rear rotors in the square bearhug configuration is slightly improved compared to the square breaststroke system. For a positive tilt angle, the opposite effect is observed.

The described trend results partially from a change in the wake geometry of the front rotors due to their mutual interaction. As the separation between rotors 1 and 3 decreases, their tip vortices merge into a super-vortex forming a strong upwash region. The combined vortex propagates upwards, which is more pronounced in the bearhug configuration for two retreating side tip vortices interacting (Fig. 5.23). As a result, the downwash effects that degrade the performance of the rear rotors are slightly reduced in the square bearhug system compared to the square breaststroke for  $-10^\circ$  a tilt angle (Fig. 5.24b). At a rotor spacing of  $0.96D$ , the rear rotors reach maximum efficiency due to the side-by-side breaststroke interaction occurring around

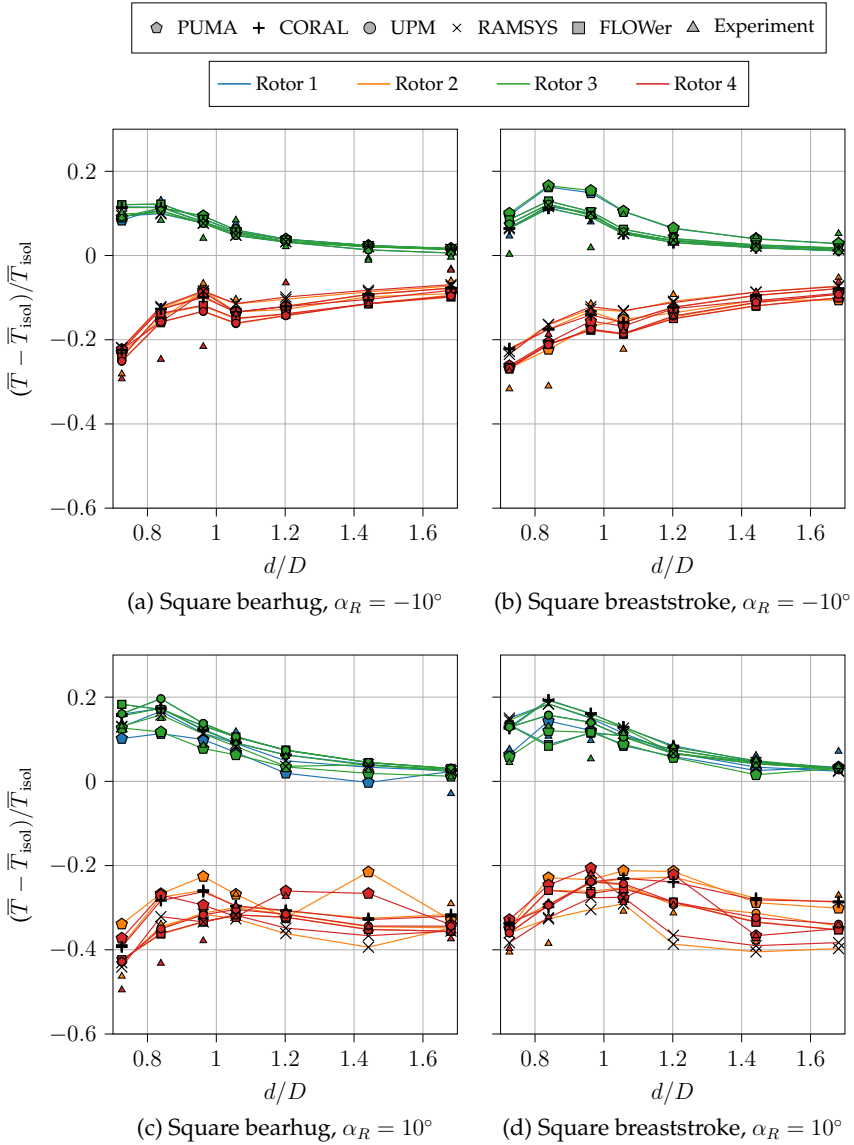


**Figure 5.21:** Change in mean thrust of each rotor in the square configuration with varying rotor spacing

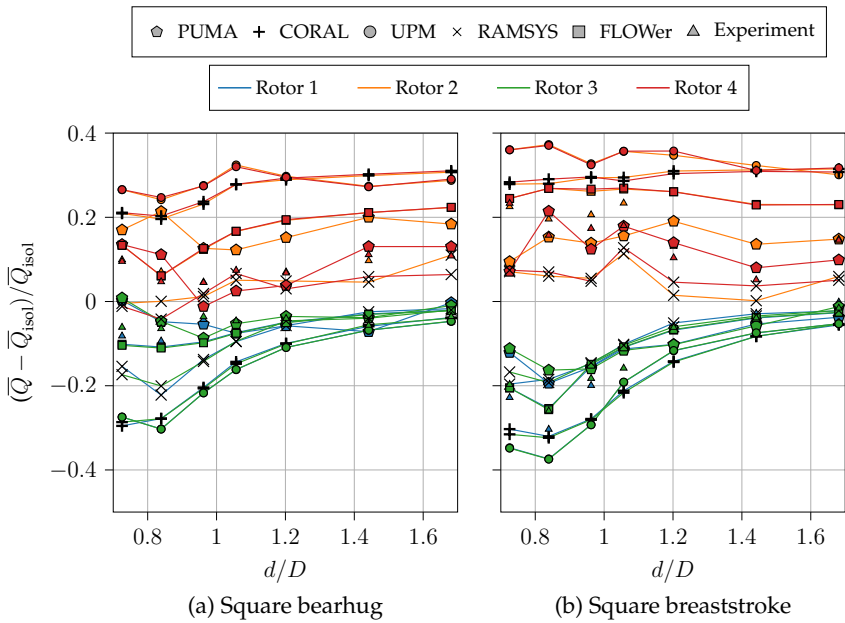


**Figure 5.22:** Change in mean torque of each rotor with varying rotor spacing for tilt angle  $+10^\circ$

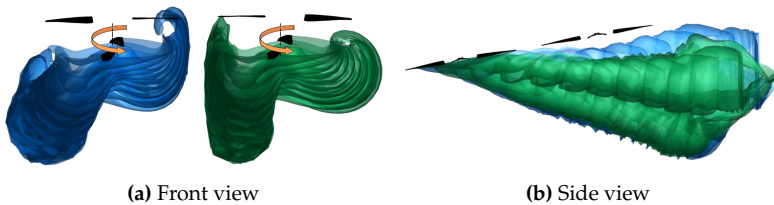


**Figure 5.23:** Comparison of the front rotor wake propagation in square bearhug (blue) and square breaststroke (green)

90° azimuth. A slight improvement in the performance of the rear rotors at this rotor separation also appears for the square breaststroke configuration; however, the side-by-side bearhug interaction between rotors 2 and 4 is weaker, as shown in the two-rotor analysis (Fig. 5.24d). With the rotor separation further decreasing, the performance of rotors 2 and 4 deteriorates sharply as they are more affected by the downwash from the inner wake of the preceding rotor and the rotor on the side (Fig. 5.24c).

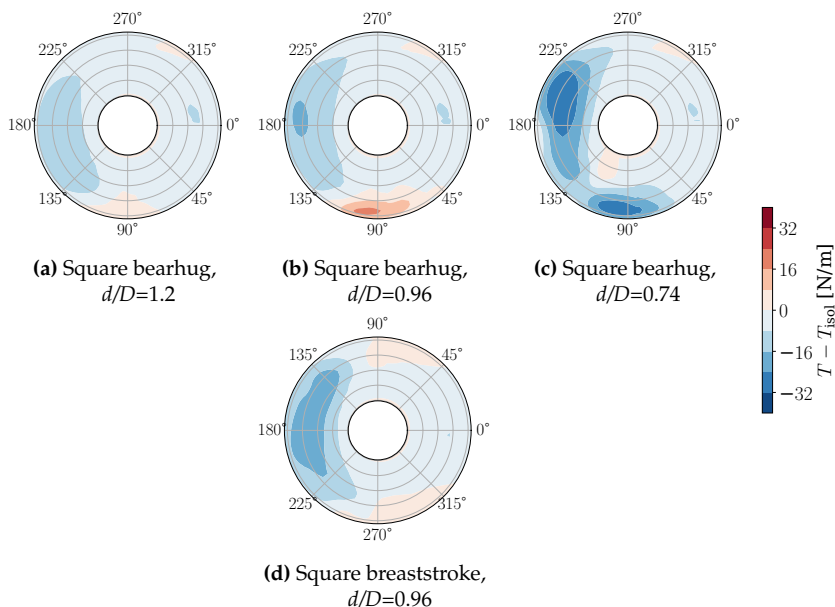


**Figure 5.24:** Change in thrust of rotor 2 in the square configuration with  $-10^\circ$  tilt (UPM)

For tilt angle of  $+10^\circ$ , the difference in the rear rotors' efficiency between the two square configurations results mostly from the interaction with the outer tip vortices of the preceding rotors. In the case of the square breaststroke configuration, the retreating side vortices of rotors 1 and 3 reach the level of rotors 2 and 4, creating an upwash region around  $90^\circ$  azimuth and locally improving the rear rotors' performance (Fig. 5.25b). On the other hand, the wider and stronger advancing side vortex in the square bearhug configuration causes an increased downwash on the rear rotors around  $225^\circ$  azimuth (Fig. 5.25a).

For both square configurations, the results show similar tendencies for the front

rotors and the improvement in their efficiency due to interaction effects. The thrust produced by rotors 1 and 3 increases by up to 10% for  $-10^\circ$  tilt angle and even 20% for  $+10^\circ$  tilt as the hub spacing is reduced. The beneficial effects arise from both tandem and side-by-side interactions, particularly evident for close rotor positioning (Fig. 5.26).

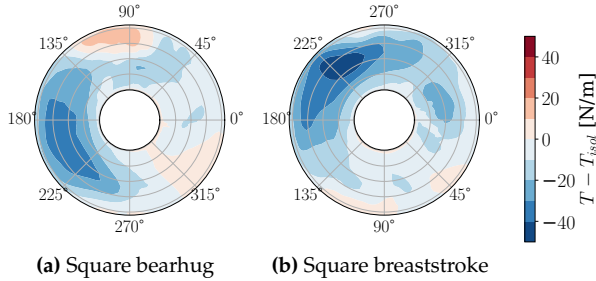


**Figure 5.25:** Change in thrust of rotor 2 in the square configuration with tilt  $+10^\circ$  and  $d/D=0.96$  (UPM)

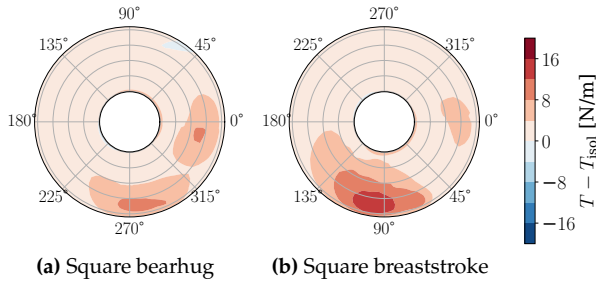


**Figure 5.26:** Change in thrust of rotor 1 in the square configuration with  $\alpha_R = -10^\circ$  and  $d/D = 0.96$  (UPM)

The discrepancies between the selected solvers were analysed in greater detail for the square breaststroke configuration at  $1.2D$  rotor spacing and  $-10^\circ$  tilt angle based on the induced velocity fields (Fig. 5.27). The blue and red colours represent the downwash and upwash regions respectively and the white areas in the measurement results are due to the shadows of the rotor hubs, for which no velocity data could be evaluated. All of the presented results show similar wake propagation, yet small differences, reflected in the performance estimate for this rotor spacing (Fig. 5.28), can be noticed. The higher velocities obtained by PUMA indicate a stronger breaststroke interaction between the front rotors, which results in a greater increase in their

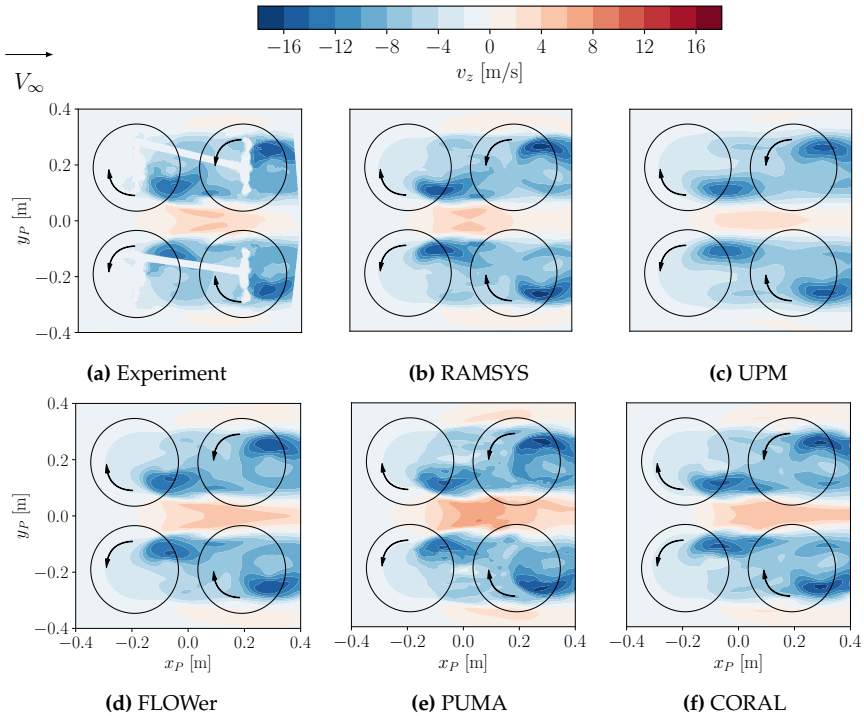


**Figure 5.27:** Induced velocity fields of the square breaststroke configuration,  $d/D = 1.2$ ,  $\alpha_R = -10^\circ$

efficiency on the advancing side, as shown in Fig. 5.29 for rotor 3. When it comes to prediction of the back rotors' performance, the RAMSYS results show the lowest thrust reduction (Fig. 5.28). Compared to UPM, the distribution of the downwash shed from the retreating side of the front rotors in the velocity field from RAMSYS indicates a slightly weaker interaction with the back rotors. As a result, the estimate of the thrust loss on rotors 2 and 4 due to the tandem interaction differs between these tools, which can be seen around  $160^\circ$  azimuth in Fig. 5.29.

The differences in the predicted wake geometry and propagation do not significantly affect the results at negative tilt angles; however, they lead to greater discrepancies for the nose-up tilt, where vortices move closer to the rotor planes. This is particularly evident for the torque values where the maximum difference reaches 30% (Fig. 5.22). As shown in the tandem results, the wake interactions with the back rotors are the greatest for the tilt angle of  $+10^\circ$ , making it the most difficult



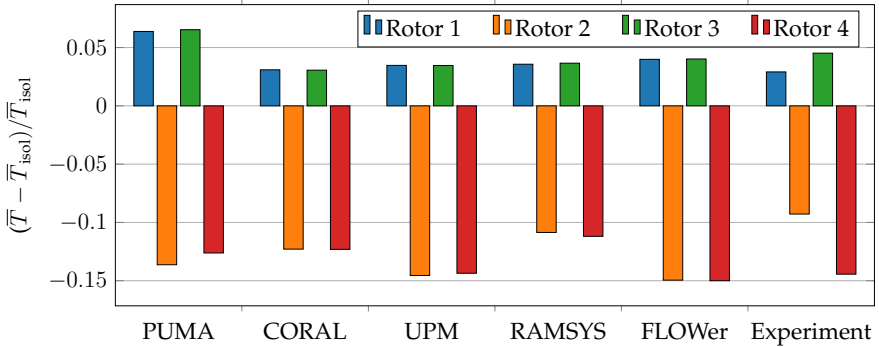


**Figure 5.28:** Change in mean thrust of each rotor in the square breaststroke configuration for  $d/D=1.2$  and  $\alpha_R = -10^\circ$

test case to model. A discussion of the discrepancy in torque prediction can be found in Section 5.4.2. At  $+10^\circ$  the interactions affecting the back rotors are strong regardless of the hub spacing, yet for rotors 1 and 3 they increase significantly for the most compact configurations and so does the discrepancy in the predicted torque values.

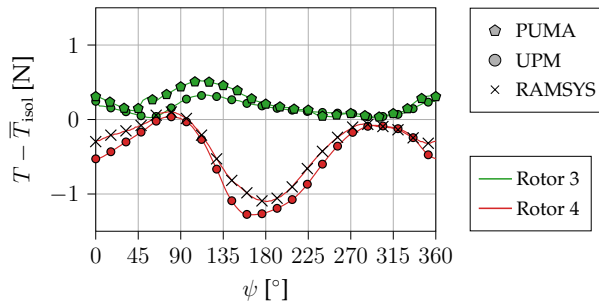


**Figure 5.29:** Relative change in azimuthal blade loading for rotor 3 and 4 in the square breaststroke configuration,  $d/D=1.2$ ,  $\alpha_R=-10^\circ$

### 5.3.2 Diamond configuration

In the diamond configuration, substantial interactions arise from the diagonal bearhug (rotors 1 and 3) and diagonal breaststroke alignment (rotors 1 and 2). Similar to the two-rotor systems, the performance of rotors 2 and 3 improves due to the influence of the tip vortices of rotor 1 from its retreating and advancing side, respectively (Fig. 5.30). The beneficial effects can already be observed for larger rotor spacings,

although it should be noted that in the diamond configuration the distance between side rotors and rotor 1 in the flight direction is shorter than the defined hub distance and is equal to  $d/\sqrt{2}$ . Additionally, for rotor spacings closer than  $1.44D$  the side rotors operate partially behind rotor 1 relative to the flow. As a result, for the closest analysed hub spacing rotors 2 and 3 operate in conditions comparable to the tandem system and the interaction effects become detrimental to their efficiency.

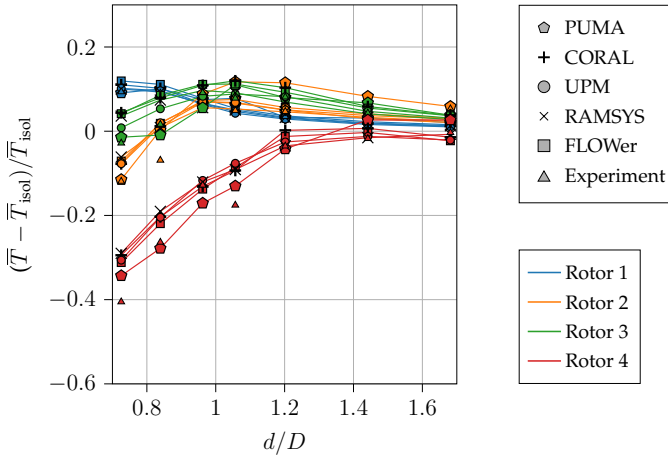


**Figure 5.30:** Change in mean thrust of each rotor in the diamond configuration with varying rotor spacing for tilt angle  $-10^\circ$

Rotor 4 is located  $\sqrt{2}$  times further from rotor 1 than the distance between the front and back rotors in the square configuration. As a result, the influence of the side rotors on rotor 4 is greater than the effects of its tandem interaction with rotor 1. The induced velocity fields for  $-10^\circ$  tilt and  $d/D = 1.2$  shown in Fig. 5.31 indicate that strong diagonal breaststroke interactions alter the wake propagation of the advancing side vortex of rotor 2. Consequently, in contrast to a beneficial diagonal breaststroke interaction between rotors 2 and 1, rotor 4 is affected by the downwash from rotor 2. However, this effect is balanced by the influence of the upwash from the retreating side of rotor 3 up to the rotor spacing  $1.2D$  (Fig. 5.32a). For smaller spacings, the influence of both side rotors on rotor 4 becomes detrimental (Fig. 5.32b) and its efficiency starts to decrease (Fig. 5.30).

In the diamond configuration, differences in the simulated propagation of tip vortices, especially the strong rolled-up vortices from the advancing side, lead to discrepancies in the assessment of interaction effects. The simulated induced velocity

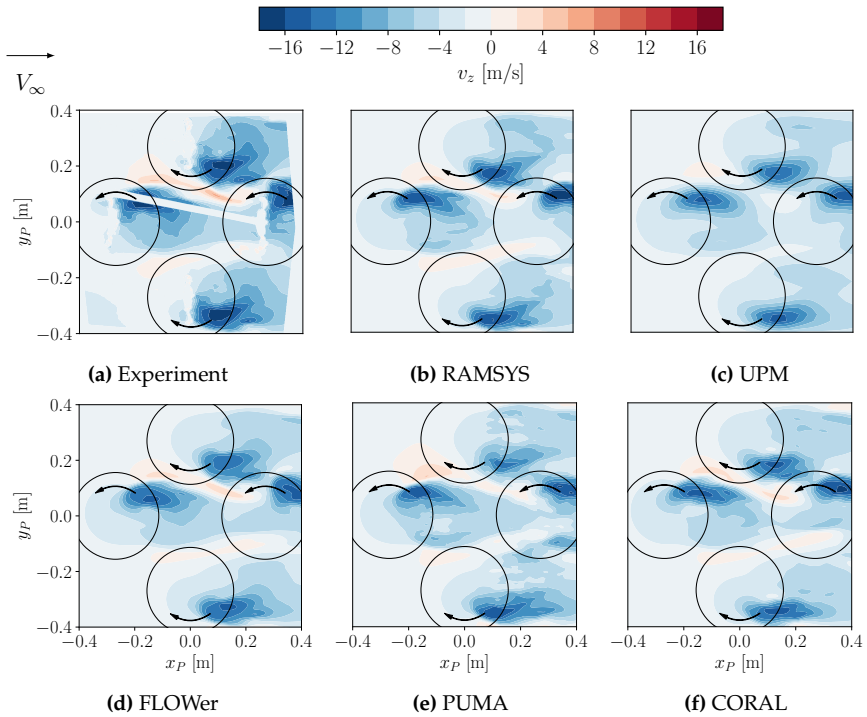


**Figure 5.31:** Induced velocity fields of the diamond configuration,  $d/D = 1.2$ ,  $\alpha_R = -10^\circ$

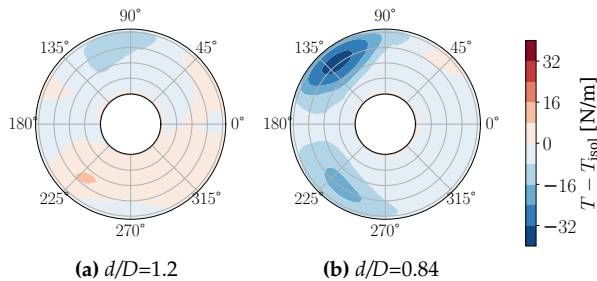


**Figure 5.32:** Change in thrust of rotor 4 in the diamond configuration with tilt  $-10^\circ$  (UPM)

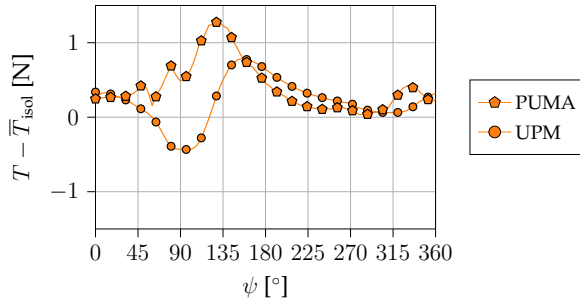


**Figure 5.33:** Relative change in azimuthal blade loading for rotor 2 in the diamond configuration,  $d/D = 1.2$ ,  $\alpha_R = -10^\circ$

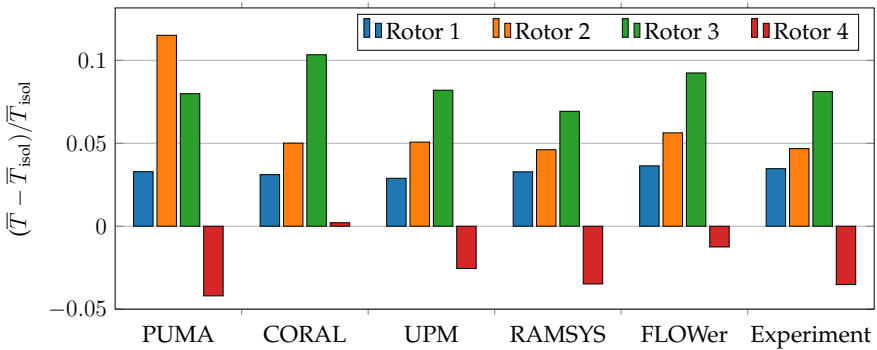


**Figure 5.34:** Change in mean thrust of each rotor in the diamond configuration for  $d/D=1.2$  and tilt angle  $-10^\circ$

fields for rotor spacing  $1.2D$  show that PUMA predicts a stronger and wider vortex shed from the advancing side of rotor 1 in compared to the UPM field (Fig. 5.31). As a result, rotor 2 operates in a strong upwash around  $130^\circ$  azimuth, whereas the same rotor in the UPM prediction is affected by an inboard downwash from the front rotor at  $90^\circ$  azimuth, before reaching an upwash region around  $150^\circ$  azimuth (Fig. 5.33). This causes a greater increase of thrust produced by rotor 2 in PUMA calculations, with the evaluated relative gain 5% higher than the UPM result (Fig. 5.34).

Similar to the square configurations, the increasing tilt angle leads to intensified wake-rotor interactions, especially on rotors 2 and 4, for which a wider spread of the calculated values is observed (Fig. 5.35b). The inviscid methods overestimate the thrust increase on rotor 2 compared to other tools and experimental results, which indicates that a strong upwash from rotor 1 causes a significant increase in angles of

attack on rotor 2, leading to local separation regions. Even though the relative change in thrust on the side rotors is similar to the negative tilt cases, a considerable decrease in their torque is observed for tilt  $+10^\circ$  with a minimum at a rotor spacing of  $1.2D$  (Fig. 5.35d). According to the experimental results, the maximum torque reduction reaches 10% for rotor 3 and almost 30% for rotor 2.

The negative interaction effects on rotor 4 are dominant at a tilt of  $+10^\circ$ , resulting in up to 50% thrust reduction and 20% torque increase at  $d/D=0.74$ . The efficiency of rotor 4 is therefore up to 20% lower than that estimated for the back rotors in the square system with overlapping rotors. On the other hand, the efficiency of rotor 1 increases by up to 20% with reduced rotor spacings due to diagonal bearhug and breaststroke interactions as well as tandem interactions for the closest positioning.

### 5.3.3 Influence of rotor phasing

The presented results were prepared with the assumption of orthogonal rotor phasing, necessary for the test cases with overlapping rotors. For selected non-overlapping rotor spacing  $d/D=1.2$ , measurements were performed for both orthogonal and tip-to-tip rotor phasing (Fig. 3.23). The comparison of the results obtained for the diamond configuration shows that the rotor phasing has a negligible influence on thrust and torque produced by the quadrotor for the whole range of tilt angles analysed (Fig. 5.36). Nevertheless, it can be a decisive factor in the aeroacoustic design.

The acoustic signature of the analysed configurations was evaluated based on the overall sound pressure level (OASPL) on a plane located 1.35 m below the centre of a quadrotor (Fig. 5.37), similar to the one used in the isolated rotor study. The analysis included cases with a tilt angle of  $-10^\circ$  for two selected rotor spacings  $0.96D$  and  $1.2D$ , alternating between orthogonal and tip-to-tip phasing for the latter (Fig. 3.23). For the  $0.96D$ , only orthogonal phasing was feasible without adding a vertical offset between the rotors due to the blade overlap. The results included loading and thickness noise contributions and were cross-validated using two computational tool chains UPM+APSIM and FLOWer+ACCO.

Calculated aeroacoustic carpets show that the noise directivity pattern differs between square bearhug and square breaststroke configurations operating with orthogonal phasing (Fig. 5.38). As the load fluctuations on the blades increase with reduced hub spacing, the increase in the noise levels below the quadrotor can be observed for the rotor spacing  $0.96D$  compared to  $1.2D$ . Nevertheless, the relative rotor phasing proves to be the decisive factor for the square configurations, as the rotors operating tip-to-tip produce about 6 dB more noise than those with orthogonal

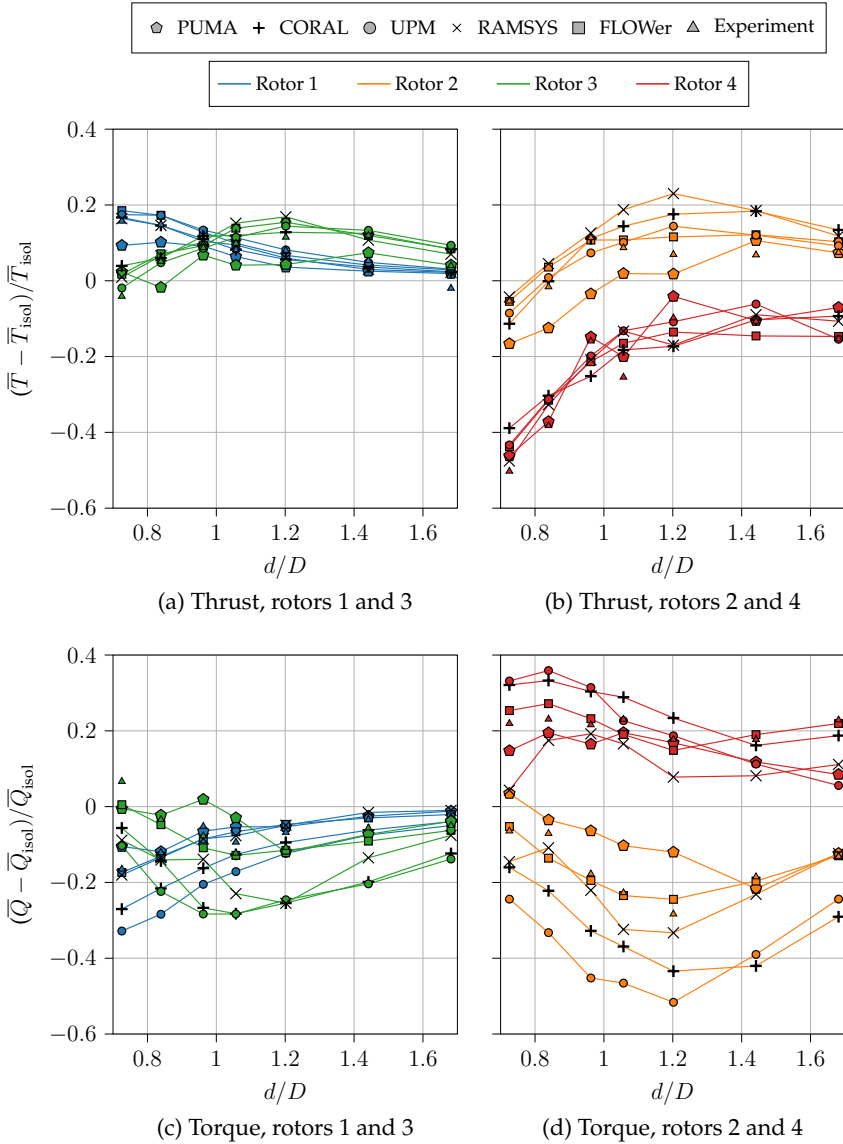


**Figure 5.35:** Change in mean thrust and torque of each rotor in the diamond configuration with varying rotor spacing for tilt angle  $+10^\circ$

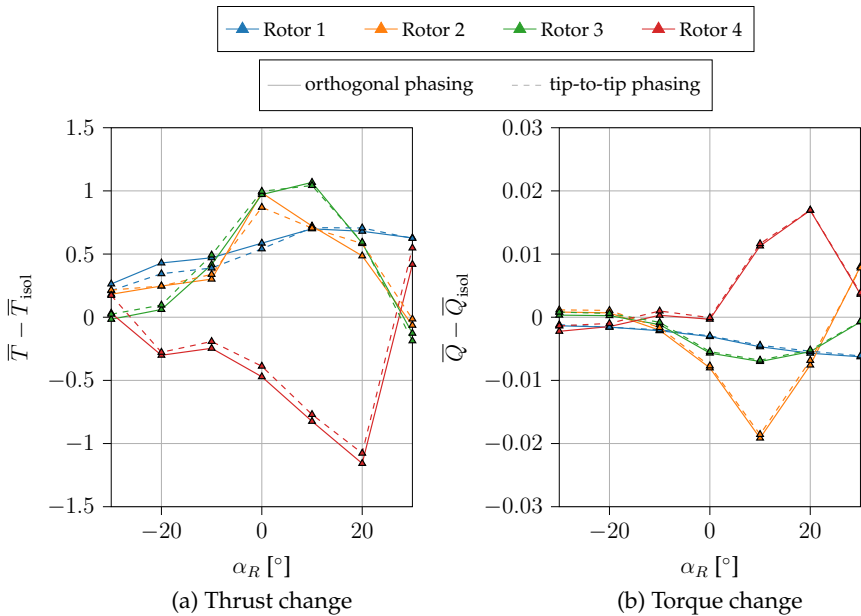


**Figure 5.36:** Absolute changes of rotor thrust and torque in the diamond configuration depending on the rotor phasing,  $d/D=1.2$

phasing at the same  $d$ . An unfavourable tendency is observed for the diamond configuration, which means that, for the cases analysed, the alignment of rotors in-phase with respect to the flow direction is more detrimental in terms of generated OASPL than close blade passages in tip-to-tip phasing (compare Fig. 3.23b and Fig. 3.23c). The results show that a diamond configuration with  $d/D = 0.96$  and orthogonal phasing is the least favourable of the analysed variants in terms of generated noise.

A comparison of the OASPL noise carpets for all configurations with tip-to-tip rotor phasing shows a very good agreement between applied computational methods (Fig. 5.39). Nevertheless, the OASPL levels are determined by the first few harmonics and do not give an overview of multirotor interactions, reflected in the increase of unsteady loading noise at higher frequencies. These are also particularly important as human hearing is the most sensitive to frequencies between 2000 and 5000 Hz, corresponding here to the range between 11 and 28 BPF harmonics. Harmonic spectra for the bearhug square and diamond configurations at an observer position directly below the multirotor are presented in Fig. 5.40. A comparison between the UPM+APSIM and FLOWer+ACCO results shows that the panel method is able to reproduce the

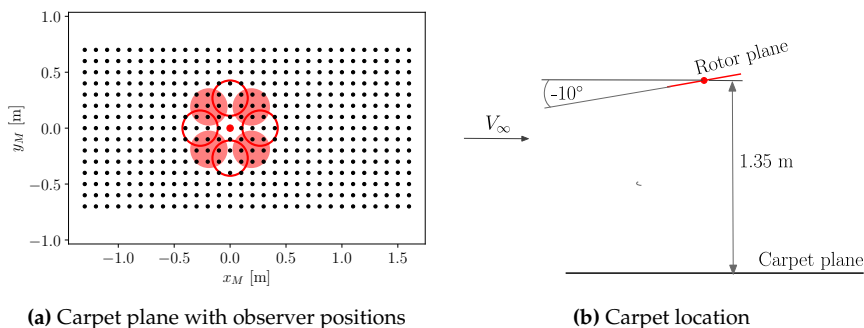


**Figure 5.37:** Analysed observer positions relative to the quadrotor centre

SPL levels of the higher-fidelity solver for the first 3-4 harmonics, resulting in a good agreement in the OASPL carpets from both methods. Nevertheless, UPM+APSIM tends to overestimate harmonic contributions at higher frequencies, as proved also in other studies [97]. Both observations are the effects of the applied roll-up model. The results can be partially adjusted by changing model parameters, such as the tip vortex core radius; however, the method still shows limitations in recreating higher harmonic contributions. Another factor leading to expected discrepancies in broadband noise prediction is the omission of viscosity in UPM. Nevertheless, qualitative trends from the comparison between different configurations were captured with both computational tools.

Tip-to-tip phasing results in the highest noise levels for the first 3 harmonics for the square bearhug configuration, which could be observed in OASPL carpets. Orthogonal phasing allows for significant reduction in the SPL caused by acoustic interference, yet it does not alleviate aerodynamic interactions between the rotors. As a result, noise levels at higher frequencies are insensitive to rotor phasing and remain nearly constant above 2.5 kHz due to the high unsteady loading. Consequently, despite orthogonal phasing the highest SPL in the mid-range is produced by the configuration with overlapping rotors ( $d/D = 0.96$ ) and thus, with intensified aerodynamic interactions.

For the diamond configuration, noise levels generated by the overlapping rotors dominate not only mid-frequencies but also the first harmonics. Tip-to-tip phasing at  $d/D = 1.2$  shows an advantage over orthogonal phasing at low frequencies, however, above 2000 Hz the noise produced by both variants is comparable. The UPM+APSIM prediction shows slower decay of harmonics with increasing frequency than FLOWer+ACCO, again due to excessive numerical noise.



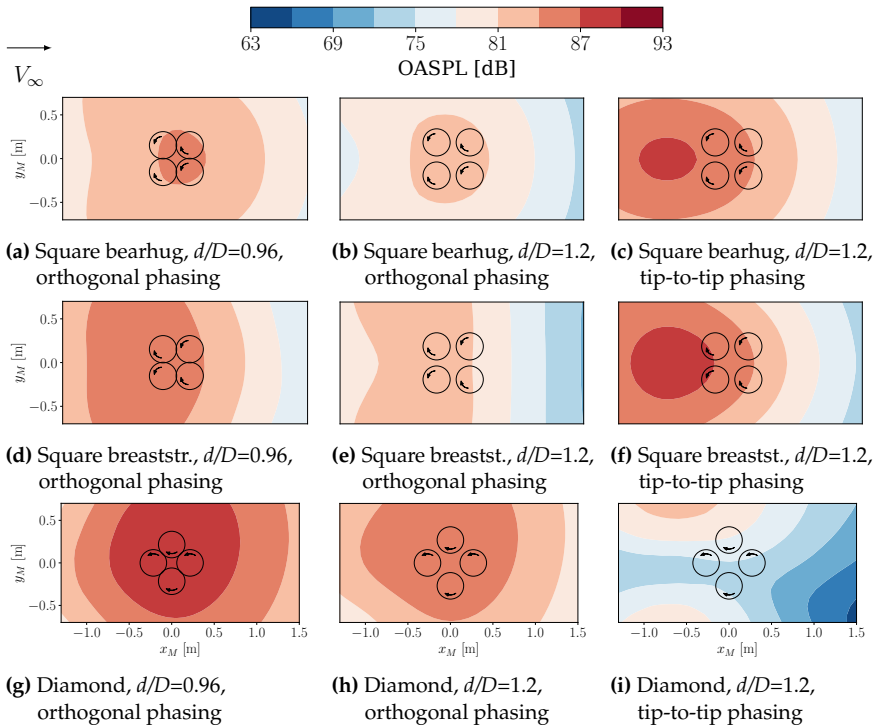


**Figure 5.38:** Calculated OASPL on a plane 1.35 m below the quadrotor with  $-10^\circ$  tilt, UPM+APSIM

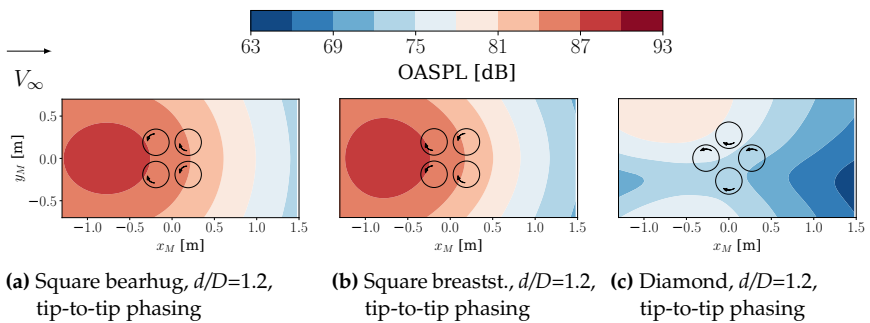


**Figure 5.39:** Calculated OASPL on a plane 1.35 m below the quadrotor with  $-10^\circ$  tilt, FLOWer+ACCO

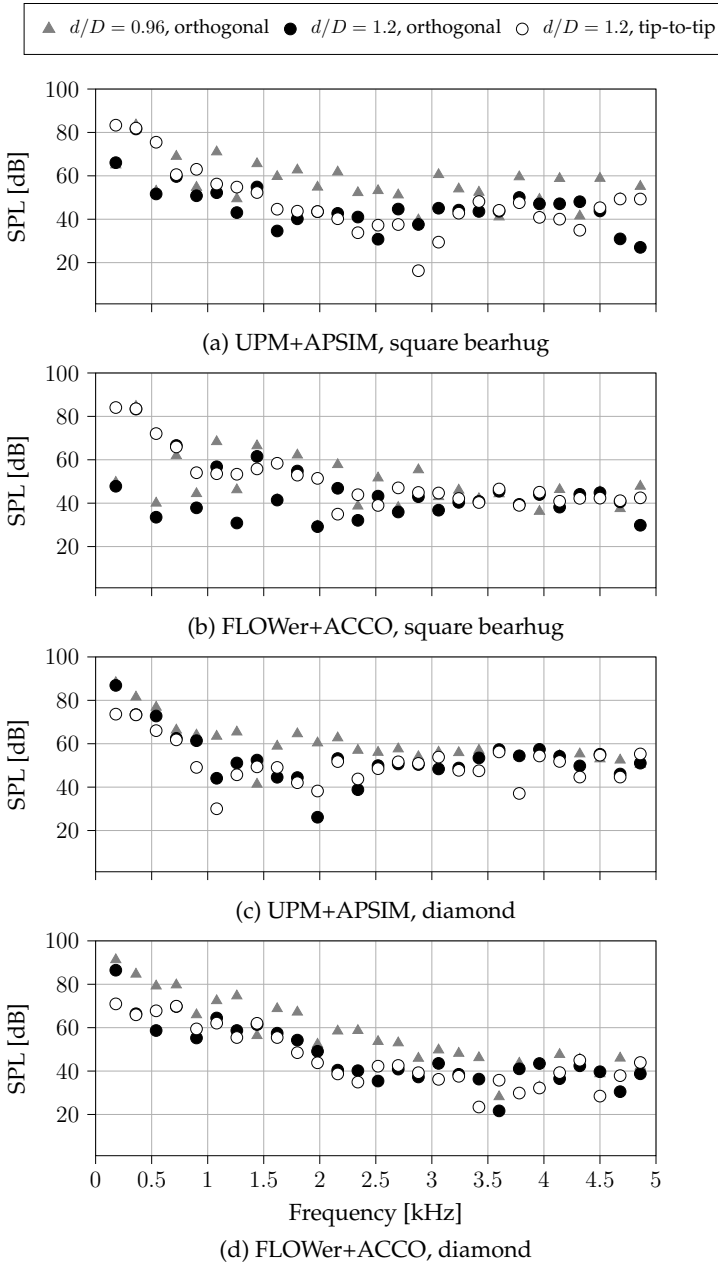


**Figure 5.40:** Harmonic spectra at the observer position [0,0,-1.35] depending on the rotor spacing and phasing

## 5.4 Discussion

### 5.4.1 Accuracy of the measurement

The accuracy of the thrust measurement can be estimated from the balance calibration on different days. Assuming that the variation in the thrust measurement is only proportional to changes in the air density, the calculated uncertainty is 3.8% for rotor 1, 1.4% for rotor 2, 1.5% for rotor 3 and 1.9% for rotor 4. Possible errors due to the balance drift in the measured absolute thrust differences were minimised by repeating the single rotor measurements directly prior to the multirotor test cases.

The standard deviation of the thrust from the isolated rotor measurements on different days equals 0.2 N for the  $-10^\circ$  tilt and 0.3 N for  $+10^\circ$ , which is around 3% of the average value for both cases. The deviation for the torque values calculated from the electrical power consumption equals 0.001 Nm, which is less than 2% for both tilt angles.

Another uncertainty of the results can be evaluated based on the symmetry accuracy. By definition, the square configuration is symmetrical, which means that both front and both back rotors should produce the same forces. Deviations from this rule seen in the results occur due to the uncertainty of the scales, geometry imperfections and asymmetry in the flow. Based on the average of the measurements from different days, the difference in the thrust measurement of the front rotors (1 and 3) is 0.25 N regardless of the tilt angle, while for the back rotors (2 and 4) the difference is 0.16 N for  $-10^\circ$  tilt and it increases to 0.3 N for  $+10^\circ$  tilt. The measured torque differed by 0.001 Nm between the front rotors and by 0.006 Nm between the back rotors.

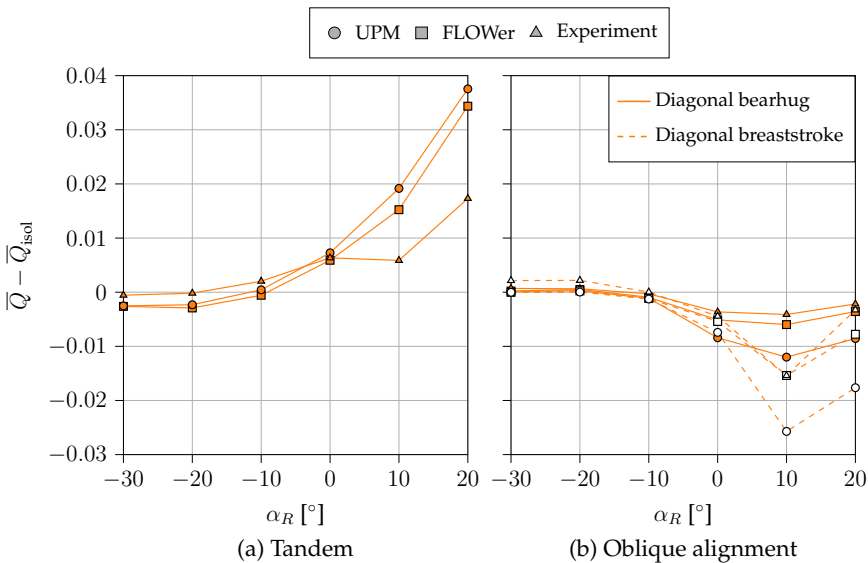
### 5.4.2 Discrepancies in torque prediction

Significant interactions occurring at the  $10^\circ$  tilt angle make it a challenging test point for both computational analysis and measurement. As the vortices pass close to the blades, modelling choices, such as vortex core models in the free wake methods, have an increased impact on the results. Differences in the estimated blade loading (bound circulation) result in a different circulation transferred to the wake panels through the Kutta condition. These two factors together cause discrepancies in the wake propagation which affect the aerodynamic interactions between the rotors, particularly at nose-up tilt angles. The effect is especially visible on the torque values, sensitive to the exact inflow conditions. Nevertheless, the spread in the estimated torque changes due to the interactions to a large extent reflects the spread in the

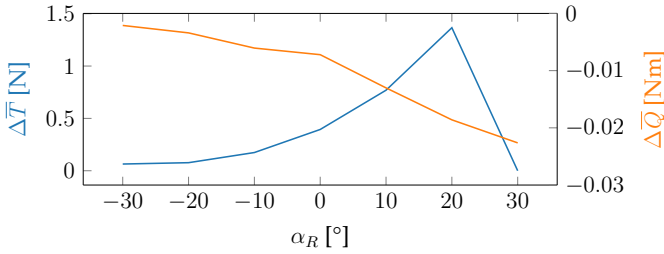
absolute torque values from the isolated rotor study used as a reference.

Figure 5.41 presents the change in torque of rotor 2 from Fig. 5.12b and Fig. 5.14d as the absolute difference from the isolated rotor results. Figure 5.41a shows that potential methods such as UPM are capable of capturing the torque changes due to interactions comparable to the high-fidelity results of FLOWer. Nevertheless, as these tools do not account for the viscous drag and therefore underestimate the absolute torque values, the resulting relative torque changes can be greatly overestimated. This is particularly evident for tandem interactions (and therefore also for square configurations) at high nose-up tilt angles, where the torque on the back rotors increases sharply as the reference torque of a single rotor decreases.

Additionally, as presented in Fig. 5.41a, while the UPM and FLOWer results show a comparable tendency over the whole range of tilt angles, the experimental data indicate a change in the trend at  $10^\circ$ . The discrepancy originates from a decreased accuracy of the measurement at this point due to installation effects. While the front rotors in the square configurations operated in unobstructed flow conditions for all test cases, the inflow of the back rotors was partially blocked by the rotor struts at positive tilt angles. The effect can be observed in the difference in the measured isolated rotor performance between front and back positions, shown in Fig. 5.42. The



**Figure 5.41:** Absolute torque change of rotor 2 for  $d/D=1.2$



**Figure 5.42:** Difference between isolated rotor loads measured at front and back position of the square frame

trend of  $\Delta \bar{T}$  indicates an increasing inflow blockage until the 20° tilt angle. In contrast to the measured thrust, the full recovery at  $\alpha_R = 30^\circ$  could not be observed for the torque. To account for the blockage effect the quadrotor results were presented as a difference from the isolated rotor performance, measured for each rotor and each position separately. While the method was effective for interpreting interaction effects on thrust in all cases, the choice of a correct reference for the torque of the back rotors is not straightforward as shown in (Fig. 5.43). The discrepancy between the selected approach and FLOWer results is the greatest for the tilt angle 10°, and the agreement improves again for higher positive angles as the back rotors are no longer directly in the wake of the upstream rotors. As a result, also for the square configurations, most of the tools, including high-fidelity solver FLOWer, overestimate the torque increase on the back rotors at 10° compared to the measurement (Fig. 5.22).

In contrast to the tandem cases, the predicted torque trends from the potential tool UPM and the high-fidelity code FLOWer do not agree at the nose-up rotor tilt for oblique alignment interactions (Fig. 5.41b), indicating the influence of viscous effects. In these cases, unlike in the tandem configuration, the angles of attack on rotor 2 are locally increased by the upwash from the wake of the front rotor. At higher nose-up tilt angles this leads to flow separation and hence an increase in viscous drag, which cannot be predicted by potential methods. The resulting discrepancy between UPM results and FLOWer/ experiment is more significant for a diagonal breaststroke interaction, as it affects the advancing side of rotor 2, which generates most of the rotor loads. Similarly, potential methods (UPM, RAMSYS, CORAL) tend to overestimate the torque reduction for side rotors 2 and 3 in the diamond configuration, as shown for the 10° tilt angle (Fig. 5.35c,d). A similar observation applies to side-by-side interactions at high positive tilt angles.

Calculations performed with the potential solver PUMA considered the viscous

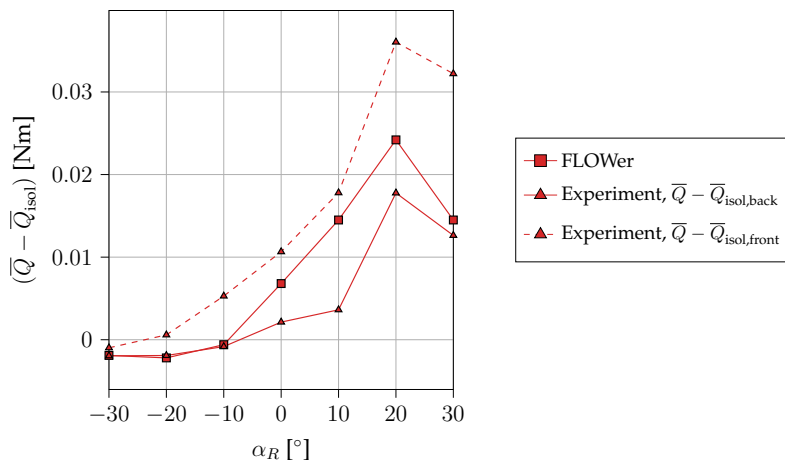


**Figure 5.43:** Change of torque of rotor 4 in the square bearhug configuration for  $d/D=1.2$  depending on the isolated rotor reference

effects through the airfoil characteristics. This approach did not always improve the performance prediction due to uncertainty in the airfoil data at low Reynolds numbers or reduced accuracy of the polars for higher angles of attack. Therefore, taking the diamond configuration as an example, the PUMA results indicate stronger upwash on rotor 2 leading to an overpredicted stall on its blades (Fig. 5.35d).

Discrepancies between UPM and RAMSYS results for the square configurations at the  $10^\circ$  tilt angle prove that for high-interaction cases, differences in the wake propagation between the solvers can have a greater impact than viscous vs. potential flow assumptions or different blade representations (Fig. 5.22).

## 5.5 Quadrotor configurations with vertical spacing

The study of square configurations shows that the interaction with the wakes of the front rotors has a detrimental influence on the back rotors' efficiency, reducing the performance of a quadrotor for all horizontal rotor spacings analysed. As further increases in hub spacing require a corresponding increase in vehicle dimensions, the introduction of a vertical offset of the back rotors can be a more practical method of improving efficiency. In contrast, a diamond configuration showed enhanced performance for most of the conditions analysed, with the back rotor being the only one affected by negative interaction effects. The following study verifies that adding

a vertical offset  $z$  to the back rotors in the square bearhug configuration or to the rearmost rotor in a diamond configuration (Fig. 5.44) can effectively improve, or respectively further improve, the quadrotor performance.

The total thrust and torque of a quadrotor were compared with those of four isolated rotors for different vertical spacings up to  $z/D = 0.38$  (Fig. 5.45, 5.46). Figure 5.45a,b shows that for a tilt angle of  $-10^\circ$ , raising the back rotors in the square configuration immediately increases the quadrotor efficiency. For both hub spacings, a gradual increase in thrust was obtained with increasing vertical offset with no more than a 1% change in torque (Fig. 5.46a,b). At a hub spacing of  $d/D = 0.96$  a vertical offset of  $0.15D$  is sufficient to eliminate the detrimental downwash effects. Further increases in the vertical spacing give a slight improvement of system efficiency (less than 5%) compared to four isolated rotors. Nevertheless, the trend indicates that adding an offset greater than  $0.38D$  would not result in a significant further increase in the thrust produced. The same applies to the hub spacing  $d/D = 1.2$ , for which no thrust gain over four isolated rotors could be achieved. In contrast to the immediate benefits at the  $-10^\circ$  tilt angle, the increase in efficiency for the smallest vertical spacing at the positive angle of  $10^\circ$  is negligible, with a slight increase in both thrust and torque. In the case of  $d/D = 1.2$ , no more than 2% efficiency improvement was achieved below  $z/D = 0.26$ .

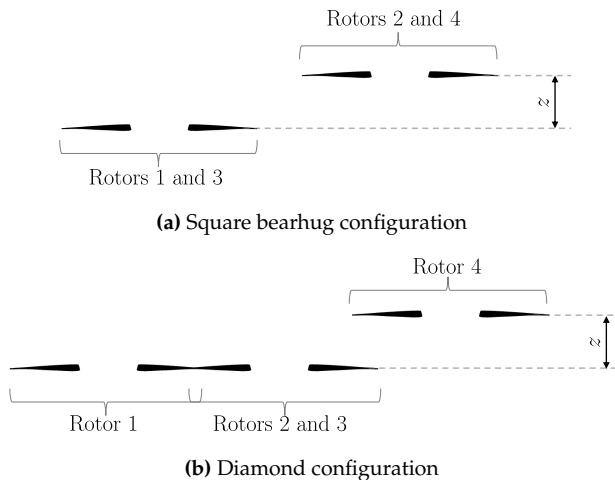


**Figure 5.44:** Definition of the vertical spacing  $z$  between the rotors for  $d/D=1.2$

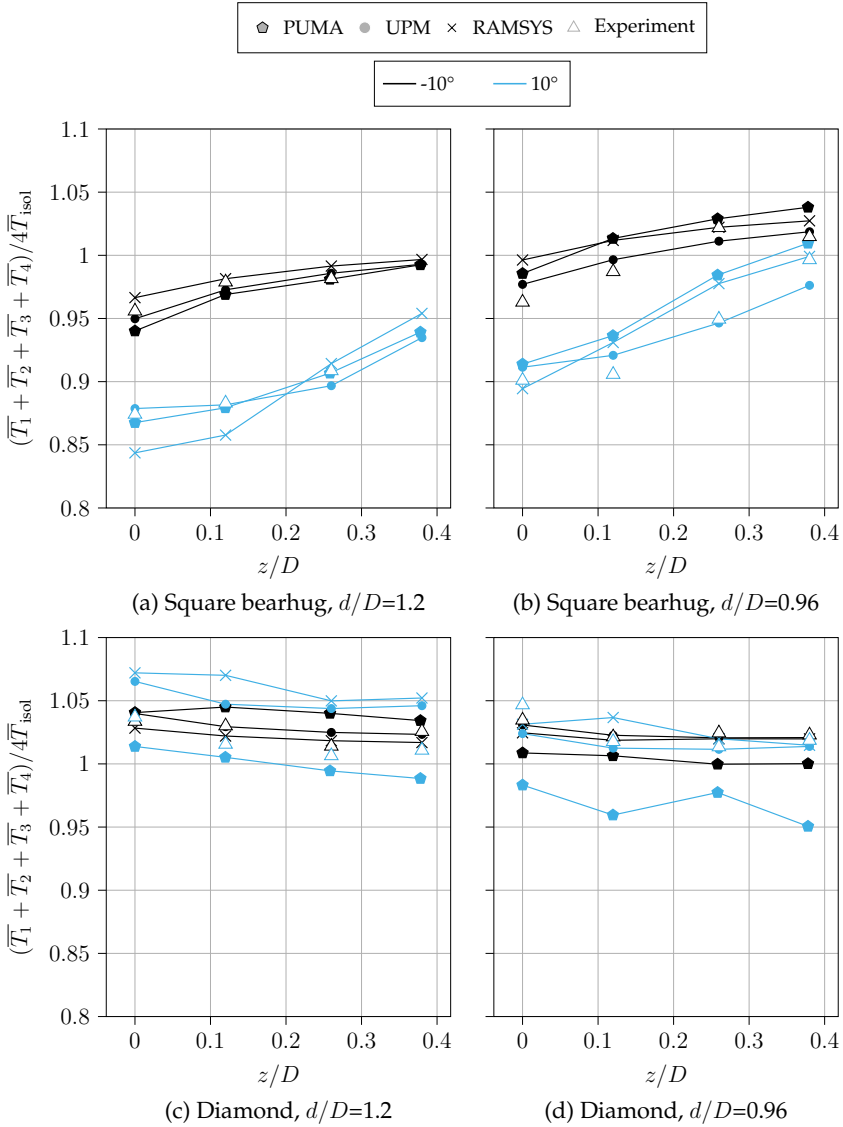
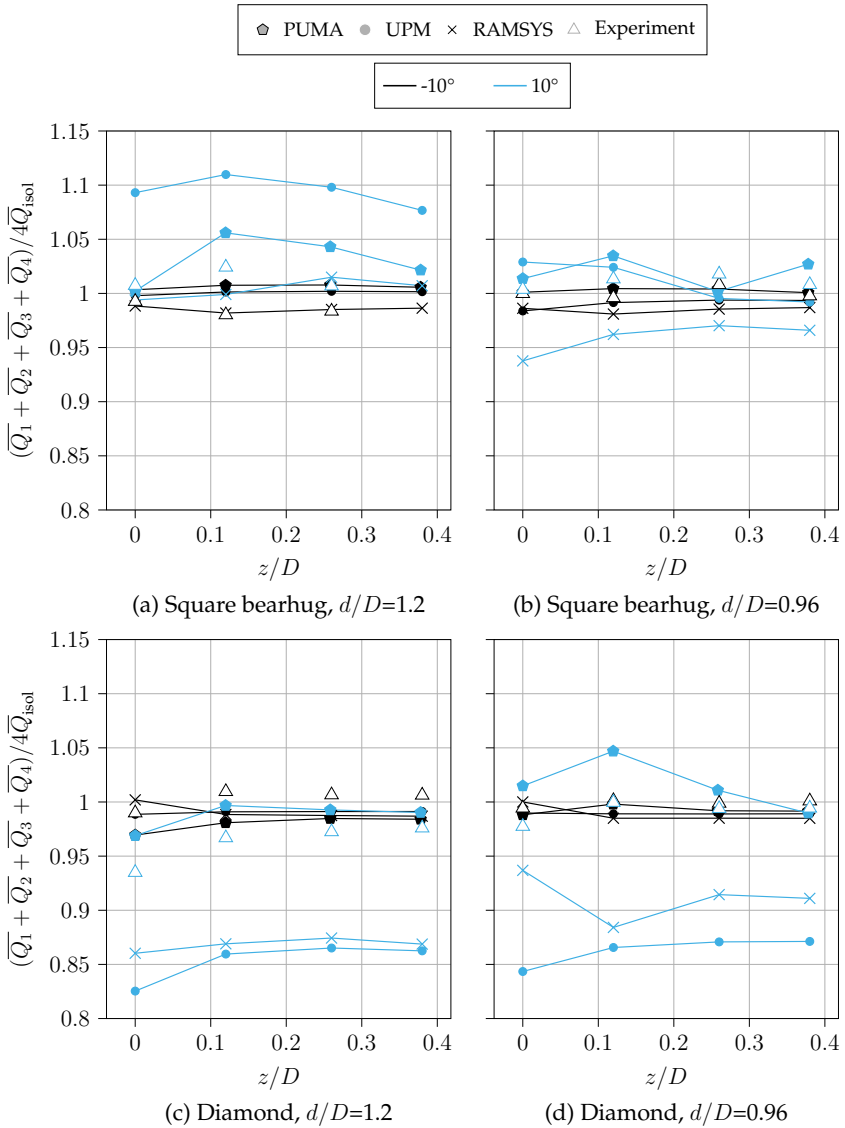


Figure 5.45: Change in mean thrust of the quadrotor with varying vertical rotor offset





**Figure 5.46:** Change in mean torque of the quadrotor with varying vertical rotor offset

A higher vertical offset results in a gradual torque reduction (Fig. 5.46a) and a significant gain in produced thrust. For both vertical spacings, up to 10% performance improvement was achieved by raising the back rotors by  $0.38D$ . As a result, a configuration with horizontal spacing  $d/D = 0.96$  reached the efficiency of four isolated rotors, while the maximum efficiency for the  $d/D = 1.2$  case was 5% lower.

Conversely, raising the back rotor in the diamond configuration leads to a performance decrease and thus to the loss of the benefit from the interactions between the front rotors visible at  $z = 0$ . Already at  $z/D = 0.12$  a simultaneous decrease in produced thrust and increase in torque could be observed, resulting in an efficiency reduction of up to 4% at  $d/D = 1.2$ . However, the quadrotor performance remains nearly constant with a further increase in the vertical spacing.

The described tendencies were reproduced by all computational methods. Deviations from the general trends of up to 5% can be observed for the diamond configuration with  $d/D = 0.96$  due to strong interactions between the rotors and resulting stability issues. Discrepancies in the torque prediction up to 15% are consistent with those described for the horizontal spacing analysis.

The effects of vertical spacing are studied in detail in the following sections based on the performance analysis of individual rotors.

### 5.5.1 Square bearhug configuration

Figure 5.47 shows the change in thrust compared to an isolated rotor for rotors 3 and 4, representing both the front and both the back rotors respectively. Adding a vertical offset to the back rotors improved their performance in all cases analysed. The thrust produced by each back rotor was increased by approximately 10% at  $-10^\circ$  tilt angle and 20% at  $10^\circ$  tilt, which in most cases was not sufficient to reach the isolated rotor's efficiency. Nevertheless, even though full recovery was not achieved for rotors 2 and 4, the efficiency increase of the front rotors counteracted the negative effect for the overall quadrotor performance. As shown in Fig. 5.48, a positive impact of the tandem interaction on the front rotor, visible around  $0^\circ$  azimuth, weakens as the vertical spacing between the front and back rotors increases. At the same time, a strong side-by-side interaction with a neighbouring rotor at  $270^\circ$  azimuth remains nearly unchanged, resulting in an approximately constant 10% thrust increase for rotors 1 and 3 at  $z/D = 0.96$ . The interaction effects between the front rotors at the wider hub spacing  $d/D = 1.2$  are not as strong, yet the benefit is clearly observable for all  $z/D$  values.

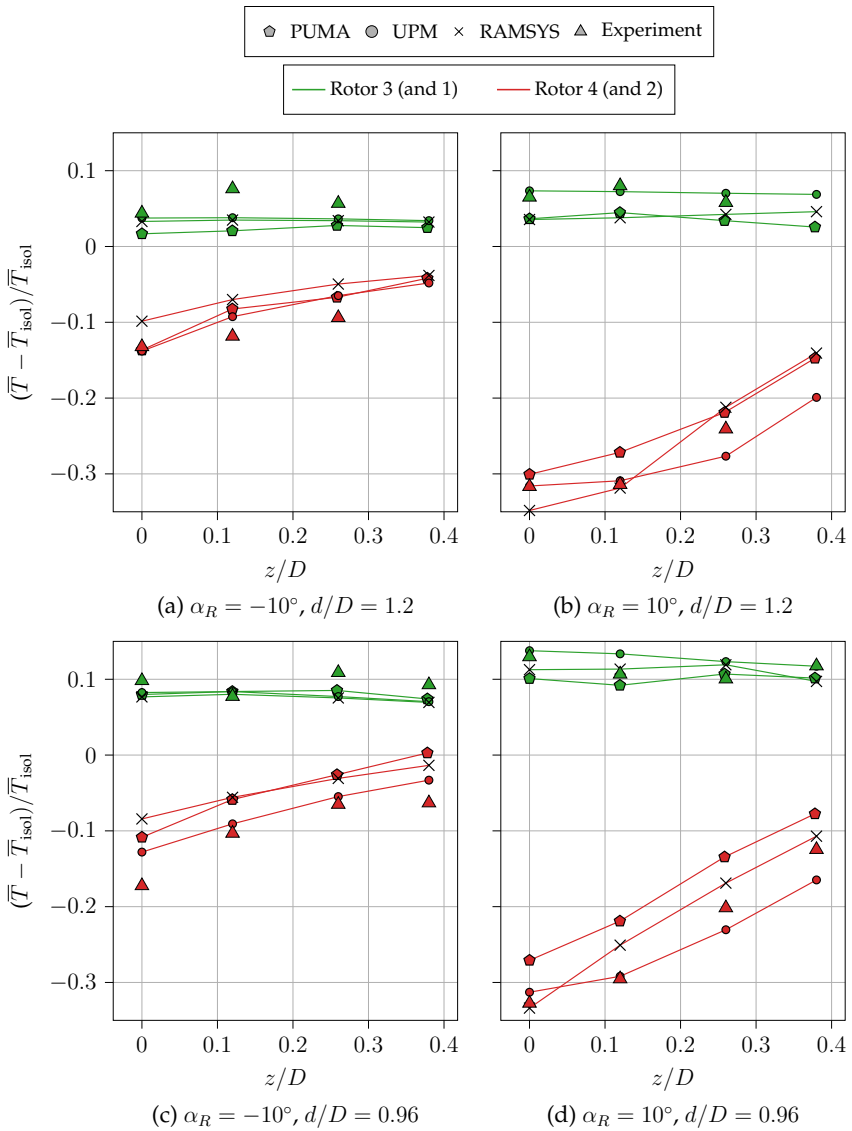


**Figure 5.47:** Change in mean thrust of each rotor in square bearhug configuration with varying vertical rotor offset

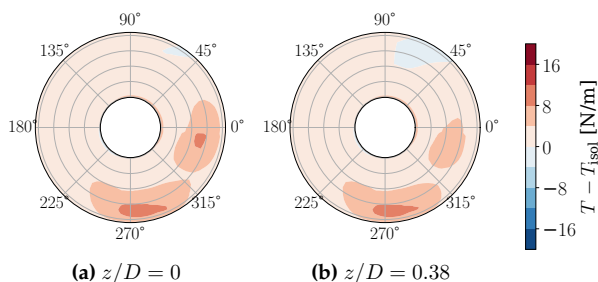


**Figure 5.48:** Change in thrust of rotor 1 in the square bearhug configuration with tilt  $-10^\circ$  and  $d/D = 0.96$  (UPM)

At  $z = 0$  the thrust loss on the back rotors is comparable for both horizontal spacings. However, at the  $10^\circ$  tilt angle increasing the vertical distance is less effective at the wider horizontal spacing than for the configuration with the blade overlap ( $d/D = 0.96$ ). Figure 5.49 shows that without the offset the back rotors in both cases are affected by the downwash from the advancing side vortex of the preceding rotor. Raising the back rotors reduces the interaction on this side; however, the rotors are then more affected by the retreating side vortex propagating at a higher level. This interaction persists at larger vertical spacings for  $d/D = 1.2$ , for which the trajectory of the vortices is more aligned with the back rotors.

Regardless of the horizontal separation at  $10^\circ$  tilt angle, the impact of the retreating side tip vortices on the back rotors is observable even for the largest vertical offset. The effect is surprising when looking at the wake trajectory of an isolated rotor. Figure 5.50a shows a theoretical position of a rotor placed at  $d/D = 0.96$  and  $z/D = 0.38$  at the  $10^\circ$  tilt angle. In this case, the retreating side tip vortex of the upstream rotor propagates in the rotor plane, well below the downstream rotor. However, as shown in Fig. 5.50b, a bearhug interaction between the front rotors changes the trajectory of their inboard tip vortices, directing them upwards. In a full configuration an upwash region is also generated between the back rotors, which further deflects the vortex trajectory towards the back rotor. As a result, detrimental downwash effects remain in this region for vertical offsets larger than expected.

The reduced impact of the front rotors' downwash is also reflected in the torque decrease for the back rotors (Fig. 5.51). Similarly, the recovery first appears for larger vertical offsets, above the trajectories of both advancing and retreating side vortices of the preceding rotors. For the offset  $z = 0.12$  and the wider spacing rotors 2 and 4 produce slightly higher torque before positive effects can be observed. As described in the Section 5.4.2, the experimental torque results is underestimated for the back

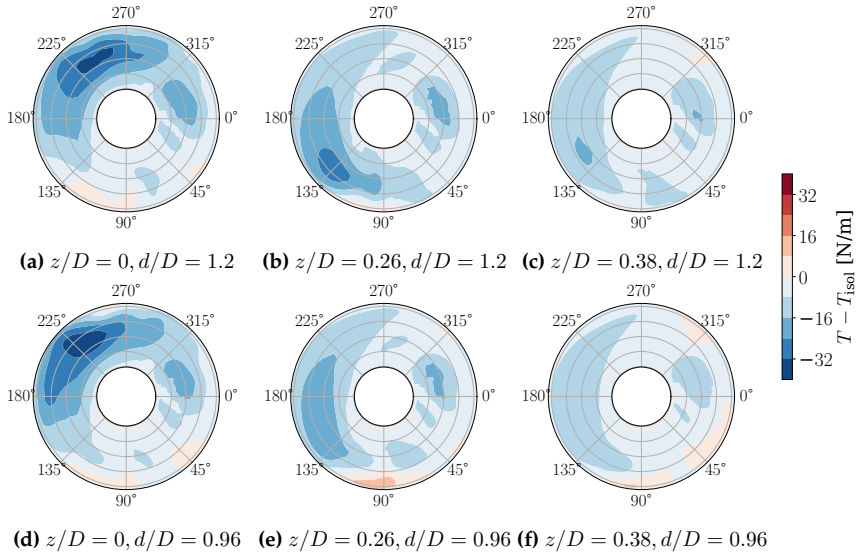


**Figure 5.49:** Change in thrust of rotor 2 in the square bearhug configuration with tilt  $10^\circ$  (UPM)

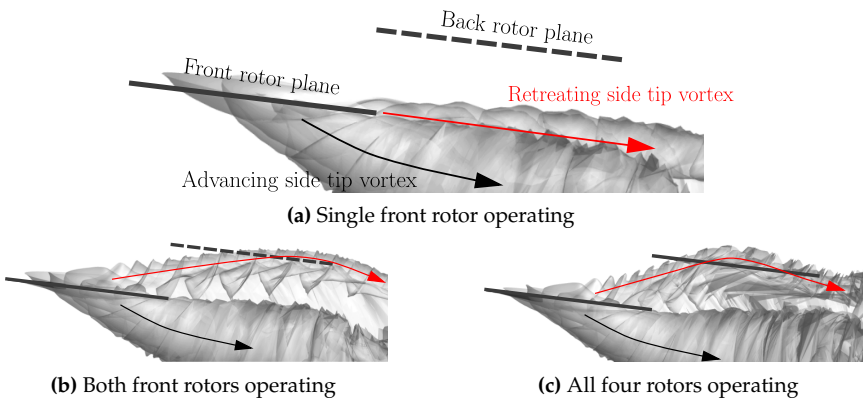


**Figure 5.50:** Wake of the front rotor(s) in square bearhug configuration at  $10^\circ$  tilt angle,  $d/D = 0.96$  and  $z/D = 0.38$

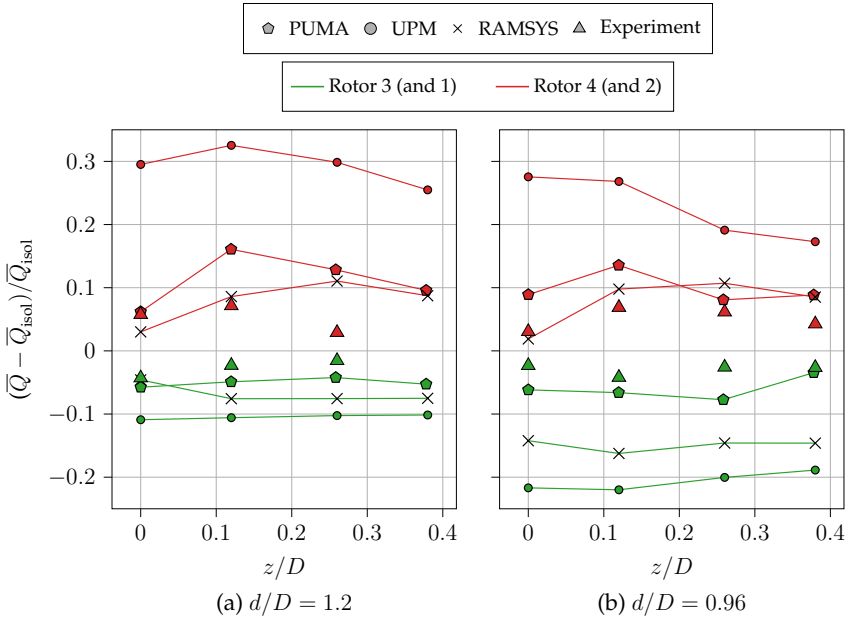


**Figure 5.51:** Change in mean torque of each rotor in square bearhug configuration with varying vertical rotor offset at  $\alpha_R = 10^\circ$

rotors due to installation effects at this tilt angle. For the front rotors an increase in torque of up to 2% was observed from reduced tandem interaction. At a tilt angle of  $-10^\circ$  the change in torque was negligible for all rotors.

The analysis shows that raising the back rotors is a more efficient method of improving the square quadrotor performance than increasing the horizontal hub spacing. This is particularly evident for the  $10^\circ$  tilt angle, where increasing the hub separation did not improve the back rotors' efficiency and only cancelled a positive proximity effect for the front rotors within the analysed  $d$  values. Nevertheless, the benefit of introducing a vertical offset strongly depends on the quadrotor tilt angle and effectively means that the strongest interactions with a preceding rotor wake are shifted to higher nose-up tilt angles. Figure 5.52 shows that at  $z = 0$  the back rotor recovers from the downwash influence above  $\alpha_R = 10^\circ$ . From this point on, adding a vertical offset has a detrimental effect as it causes a further drop in performance. Moreover, the resulting loss on the raised rotors at  $\alpha_R = 20^\circ$  is greater than the maximum loss with  $z = 0$  at  $\alpha_R = 10^\circ$ .

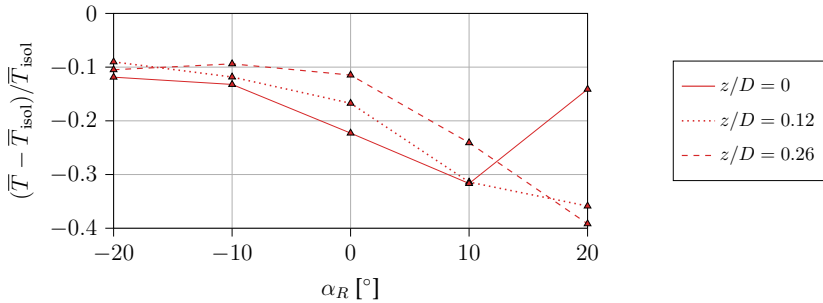


**Figure 5.52:** Change of thrust of rotor 4 depending on tilt angle and vertical offset, square bearhug configuration with  $d/D=1.2$

## 5.5.2 Diamond configuration

Raising the back rotor in the diamond configuration does not have a significant influence on the performance of the preceding rotors. For this reason, Fig. 5.53, 5.54, which show changes in thrust and torque due to interactions, focus on the results for rotor 4 with experimental data for rotors 1, 2 and 3 added as a reference.

At  $d/D = 1.2$ , adding the vertical offset to the back rotor causes a decrease in its efficiency, especially at a tilt angle of  $10^\circ$  with the simultaneous thrust reduction and torque increase of 10%. This effect is already observed for  $z/D = 0.12$  and it remains almost constant with further increasing  $z$  spacing. For  $d/D = 0.96$  the back rotor shows the lowest performance at  $z/D = 0.12$ . Its efficiency increases with greater vertical offsets, yet no improvement compared to the performance at  $z/D = 0$  was achieved. The explanation for the observed tendency can be found in the changes of sectional thrust compared to an isolated rotor (Fig. 5.55).

Unlike the square configuration, the back rotor in the diamond system is affected not only by the detrimental tandem interaction with the front rotor but also by diagonal alignment interactions with the side rotors. However, these can have either positive or negative effects depending on the flight conditions and distances between the rotors. For a larger horizontal spacing  $d/D = 1.2$  at the tilt angle of  $-10^\circ$ , the vortex from the advancing side of rotor 2 causes a local thrust reduction on rotor 4 (Fig. 5.55a). This detrimental effect is almost entirely cancelled by the upwash created by the retreating side vortex of rotor 3. Adding a vertical offset to the back rotor gradually reduces the downwash effect on the advancing side, but also completely eliminates the positive upwash influence (Fig. 5.55b,c). As the detrimental effect of the advancing side vortex remains observable for all vertical spacings, the rotor

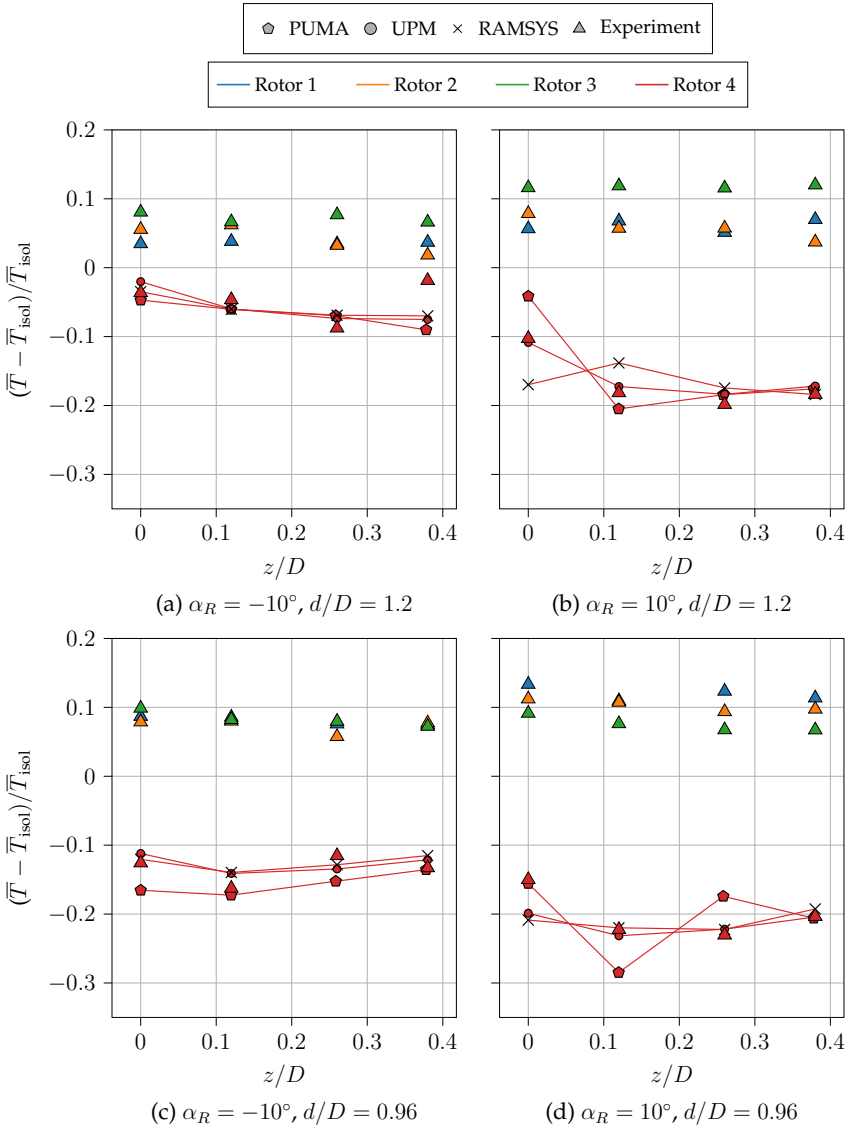


**Figure 5.53:** Change in mean thrust of each rotor in square diamond configuration with varying vertical rotor offset



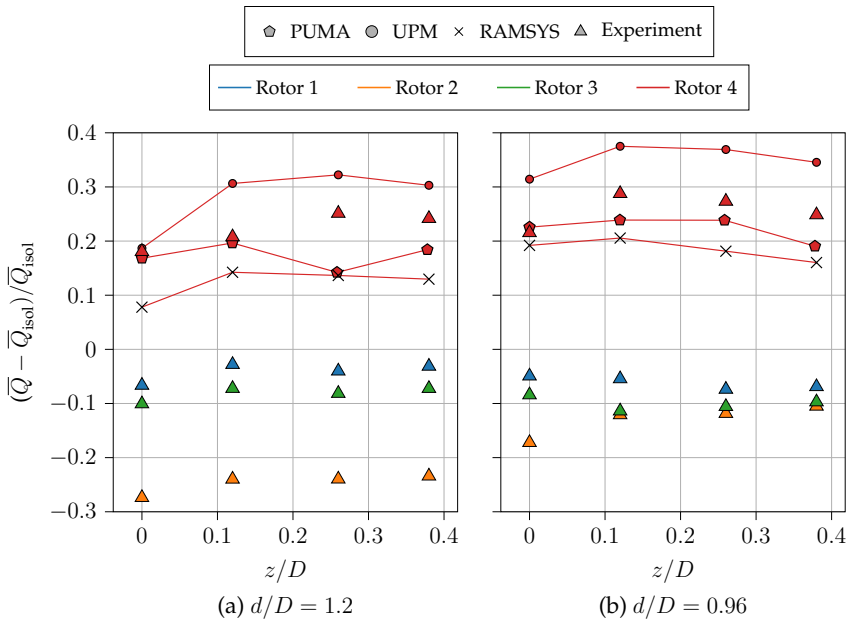


**Figure 5.54:** Change in mean torque of rotor 4 in diamond configuration with varying vertical rotor offset at  $\alpha_R = 10^\circ$

performance is reduced compared to the  $z = 0$  case. Additionally, a progressive thrust decrease at the front of rotor 4 indicates more interaction with the wake of rotor 1 for larger  $z$  spacings. Similarly, at  $d/D = 0.96$  and no vertical offset, the back rotor is mainly influenced by the side rotors' tip vortices, both of which in this case causing strong local downwash regions (Fig. 5.55d). At the same time, an upwash area between the side rotors counteracts the downwash from rotor 1 around  $180^\circ$  azimuth of rotor 4 (Fig. 5.56a). After raising the back rotor by  $0.12 D$  the influence of the side rotors slowly decreases, yet the back rotor also loses its shielding from the tandem interaction (Fig. 5.56b). As a result, the thrust loss area spreads to the entire front of the rotor 4 (Fig. 5.55e). The efficiency gradually improves with further increases in the vertical spacing (Fig. 5.55f); however, no improvement compared to  $z = 0$  was achieved within analysed offsets.

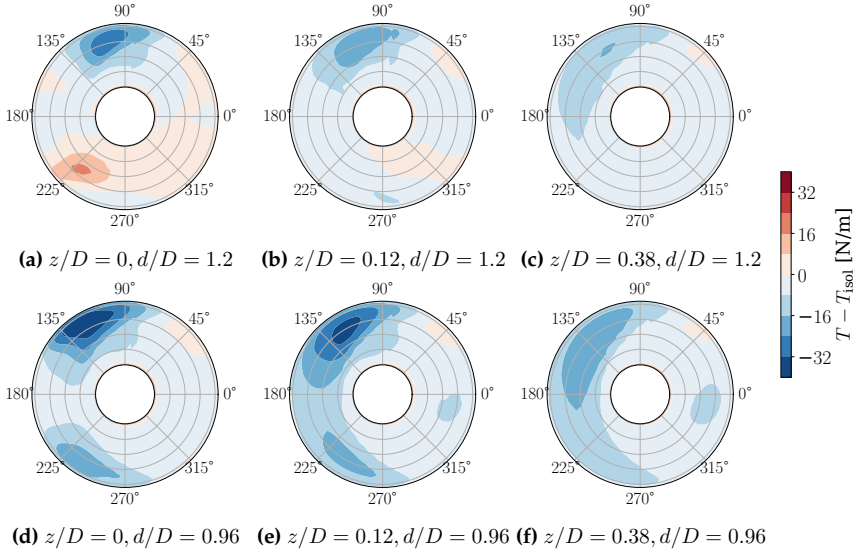


**Figure 5.55:** Change in thrust of rotor 4 in the diamond configuration with tilt  $-10^\circ$  (UPM)

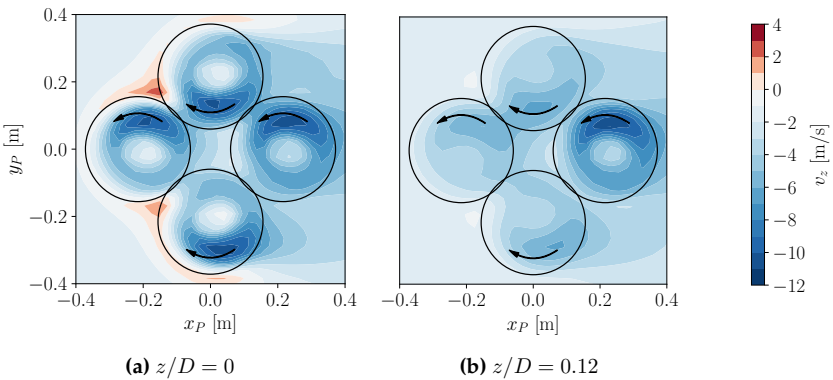


**Figure 5.56:** Velocity field in the plane of rotor 4,  $\alpha_R = -10^\circ$  and  $d/D = 0.96$  (UPM)

## 5.6 Summary

The nature of the interaction effects on quadrotor performance in forward flight was explained based on the investigation of two-rotor systems. The analysis shows the tandem alignment has a strong detrimental influence on the rear rotors operating in the downwash of the preceding rotors. The tandem interactions intensify as the tilt angle increases, leading to a thrust reduction of up to 40% with a simultaneous increase in the torque produced. The back rotors can be positively affected when positioned in the oblique alignment, where they operate in the upwash regions caused by the rolled-up tip vortices of the preceding rotors. The beneficial effects were also observed for side-by-side interactions for closer spacings, with the breaststroke system being more favourable.

The tandem interaction is dominant in square configurations, which produce less thrust than four isolated rotors at all analysed horizontal spacings. For higher nose-up tilt angles the negative effects worsen and the efficiency continues to decrease. Rotor separations with slightly overlapping blades are the most advantageous as the efficiency of the front rotors increases and the back rotors benefit from the side-by-side interactions. The performance of the diamond system is determined by the diagonal bearhug and breaststroke interactions, which improve the system performance by up to 5% compared to isolated rotors for all non-overlapping rotor spacings. For the tilt angle  $+10^\circ$ , a decrease in the torque produced by the side rotors results in the 10% increase in efficiency.

The computational results showed good agreement with the measured data for the forward rotor plane tilt; however, for the increased rotor-wake interactions at the nose-up tilt angle, the spread between the calculated values, especially for torque, could be observed. The general trends were still maintained in the simulations. While rotor phasing could be neglected for quadrotor performance, it had a significant impact on the overall sound pressure levels. Nevertheless, interaction noise remained an important factor at best-human-hearing frequencies.

Introducing a vertical offset to the back rotors in the square bearhug configuration improved its efficiency up to 5% at  $-10^\circ$  tilt angle and 11% at  $10^\circ$  tilt. Performance comparable to or higher than four isolated rotors was achieved for the close horizontal rotor spacing  $d/D = 0.96$ . Prediction of the front rotors' wake trajectory, including asymmetric wake propagation, is necessary to assess the vertical offset benefit. The trajectory of the retreating side vortices is determined by the wake-wake interaction from the bearhug alignment between the front rotors. For this reason, the effect is expected to be less significant for the square breaststroke configuration.

In contrast, adding a vertical separation to the back rotor in the diamond configuration has a negative impact on its efficiency. At  $z = 0$  inflow conditions around  $180^\circ$  azimuth of the back rotor are comparable to an isolated rotor case due to the upwash between the side rotors. However, the back rotor with a vertical offset is more exposed to the downwash from the tandem interaction with the front rotor. A gradual improvement in the rotor performance is expected for vertical separation greater than  $z/D = 0.38$  due to reduced downwash from the preceding rotors.



## 6 Discussion

A multirotor study included a wide range of geometric parameters and computational tools in order to identify interaction effects and verify the ability of the solvers to reproduce them. The applicability of the obtained conclusions to other flight cases and rotor models is discussed in the following section.

### 6.1 Real flight conditions

The test cases presented considered a purely theoretical setting of a fixed rotation speed for all rotors and neglected the influence of other vehicle components on the produced loads and noise. In practice, variable RPM control of the rotors is required to perform forward flight as well as to counteract load changes caused by interaction effects. Nevertheless, it is expected that similar conclusions could be drawn for full configurations and real flight conditions. Compensating of the excess or shortage of thrust due to interactions would require a further reduction or increase in the power required and thus the qualitative conclusion of positive/detrimental effect on rotor performance would remain the same. The loss of efficiency of the rear rotor(s) in the trimmed condition was observed for tandem configurations [23] as well as for full quadrotor simulations [155] and in-flight tests [8, 61].

RANS simulations of a full quadrotor in hover performed by Yoon et al. [156] show that although the fuselage alone produces negligible loads it can have a positive effect on the multicopter by blocking the detrimental interactions between the rotors. However, as discussed by Herz et al. [61] the presence of the fuselage in forward flight may have two effects, possibly cancelling each other, as it both shields the back rotors from the wake of the upstream rotors and decreases the back rotors' performance through its own vorticity. Overall, the impact of rotor-body interactions is considered secondary to rotor-rotor interactions. Differences between the square and diamond configurations, including an increase of the side rotors' performance for the latter, were observed in the numerical study on a quadrotor with a fuselage conducted by

Hwang et al. [64].

Forward flight with constant rotor phasing and overlapping horizontal spacing was investigated as an interesting case for multirotor interactions. In practice, synchrophasing of rotors in quadcopters could be achieved using variable pitch rotors [101].

A study by Tinney and Sirohi [140] shows that under hover conditions, motor noise can be a significant contributor at best human-hearing frequencies. However, in forward flight, the noise levels caused by rotor-rotor interactions in this range are much higher than in hover [33, 157] and are expected to dominate in the aeroacoustic spectra. Similarly, in hover, installation effects such as proximity to the airframe surface can cause significant changes in the noise signature, as shown by Zawodny et al. [157] but are expected to be less prevalent in forward flight.

## 6.2 Interactions at other advance ratios

The study of the tilt angle influence showed that the interactions intensify when the wakes of the upstream rotors propagate close to the rotor plane. For this reason, as investigated by Healy et al. [59], higher advance ratios and/or lower disc loading lead to similar effects as the wake skew angle approaches  $90^\circ$ . Nevertheless, Lee et al. [85] showed that for a given hub spacing, the interactions in a tandem configuration depend on both the wake skew angle and the density of vortex filaments. As a result, the performance loss on a back rotor increased until  $\mu = 0.11$ , after which the increasing pitch of the vortex helices was a decisive factor and the efficiency of the back rotor began to improve.

The tandem or oblique alignment interactions are expected to diminish for hover conditions. However, the predictions for the side-by-side alignment are not as straightforward. In the cases analysed, the upwash caused by the side-proximity of two rotors led to an efficiency improvement by simultaneous thrust increase and drag (torque) reduction. The effect can be explained using the blade element theory for an airfoil section as shown in Fig.6.1a. Assuming an unchanged magnitude of a lift vector, an additional upwash component causes a decrease in the inflow angle, which in turn affects the ratio between the vector components in the rotor reference system. The magnitudes of the components acting perpendicular and parallel to the rotor plane are more important than the lift value itself as they determine the rotor performance, i.e. thrust and torque respectively. A similar conclusion can be drawn for a detrimental effect, for example on the back rotor in a tandem interaction with an increase in the inflow angle and corresponding thrust reduction and torque increase

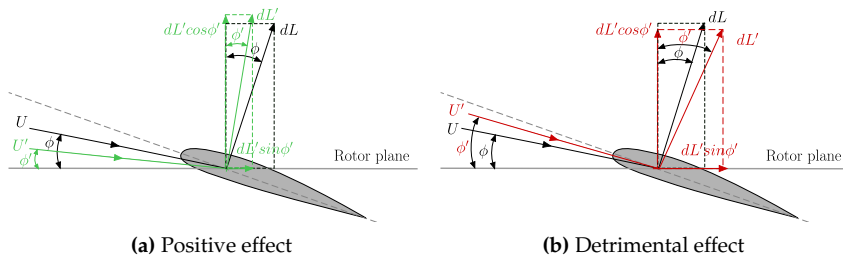


**Figure 6.1:** Observed effects of aerodynamic interactions on produced thrust and induced torque

(Fig. 6.1b). It should be noticed that the effect on torque is caused by a change in the induced (inviscid) drag, which is why it was also captured by potential methods.

The studies of side-by-side rotors in hover, described in Section 2.3 did not agree on the possible outcome of the interactions, yet the majority of them indicated a decrease in rotor efficiency. A common explanation for this result was a reduction in the induced velocity due to the counteracting upwash between the rotors, which according to the momentum theory causes a performance decrease. An apparent contradiction between the expected upwash impact based on blade element theory and momentum theory arises from the fact that both argumentations ignore the coupling between the induced velocity and the inflow angle. Actually, a loop between the two must be considered, as an upwash causes a decrease in the inflow angle, which results in increased thrust, which in turn causes an increase in the induced velocity followed again by the inflow angle reduction, and so on. This relation explains the difficulty in predicting the final outcome of the interactions and discrepancies between the cases analysed. Nevertheless, a simplified BET argumentation seems to be more accurate for higher advance ratios, while induced velocity arguments based on momentum theory could explain the hover behaviour in most cases. Corresponding changes in angle of attack, not considered so far, are discussed in the next section.

Another difficulty arises in defining the exact separation between the two possible upwash effects. Example calculations with the side-by-side bearhug configuration indicate that both effects coexist at low advance ratios (Fig. 6.2). Preliminarily, a dependence between the local skew angle and the upwash effect can be noticed, yet this topic requires a dedicated study.

Interestingly, for hover, a region of reduced efficiency inboard (between the rotors) is still accompanied by a beneficial effect at the outboard positions (Fig. 6.2a). A similar observation was made by Miesner et al. [100] for CFD calculations of an



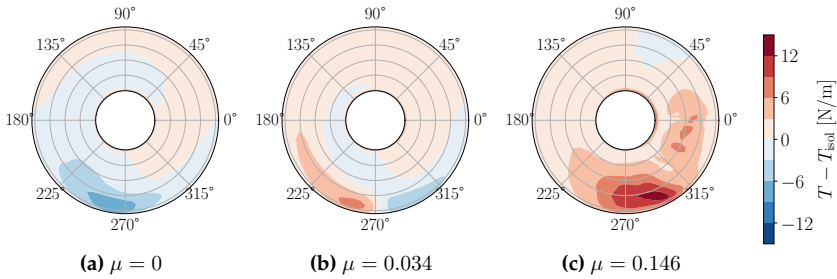


**Figure 6.2:** Effect of the bearhug alignment on thrust of rotor 1 with varying advance ratio,  $\alpha_R = 0^\circ$ ,  $d/D = 0.96$  (UPM)

octocopter configuration. The analysis of the tip vortices' trajectory showed that the proximity of the rotors draws their wakes towards each other. Based on the momentum theory, this results in greater wake contraction for the outer edges and thus higher velocities and an increase in thrust. However, for the inboard region, the wake area (vena contracta) locally increases, resulting in a lower velocity and thrust reduction.

### 6.3 Torque prediction for other blade models

The isolated rotor study shows that all applied tools were capable of capturing the general effects for both thrust and torque. Nevertheless, the capability of potential tools in predicting experimental trends, especially for torque, strongly depends on whether the effect is dominated by viscous or inviscid forces. As the latter can play a significant role in the operation of small-sized rotors, it is important to understand the origin of the error and the limitations of the applied corrections.

Based on the blade element theory described in Section 2.2.1, it can be noticed that the torque generated at each blade section is the result of two drag components  $dD\cos\phi$  and  $dL\sin\phi$ , describing the induced and viscous drag contributions respectively. Figure 6.3 shows the tilt angle effect on rotor torque predicted using BET from the isolated rotor study, including variation of both components. Changing the rotor tilt angle  $\alpha_R$  affects the inflow angle  $\phi$  and thus indirectly the angle of attack  $\alpha$  through the relation with the blade pitch  $\Theta$ . As shown in the plot, the inflow angle decreases with increasing tilt angle and so does the induced drag. A change in the viscous component is directly related to the airfoil drag characteristics presented in Fig. 6.4 for the airfoil at  $0.7R$  producing the highest blade loading. For negative tilt angles, the blade operates at moderate angles of attack, for which the drag coefficient

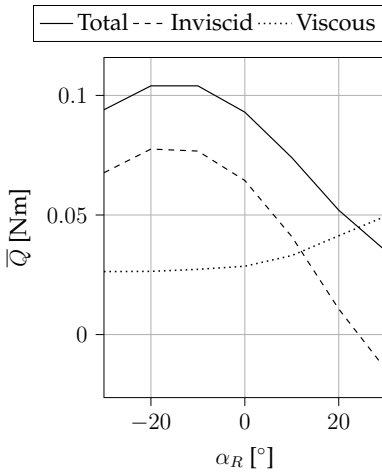


**Figure 6.3:** Tilt angle effect on torque components predicted by BET

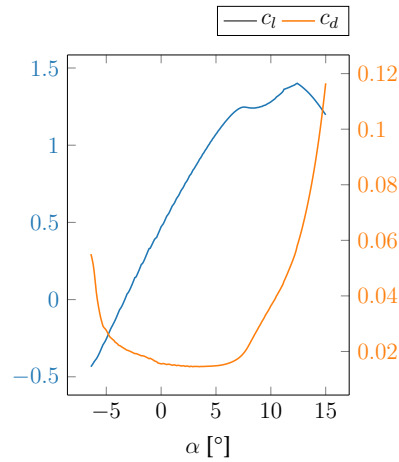


**Figure 6.4:** Aerodynamic characteristics of an airfoil at  $0.7R$  blade section

remains nearly constant, as does the resulting viscous torque. An increase in  $c_d$  due to a growth in the pressure drag for higher angles of attack can also be observed in a gradual increase in viscous torque for tilt angles above  $0^\circ$ . However, the change in induced drag remained dominant and the general trend of the tilt angle effect could be captured with potential methods. Additionally, the following observations can be made:

- A simple, post-processing viscous drag correction applied to the UPM results is not accurate for high positive tilt angles, as it does not account for the increase in drag coefficient due to flow separation. However, it provides good agreement with the results in the region where the drag coefficient is nearly independent of the angle of attack.
- The error in torque prediction by potential methods increased for higher tilt angles as the absolute torque value decreased, leading to significant discrepancies in the assessment of relative interaction effects. Additionally, for the nose-up rotor tilt, local increases in the angle of attack due to interactions led to non-negligible changes in the drag coefficient, and as a result potential methods may also fail to capture the absolute changes in produced torque. This was the case for strong oblique alignment interactions in the diamond configuration.

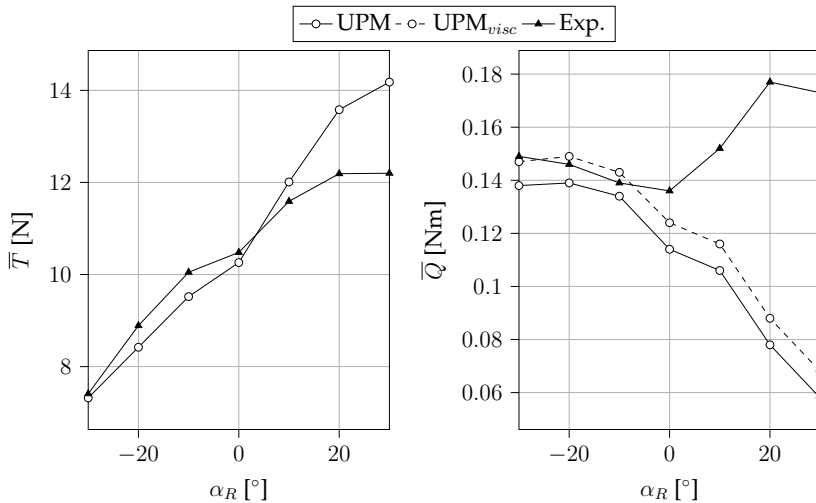


**Figure 6.5:** Effect of varying tilt angle on rotor thrust and torque at fixed rotational speed 5400 RPM and flight velocity 12.9 m/s for Aeronaut 12x6"

- The inviscid torque can be a dominant contributor, leading to a counter-intuitive reduction in total torque with increasing tilt angle (and local angles of attack). In such cases, even potential methods are capable of capturing the change in rotor torque, although they underestimate its absolute value. Naturally, this does not apply for cases where the torque trends are dominated by viscous effects.

Figure 6.5 shows the tilt angle effect for another rotor model Aeronaut 12x6" with a similar size to the analysed KDE rotor [90]. Due to a larger blade pitch  $\Theta$ , the Aeronaut rotor operated at higher angles of attack for the same flight conditions, which was likely to cause flow separation, especially at low Reynolds numbers. As a result, stall effects can be recognised for the analysed range of positive tilt angles, reflected in the experimental results by a thrust reduction and a rapid torque increase. Both effects could not be captured by the potential code UPM, although a simple viscous torque correction to the UPM output ensured a good agreement with the measurements for negative tilt angles. The calculated trend at more positive tilt angles still only reflected a reduction in the induced drag. Coupling with a boundary layer solver would be required to improve accuracy in this region.

## 7 Conclusions

Quadrotor configurations were studied using experimental data and computations performed with solvers of different fidelity levels, including the URANS tool and potential methods representing the rotor geometry as a thick blade model, lifting surface and lifting line. Interaction effects were evaluated based on changes in thrust and torque together with the analysis of the flow field below the rotor plane measured with PIV. Differences between square bearhug, square breaststroke and diamond configurations were investigated for varying tilt angles, horizontal and vertical rotor spacing as well as rotor phasing. In the preceding isolated rotor study, the applicability of a simple BET tool was compared with higher-fidelity methods for simulating rotor performance and BPF noise. The observed effects were explained using vortex visualisation with BOS. The following conclusions were drawn:

- The diamond configuration showed increased efficiency compared to both square configurations and advantages over four isolated rotors for all non-overlapping horizontal rotor spacings. In contrast, the maximum efficiency of the square configuration was equal to four isolated rotors and was achieved for the slightly overlapping hub spacing  $d/D = 0.96$  at a negative tilt angle of  $-10^\circ$ .
- Intensified interactions at the  $+10^\circ$  tilt angle led to a higher increase in efficiency for the diamond configuration due to a simultaneous thrust increase and torque reduction. The maximum efficiency gain of 10 % over four isolated rotors was achieved at a hub spacing of  $d/D = 1.2$ . In contrast, strong interactions further reduce the efficiency of both square configurations. The square breaststroke configuration showed advantages over the square bearhug alignment at hub spacings below  $d/D = 1.2$ .
- Adding a vertical offset to the back rotors in a square configuration is a more efficient method of improving the system performance than increasing the hub spacing. A vertical offset of  $z/D = 0.38$  was enough to cancel the thrust loss caused by strong interactions at the  $10^\circ$  tilt for the square bearhug configuration

with  $d/D = 0.96$ . However, a prediction of the change in the vortex trajectories of the front rotors due to their side-by-side interaction, as well as a consideration of the wake asymmetry, is necessary to estimate the vertical spacing required. Raising the back rotor in the diamond configuration only reduced the advantage over four isolated rotors achieved at  $z/D = 0$  within the analysed range of vertical offsets.

- Changes in rotor phasing have a negligible influence on quadrotor performance. Nevertheless, the acoustic interference effects can significantly reduce the OASPL levels (represented in the first few harmonics) for orthogonal phasing in the square configuration and tip-to-tip phasing in the diamond configuration. Analysis of the spectra for the observer below the quadrotor showed that, at higher harmonics of the blade passing frequency, a greater hub spacing resulted in decreased rotor-rotor interactions and is more effective method of noise reduction than synchrophasing of the rotors.
- The BET tool showed agreement with higher fidelity methods in estimating time-averaged loads and BPF noise levels of an isolated rotor. Nevertheless, the method loses applicability for cases with strong self-induced wake interactions, leading to discrepancies in the prediction of transient loads and noise directivity.

Additionally, the following answers were found to the driving questions of the thesis:

*Can a potential free wake solver be applied for aeroacoustic and aerodynamic simulation of a small-scale UAV rotor?*

Free wake solvers are capable of producing unsteady results and capturing wake interactions with low computational effort, yet at the cost of neglecting compressible and viscous effects. While the first assumption is fully justified for small-size rotors, the omission of viscosity can lead to considerable errors in the simulations of low Reynolds number flows. Nevertheless, even though the probability of flow separations and transitions causing load changes and increasing the broadband noise components is much higher than for full-scale helicopter rotors, these effects cannot be pre-assumed for all UAV rotors and flight conditions. In the cases studied, tonal noise was clearly dominant in the aeroacoustic spectra. The isolated rotor study showed that potential tools reproduced the trends in loads and BPF noise comparable to higher-fidelity solvers and experimental results. In contrast to the BET method,

free wake tools captured the influence of vortices during self-rotor interactions characteristic of the operation with a nose-up rotor tilt. Although potential methods underestimate the absolute torque value, they proved useful for estimating qualitative trends in the torque change. For moderate flight conditions a simple correction for profile drag ensured good agreement with measured torque values. Discrepancies observed between similar potential methods such as UPM and RAMSYS indicate that modelling decisions regarding vortex core and distortion models can influence performance and aeroacoustic predictions.

*Is a potential solver applicable for estimation of interaction effects for a quadrotor in forward flight?*

While the main interaction phenomena are similar for small and large scale rotors, i.e. independent of the Reynolds number and reproducible with potential tools, certain limitations of free wake solvers have to be considered when simulating multirotor flows. An undeniable advantage of such methods is their ability to capture the complexity of the rotor flow, including the wake asymmetry of fixed-pitch rotors, self-induced and mutual wake interactions. Nevertheless, the solution shows a dependence on the empirical models applied, especially apparent for strong BVI interactions at nose-up tilt angles. In comparison, the choice of a blade model (thick blade/ lifting surface/ lifting line) had a secondary influence on the assessment of interaction effects. The modelling choices are also reflected in the aeroacoustic results. The roll-up model used ensured good agreement in the OASPL estimation with the CFD tool, yet overestimated the noise levels due to unsteady loading at higher frequencies. The simulation of longer wakes, necessary to capture rotor-rotor interactions, can require setting unphysically high vortex core radii to maintain a stable solution and is associated with a quadratic growth of computational expense.

Viscous effects such as flow separation can be triggered by aerodynamic interactions, even if they would not have occurred for an isolated rotor under equivalent flight conditions. As a result, discrepancies in load prediction were observed for cases with strong upwash caused by diagonal breaststroke interaction in the diamond configuration. The application of aerodynamic airfoil characteristics to account for viscosity requires particular caution in the case of small-scale rotors, as the quality of the look-up data at low Reynolds numbers, including the post-stall prediction, has a large influence on the results.

Potential solvers are able to predict the change in induced drag due to rotor-rotor interactions while underestimating the absolute torque values. Therefore, although

they cannot be used to estimate relative changes in multirotor efficiency due to interactions, they could capture an absolute increase or decrease of torque for cases without significant flow separation. Additionally, qualitative experimental trends could already be observed in the relative results.

*What are the types of aerodynamic interactions in quadrotor configurations?*

For the square configuration, the following main interactions could be identified:

- **The tandem interaction** was manifested by a reduction of the back rotors' efficiency (thrust decrease and torque increase) due to the downwash of the front rotors, and a slight efficiency improvement of the front rotors. It was more pronounced for cases, where the wake reached the rotor plane, and thus showed a strong dependence on the tilt angle. It could be counteracted by adding the vertical offset to the back rotors.
- **The side-by-side interaction** occurred due to the upwash generated between the two front and the two back rotors, and resulted in an efficiency increase for the advance ratio analysed. It had the greatest influence for close, slightly overlapping rotor spacing as well as higher tilt angles. A larger benefit was observed for the breaststroke configuration compared to the bearhug alignment due to the stronger interaction of the advancing side vortices.

The diamond configuration was characterised by the following interactions:

- **The oblique interaction** had a positive impact on the back side rotor's efficiency due to the upwash from the front rotor's vorticity. The effect was more pronounced for the diagonal breaststroke alignment and positive tilt angles when the vortices propagated closer to the rotor plane. While the benefit to the back rotors was countered by the downwash influence for overlapping rotors, the efficiency of the front rotor increased with decreasing rotor spacing.
- **The mixed interaction** was observed for the rearmost rotor in the diamond configuration. A positive impact from the diagonal alignment was limited due to the change in the side rotors' vortex propagation after interaction with the front rotor. Nevertheless, the upwash between the side rotors mitigated the downwash influence from the tandem interaction with the front rotor around  $180^\circ$  azimuth. This effect vanished after introducing a vertical offset to the back rotor and consequently no additional benefit for the diamond configuration was observed within the range of vertical spacings analysed.

# References

- [1] G. Abate and W. Shyy, "Bio-Inspiration of Morphing for Micro Air Vehicles", *Morphing Aerospace Vehicles and Structures*, Chichester, United Kingdom: John Wiley & Sons Ltd, 2012, pp. 41–53, DOI: 10.1002/9781119964032.ch3.
- [2] I. H. Abbott, A. E. Von Doenhoff, and L. Stivers, "Summary of Airfoil Data", Report No. 824, National Advisory Committee for Aeronautics, 1945.
- [3] R. J. Adrian and J. Westerweel, *Particle Image Velocimetry*, Cambridge, United Kingdom: Cambridge University Press, 2011.
- [4] S. R. Ahmed and V. T. Vidjaja, "Unsteady Panel Method Calculation of Pressure Distribution on BO 105 Model Rotor Blades", *Journal of the American Helicopter Society*, Vol. 43, No. 1, 1998, pp. 47–56, DOI: 10.4050/JAHS.43.47.
- [5] E. Alvarez, T. Critchfield, A. Ning, and A. Schenk, "Rotor-on-Rotor Aeroacoustic Interactions of Multirotor in Hover", *Vertical Flight Society 76th Annual Forum*, Virtual, Oct. 2020, DOI: 10.4050/F-0076-2020-16489.
- [6] E. J. Alvarez and A. Ning, "Modeling Multirotor Aerodynamic Interactions Through the Vortex Particle Method", *AIAA Aviation 2019 Forum*, Dallas, Texas, June 2019, DOI: 10.2514/6.2019-2827.
- [7] D. A. Anderson, Tannehill, J.C., and Pletcher, R.H., *Computational Fluid Mechanics and Heat Transfer*. Vol. 172, 1986.
- [8] A. Atte, J. Rauleder, and D. Wylie, "Experimental Investigation of Multi-Rotor Aerodynamic Interactions", *Vertical Flight Society 78th Annual Forum*, Fort Worth, Texas, USA, July 2022, DOI: 10.4050/F-0078-2022-17467.
- [9] L. J. Ayton, J. R. Gill, and N. Peake, "The Importance of the Unsteady Kutta Condition When Modelling Gust–Aerofoil Interaction", *Journal of Sound and Vibration*, Vol. 378, 2016, pp. 28–37, DOI: 10.1016/j.jsv.2016.05.036.
- [10] M. Barbarino, F. Petrosino, and A. Visingardi, "A High-Fidelity Aeroacoustic Simulation of a VTOL Aircraft in an Urban Air Mobility Scenario", *Aerospace Science and Technology*, Vol. 125, 2022, DOI: 10.1016/j.ast.2021.107104.



- [11] M. Barbarino and D. Bianco, "A BEM–FMM Approach Applied to the Combined Convected Helmholtz Integral Formulation for the Solution of Aeroacoustic Problems", *Computer Methods in Applied Mechanics and Engineering*, Vol. **342**, 2018, pp. 585–603, DOI: 10.1016/j.cma.2018.07.034.
- [12] D. Barcelos, A. Kolaei, and G. Bramesfeld, "Aerodynamic Interactions of Quadrotor Configurations", *Journal of Aircraft*, Vol. **57**, No. 6, 2020, pp. 1074–1090, DOI: 10.2514/1.C035614.
- [13] O. Bergmann, F. Götten, C. Braun, and F. Janser, "Comparison and Evaluation of Blade Element Methods against RANS Simulations and Test Data", *CEAS Aeronautical Journal*, Vol. **13**, No. 2, 2022, pp. 535–557, DOI: 10.1007/s13272-022-00579-1.
- [14] M. Bhagwat and J. Leishman, "Generalized Viscous Vortex Model for Application to Free-Vortex Wake and Aeroacoustic Calculations", *American Helicopter Society 58th Annual Forum*, Montreal, Canada, Jan. 2002.
- [15] R. Boisard, "Aerodynamic Investigation of a Helicopter Rotor Hovering in the Vicinity of a Building", *74th American Helicopter Society Forum*, Phoenix, Arizona, USA, May 2018.
- [16] R. Boisard, "Numerical Analysis of Rotor/Propeller Aerodynamic Interactions on a High-Speed Compound Helicopter", *Journal of the American Helicopter Society*, Vol. **67**, No. 1, 2022, DOI: 10.4050/JAHS.67.012005.
- [17] J. Brandt and M. Selig, "Propeller Performance Data at Low Reynolds Numbers", *49th AIAA Aerospace Sciences Meeting Including the New Horizons Forum and Aerospace Exposition*, Orlando, Florida, USA, Jan. 2011, DOI: 10.2514/6.2011-1255.
- [18] K. S. Brentner and F. Farassat, "Modeling Aerodynamically Generated Sound of Helicopter Rotors", *Progress in Aerospace Sciences*, Vol. **39**, No. 2, 2003, pp. 83–120, DOI: 10.1016/S0376-0421(02)00068-4.
- [19] T. Brooks, C. Burley, Jr. Boyd D., and J. Jolly R., "Aeroacoustic Codes for Rotor Harmonic and BVI Noise - CAMRAD.Mod1/HIRES", *Journal of the American Helicopter Society*, Vol. **45**, No. 2, 2000, pp. 63–79, DOI: 10.4050/JAHS.45.63.
- [20] T. F. Brooks, J. R. Jolly, and M. A. Marcolini, "Helicopter Main-Rotor Noise. Determination of Source Contributions Using Scaled Model Data", NASA-TP-2825, 1988.

- [21] T. F. Brooks and C. L. Burley, "Blade Wake Interaction Noise for a Main Rotor", *Journal of the American Helicopter Society*, Vol. **49**, No. 1, 2004, pp. 11–27, DOI: 10.4050/JAHS.49.11.
- [22] T. F. Brooks, D. S. Pope, and M. A. Marcolini, "Airfoil Self-Noise and Prediction", NASA Reference Publication 1218, 1989.
- [23] J. Cai, S. Gunasekaran, and M. Ol, "Vertically Offset Overlapping Propellers in Tandem Configuration", *AIAA SCITECH 2023 Forum*, National Harbor, MD & Online, Jan. 2023, DOI: 10.2514/6.2023-2464.
- [24] P. Candeloro, D. Ragni, and T. Pagliaroli, "Small-Scale Rotor Aeroacoustics for Drone Propulsion: A Review of Noise Sources and Control Strategies", *Fluids*, Vol. **7**, No. 8, 8 2022, DOI: 10.3390/fluids7080279.
- [25] D. Casalino, "An Advanced Time Approach for Acoustic Analogy Predictions", *Journal of Sound and Vibration*, Vol. **261**, No. 4, 2003, pp. 583–612, DOI: 10.1016/S0022-460X(02)00986-0.
- [26] D. Casalino, M. Barbarino, and A. Visingardi, "Simulation of Helicopter Community Noise in Complex Urban Geometry", *AIAA Journal*, Vol. **49**, No. 8, 2011, pp. 1614–1624, DOI: 10.2514/1.J050774.
- [27] W. Castles and J. H. De Leeuw, "The Normal Component of the Induced Velocity in the Vicinity of a Lifting Rotor and Some Examples of Its Application", NACA-TR-1184, Georgia Institute of Technology, 1954.
- [28] M. Cerny and C. Breitsamter, "Investigation of Small-Scale Propellers under Non-Axial Inflow Conditions", *Aerospace Science and Technology*, Vol. **106**, 2020, DOI: 10.1016/j.ast.2020.106048.
- [29] G. H. Chen, G. F. Nunez, C. R. Russel, M. P. Avera, and J. M. Dotterweich, "Wind Tunnel Test Results for an Overlapped Quadrotor Configured UAS", Phoenix, Arizona, USA, May 2018.
- [30] R. T. N. Chen, "A Survey of Nonuniform Inflow Models for Rotorcraft Flight Dynamics and Control Applications", Nasa Technical Memorandum 102219, 1990.
- [31] S. Conley and D. Shirazi, "Comparing Simulation Results from CHARM and RotCFD to the Multirotor Test Bed Experimental Data", *AIAA Aviation Forum*, Virtual, Aug. 2021, DOI: 10.2514/6.2021-2540.

- [32] B. Davoudi and K. Duraisamy, "A Hybrid Blade Element Momentum Model for Flight Simulation of Rotary Wing Unmanned Aerial Vehicles", *AIAA Aviation 2019 Forum*, Dallas, Texas, June 2019, DOI: 10.2514/6.2019-2823.
- [33] T. Dbouk and D. Drikakis, "Computational Aeroacoustics of Quadcopter Drones", *Applied Acoustics*, Vol. **192**, 2022, DOI: 10.1016/j.apacoust.2022.108738.
- [34] R. De Vries, N. Van Arnhem, T. Sinnige, R. Vos, and L. L. Veldhuis, "Aerodynamic Interaction between Propellers of a Distributed-Propulsion System in Forward Flight", *Aerospace Science and Technology*, Vol. **118**, 2021, DOI: 10.1016/j.ast.2021.107009.
- [35] R. W. Deters, G. K. Ananda Krishnan, and M. S. Selig, "Reynolds Number Effects on the Performance of Small-Scale Propellers", *32nd AIAA Applied Aerodynamics Conference*, Atlanta, Georgia, USA, June 2014, DOI: 10.2514/6.2014-2151.
- [36] R. W. Deters, S. Kleinke, and M. S. Selig, "Static Testing of Propulsion Elements for Small Multirotor Unmanned Aerial Vehicles", *35th AIAA Applied Aerodynamics Conference*, Denver, Colorado, USA, June 2017, DOI: 10.2514/6.2017-3743.
- [37] R. C. Dingeldein, "Wind-Tunnel Studies of the Performance of Multirotor Configurations", NACA-TN-3236, 1954.
- [38] *DJI Phantom 4 Pro*, DJI Official, <https://www.dji.com/de/phantom-4-pro-v2> (visited on 03/22/2024).
- [39] M. Drela, "XFOIL: An Analysis and Design System for Low Reynolds Number Airfoils", *Low Reynolds Number Aerodynamics. Lecture Notes in Engineering*, ed. by T. J. Mueller, vol. 54, Berlin, Heidelberg: Springer, 1989, pp. 1–12, DOI: 10.1007/978-3-642-84010-4\_1.
- [40] L. Dürrwächter, "Simulation of Installation Effects on Open-Rotor Acoustics with a Coupled Numerical Tool Chain", PhD thesis, Germany: University of Stuttgart, 2020.
- [41] L. Dürrwächter, M. Keßler, and E. Krämer, "Numerical Assessment of Open-Rotor Noise Shielding with a Coupled Approach", *AIAA Journal*, Vol. **57**, No. 5, 2019, DOI: 10.2514/1.J057531.
- [42] *EHang EH216-S (Production Model)*, <https://evtol.news/ehang-216> (visited on 03/22/2024).

- [43] F. Farassat, "Derivation of Formulations 1 and 1A of Farassat", NASA/TM-2007-214853, 2007.
- [44] F. Farassat, "Linear Acoustic Formulas for Calculation of Rotating Blade Noise", *AIAA Journal*, Vol. **19**, No. 9, 1981, pp. 1122–1130, DOI: 10.2514/3.60051.
- [45] F. Farassat and G. P. Succi, "A Review of Propeller Discrete Frequency Noise Prediction Technology with Emphasis on Two Current Methods for Time Domain Calculations", *Journal of Sound and Vibration*, Vol. **71**, No. 3, 1980, pp. 399–419, DOI: 10.1016/0022-460X(80)90422-8.
- [46] Federal Aviation Administration and U.S. Department of Transportation, *Helicopter Flying Handbook*, FAA-H-8083-21B, 2019.
- [47] J. E. Ffowcs Williams, D. L. Hawkings, and M. J. Lighthill, "Sound Generation by Turbulence and Surfaces in Arbitrary Motion", *Philosophical Transactions of the Royal Society of London. Series A, Mathematical and Physical Sciences*, Vol. **264**, No. 1151, 1969, pp. 321–342, DOI: 10.1098/rsta.1969.0031.
- [48] Q. Gallas, R. Boisard, J.-C. Monnier, J. Pruvost, and A. Gilliot, "Experimental and Numerical Investigation of the Aerodynamic Interactions between a Hovering Helicopter and Surrounding Obstacles", *43rd European Rotorcraft Forum*, Milan, Italy, Sept. 2017.
- [49] A. D. Gardner, A. A. Kostek, F. Löble, and J. N. Braukmann, "Experiments and Modelling of Multicopter Rotor Response to Sinusoidal Gusts", *Vertical Flight Society 80th Annual Forum*, Montreal, Canada, May 2024.
- [50] M. Gennaretti and G. Bernardini, "Novel Boundary Integral Formulation for Blade-Vortex Interaction Aerodynamics of Helicopter Rotors", *AIAA Journal*, Vol. **45**, No. 6, 2007, pp. 1169–1176, DOI: 10.2514/1.18383.
- [51] H. Glauert, "A General Theory of the Autogyro", Reports and Memoranda No. 1111, Aeronautical Research Committee, 1926.
- [52] E. Grande, G. Romani, D. Ragni, F. Avallone, and D. Casalino, "Aeroacoustic Investigation of a Propeller Operating at Low Reynolds Numbers", *AIAA Journal*, Vol. **60**, No. 2, 2022, pp. 860–871, DOI: 10.2514/1.J060611.
- [53] D. A. Griffiths and J. G. Leishman, "A Study of Dual-Rotor Interference and Ground Effect Using a Free-Vortex Wake Model", *American Helicopter Society 58th Annual Forum*, Montreal, Canada, Nov. 2002.

- [54] O. Gur and A. Rosen, "Comparison between Blade-Element Models of Propellers", *The Aeronautical Journal*, Vol. **112**, No. 1138, 2008, pp. 689–704, DOI: 10.1017/S0001924000002669.
- [55] O. Gur and A. Rosen, "Design of Quiet Propeller for an Electric Mini Unmanned Air Vehicle", *Journal of Propulsion and Power*, Vol. **25**, No. 3, 2009, pp. 717–728, DOI: 10.2514/1.38814.
- [56] O. Gur and A. Rosen, "Propeller Performance at Low Advance Ratio", *Journal of Aircraft*, Vol. **42**, No. 2, 2005, pp. 435–441, DOI: 10.2514/1.6564.
- [57] D. B. Hanson and M. R. Fink, "The Importance of Quadrupole Sources in Prediction of Transonic Tip Speed Propeller Noise", *Journal of Sound and Vibration*, Vol. **62**, No. 1, 1979, pp. 19–38, DOI: 10.1016/0022-460X(79)90554-6.
- [58] R. Healy, F. Gandhi, and M. Mistry, "Computational Investigation of Multirotor Interactional Aerodynamics with Hub Lateral and Longitudinal Canting", *AIAA Journal*, Vol. **60**, No. 2, 2022, pp. 872–882, DOI: 10.2514/1.J060530.
- [59] R. Healy, M. Misiorowski, and F. Gandhi, "A CFD-Based Examination of Rotor-Rotor Separation Effects on Interactional Aerodynamics for eVTOL Aircraft", *Journal of the American Helicopter Society*, Vol. **67**, No. 1, 2022, pp. 1–12, DOI: 10.4050/JAHS.67.012006.
- [60] B. S. Henderson and D. Huff, "Electric Motor Noise for Small Quadcopters: Part II - Source Characteristics and Predictions", *2018 AIAA/CEAS Aeroacoustics Conference*, Atlanta, Georgia, USA, June 2018, DOI: 10.2514/6.2018-2953.
- [61] S. Herz, A. Atte, D. Seth, J. Rauleder, and M. McCrink, "Impact of Rotor-Rotor and Rotor-Body Aerodynamic Interactions on Quadrotor Vehicle Performance", *Vertical Flight Society 79th Annual Forum*, West Palm Beach, Florida, May 2023, DOI: 10.4050/F-0079-2023-18180.
- [62] J. L. Hess, "Panel Methods in Computational Fluid Dynamics", *Annual Review of Fluid Mechanics*, Vol. **22**, No. 1, 1990, pp. 255–274, DOI: 10.1146/annurev.fl.22.010190.001351.
- [63] H. H. Hubbard, "Aeroacoustics of Flight Vehicles: Theory and Practice." NASA-RP-1258-VOL-1, 1991.
- [64] J. Y. Hwang, M. K. Jung, and O. J. Kwon, "Numerical Study of Aerodynamic Performance of a Multirotor Unmanned-Aerial-Vehicle Configuration", *Journal of Aircraft*, Vol. **52**, No. 3, 2015, pp. 839–846, DOI: 10.2514/1.C032828.

- [65] N. Intaratep, W. N. Alexander, W. J. Devenport, S. M. Grace, and A. Dropkin, "Experimental Study of Quadcopter Acoustics and Performance at Static Thrust Conditions", *22nd AIAA/CEAS Aeroacoustics Conference*, Lyon, France, May 2016, DOI: 10.2514/6.2016-2873.
- [66] Z. Jia and S. Lee, "Aeroacoustic Analysis of a Side-by-Side Hybrid VTOL Aircraft", *Vertical Flight Society 76th Annual Forum*, Virginia Beach, Virginia, USA, Oct. 2020, DOI: 10.4050/F-0076-2020-16491.
- [67] Z. Jia and S. Lee, "Computational Study on Noise of Urban Air Mobility Quadrotor Aircraft", *Journal of the American Helicopter Society*, Vol. 67, No. 1, 2022, pp. 1–15, DOI: 10.4050/JAHS.67.012009.
- [68] W. Johnson, *Helicopter Theory*, New York, USA: Dover Publications, 1980.
- [69] J. Katz and A. Plotkin, *Low-Speed Aerodynamics*, 2nd ed., Cambridge, United Kingdom: Cambridge University Press, 2001, DOI: 10.1017/CBO9780511810329.
- [70] KDE-CF125-DP Propeller Blades, 12.5" x 4.3, Dual-Edition Series (CW/CCW Pair), KDE Direct, <https://www.kdedirect.com/products/kde-cf125-dp> (visited on 04/08/2024).
- [71] M. Kessler and S. Wagner, "Source-Time Dominant Aeroacoustics", *Computers & Fluids*, Vol. 33, No. 5, 2004, pp. 791–800, DOI: 10.1016/j.compfluid.2003.06.012.
- [72] C. N. Keys, "Rotary-Wing Aerodynamics. Volume II - Performance Prediction of Helicopters." NASA Contractor Report 3083, 1979.
- [73] J. Ko, J. Kim, and S. Lee, "Computational Study of Wake Interaction and Aeroacoustic Characteristics in Multirotor Configurations", *InterNoise Conference*, Madrid, Spain, Sept. 2019.
- [74] A. Kolaei, D. Barcelos, and G. Bramesfeld, "Experimental Analysis of a Small-Scale Rotor at Various Inflow Angles", *International Journal of Aerospace Engineering*, Vol. 2018, 2018, DOI: 10.1155/2018/2560370.
- [75] A. A. Kostek, J. N. Braukmann, F. Lößle, A. D. Gardner, V. Riziotis, S. Miesner, M. Keßler, A. Visingardi, and R. Boisard, "Experimental Investigation of Quadrotor Aerodynamics with Computational Cross-Validation", *Vertical Flight Society 79th Annual Forum*, West Palm Beach, FL, USA, May 2023, DOI: 10.4050/F-0079-2023-17991.

- [76] A. A. Kostek, J. N. Braukmann, F. Löble, S. Miesner, A. Visingardi, R. Boisard, V. Riziotis, M. Keßler, and A. D. Gardner, "Experimental and Computational Investigation of Aerodynamic Interactions in Quadrotor Configurations", *Journal of the American Helicopter Society*, Vol. 69, No. 2, 2024, pp. 1–17, DOI: 10.4050/JAHS.69.022009.
- [77] A. A. Kostek, F. Löble, R. Wickersheim, M. Keßler, R. Boisard, G. Reboul, A. Visingardi, M. Barbarino, and A. D. Gardner, "Experimental Investigation of UAV Rotor Aeroacoustics and Aerodynamics with Computational Cross-Validation", *CEAS Aeronautical Journal* 2023, DOI: 10.1007/s13272-023-00680-z.
- [78] U. Kowarsch, C. Oehrle, M. Hollands, M. Keßler, and E. Krämer, "Computation of Helicopter Phenomena Using a Higher Order Method", *High Performance Computing in Science and Engineering '13*, Cham, Switzerland: Springer International Publishing, 2013, pp. 423–438, DOI: 10.1007/978-3-319-02165-2\_29.
- [79] T. Krebs, G. Bramesfeld, and J. Cole, "Transient Thrust Analysis of Rigid Rotors in Forward Flight", *Aerospace*, Vol. 9, No. 1, 2022, DOI: 10.3390/aerospace9010028.
- [80] N. Kroll, B. Eisfeld, and H. M. Bleecke, "The Navier-Stokes Code FLOWer", *Portable Parallelization of Industrial Aerodynamic Applications (POPINDA)*, vol. 71, Notes on Numerical Fluid Mechanics, 1991, pp. 58–71.
- [81] U. J. Kurze, "Noise Reduction by Barriers", *The Journal of the Acoustical Society of America*, Vol. 55, No. 3, 2005, pp. 504–518, DOI: 10.1121/1.1914528.
- [82] H. Lee, B. Sengupta, M. S. Araghizadeh, and R. S. Myong, "Review of Vortex Methods for Rotor Aerodynamics and Wake Dynamics", *Advances in Aerodynamics*, Vol. 4, No. 1, 2022, DOI: 10.1186/s42774-022-00111-3.
- [83] H. Lee, B. Sengupta, M. S. Araghizadeh, and R. S. Myong, "Review of Vortex Methods for Rotor Aerodynamics and Wake Dynamics", *Advances in Aerodynamics*, Vol. 4, No. 1, 2022, p. 20, DOI: 10.1186/s42774-022-00111-3.
- [84] H. Lee and D. Lee, "Rotor Interactional Effects on Aerodynamic and Noise Characteristics of a Small Multirotor Unmanned Aerial Vehicle", *Physics of Fluids*, Vol. 32, No. 4, 2020, DOI: 10.1063/5.0003992.

- [85] J. Lee, S. Oh, K. Yee, and D.-K. Kim, "Numerical Investigation on Overlap Effects of Tandem Rotors in Forward Flight", *International Journal of Aeronautical and Space Sciences*, Vol. 10, No. 2, 2009, pp. 63–76, DOI: 10.5139/IJASS.2009.10.2.063.
- [86] J. Lee, K. Yee, and S. Oh, "Aerodynamic Characteristic Analysis of Multi-Rotors Using a Modified Free-Wake Method", *Transactions of the Japan Society for Aeronautical and Space Sciences*, Vol. 52, No. 177, 2009, pp. 168–179, DOI: 10.2322/tjsass.52.168.
- [87] J. G. Leishman and T. S. Beddoes, "A Semi-Empirical Model for Dynamic Stall", *Journal of the American Helicopter Society*, Vol. 34, No. 3, 1989, pp. 3–17, DOI: 10.4050/JAHS.34.3.3.
- [88] J. G. Leishman, *Principles of Helicopter Aerodynamics*, Cambridge, United Kingdom: Cambridge University Press, 2016.
- [89] J. G. Leishman, M. J. Bhagwat, and A. Bagai, "Free-Vortex Filament Methods for the Analysis of Helicopter Rotor Wakes", *Journal of Aircraft*, Vol. 39, No. 5, 2002, pp. 759–775, DOI: 10.2514/2.3022.
- [90] F. Lößle, "Experimentelle Untersuchung der Aerodynamik und Aeroakustik kleiner Rotoren im Schweben- und Vorwärtsflug", PhD thesis, Germany: Leibniz University Hannover, 2024.
- [91] F. Lößle, A. Kostek, C. Schwarz, and R. Schmid, "Experimental Measurement of a UAV Rotor's Acoustic Emission", *New Results in Numerical and Experimental Fluid Mechanics XIII*, 2021, pp. 387–396, DOI: 10.1007/978-3-030-79561-0\_37.
- [92] F. Lößle, A. Kostek, C. Schwarz, R. Schmid, A. Gardner, and M. Raffel, "Aerodynamics of Small Rotors in Hover and Forward Flight", *48th European Rotorcraft Forum*, Winterthur, Switzerland, Sept. 2022.
- [93] J. Luo, L. Zhu, and G. Yan, "Novel Quadrotor Forward-Flight Model Based on Wake Interference", *AIAA Journal*, Vol. 53, No. 12, 2015, pp. 3522–3533, DOI: 10.2514/1.J053011.
- [94] R. MacNeill and D. Verstraete, "Blade Element Momentum Theory Extended to Model Low Reynolds Number Propeller Performance", *The Aeronautical Journal*, Vol. 121, No. 1240, 2017, pp. 835–857, DOI: 10.1017/aer.2017.32.
- [95] Z. Maekawa, "Noise Reduction by Screens", *Applied Acoustics*, Vol. 1, No. 3, 1968, pp. 157–173, DOI: 10.1016/0003-682X(68)90020-0.



- [96] F. Mahmuddin, S. Klara, H. Sitepu, and S. Hariyanto, "Airfoil Lift and Drag Extrapolation with Viterna and Montgomerie Methods", *Energy Procedia*, Vol. **105**, 2017, pp. 811–816, DOI: 10.1016/j.egypro.2017.03.394.
- [97] J. Manghnani, V. Domogalla, R. Ewert, and J. W. Delfs, "Noise Emissions from Installed Propeller-Wing Configurations Using Mid-Fidelity Unsteady Panel Method Coupled to FW-H Equation-Based Solver.", *DJINN-ENODISE Conference*, Berlin, Germany, Nov. 2023.
- [98] J. E. Marte and D. W. Kurtz, "A Review of Aerodynamic Noise From Propellers, Rofors, and Lift Fans", Technical Report 32-1462, California Institute of Technology, 1970.
- [99] M. H. McCrink and J. W. Gregory, "Blade Element Momentum Modeling of Low-Reynolds Electric Propulsion Systems", *Journal of Aircraft*, Vol. **54**, No. 1, 2017, pp. 163–176, DOI: 10.2514/1.C033622.
- [100] S. Miesner, M. Kessler, and E. Kramer, "High-Fidelity Simulations of Rotors in Compact Configuration", *Vertical Flight Society 78th Annual Forum*, Fort Worth, Texas, May 2022, DOI: 10.4050/F-0078-2022-17466.
- [101] D. Miljković, "Methods for Attenuation of Unmanned Aerial Vehicle Noise", *41st International Convention on Information and Communication Technology, Electronics and Microelectronics (MIPRO)*, Opatija, Croatia, May 2018, DOI: 10.23919/MIPRO.2018.8400169.
- [102] M. Misorowski, F. Gandhi, and A. A. Oberai, "Computational Study on Rotor Interactional Effects for a Quadcopter in Edgewise Flight", *AIAA Journal*, Vol. **57**, No. 12, 2019, pp. 5309–5319, DOI: 10.2514/1.J058369.
- [103] L. Morino, M. Gennaretti, and P. Petrocchi, "A General Theory of Potential Aerodynamics with Applications to Helicopter Rotor-Fuselage Interaction", *Boundary Element Methods*, Berlin, Germany: Springer, 1992, pp. 242–251, DOI: 10.1007/978-3-662-06153-4\_27.
- [104] M. Mudry, "La Theorie Generale Des Nappes Et Filaments Tourbillonnaires Et Ses Applications a L'aerodynamique Instationnaire", PhD thesis, France: University of Paris, 1982.
- [105] R. Niemiec and F. Gandhi, "A Comparison Between Quadrotor Flight Configurations", *42nd European Rotorcraft Forum*, Lille, France, Sept. 2016.
- [106] R. Niemiec and F. Gandhi, "Effects of Inflow Model on Simulated Aeromechanics of a Quadrotor Helicopter", *American Helicopter Society 72nd Annual Forum*, West Palm Beach, FL, USA, May 2016.

- [107] Z. Ning and H. Hu, "An Experimental Study on the Aerodynamic and Aeroacoustic Performances of a Bio-Inspired UAV Propeller", *35th AIAA Applied Aerodynamics Conference*, Denver, Colorado, USA, June 2017, DOI: 10.2514/6.2017-3747.
- [108] Z. Ning and H. Hu, "An Experimental Study on the Aerodynamics and Aeroacoustic Characteristics of Small Propellers", *54th AIAA Aerospace Sciences Meeting*, San Diego, California, USA, Jan. 2016, DOI: 10.2514/6.2016-1785.
- [109] F. Nitzsche, C. Spieß, R. Leibbrandt, M. Gennaretti, G. Bernardini, J. Serafini, F. Porcaccia, V. Riziotis, G. Papadakis, N. Spyropoulos, A. Siami, D. Hilewit, and M. Rafiee, "A New Comprehensive Analysis Tool for the Preliminary Design and Design Evaluation of Helicopters – The CORAL", *47th European Rotorcraft Forum*, Virtual, Sept. 2021.
- [110] G. Papadakis and S. G. Voutsinas, "In View of Accelerating CFD Simulations through Coupling with Vortex Particle Approximations", *Journal of Physics: Conference Series*, Vol. **524**, No. 1, 2014, DOI: 10.1088/1742-6596/524/1/012126.
- [111] D. A. Peters and C. J. He, "Correlation of Measured Induced Velocities with a Finite-State Wake Model", *Journal of the American Helicopter Society*, Vol. **36**, No. 3, 1991, pp. 59–70, DOI: 10.4050/JAHS.36.59.
- [112] F. Petrosino, M. Barbarino, and M. Staggat, "Aeroacoustics Assessment of an Hybrid Aircraft Configuration with Rear-Mounted Boundary Layer Ingested Engine", *Applied Sciences*, Vol. **11**, No. 7, 2021, DOI: 10.3390/app11072936.
- [113] R. Piccinini, M. Tugnoli, and A. Zanotti, "Numerical Investigation of the Rotor-Rotor Aerodynamic Interaction for eVTOL Aircraft Configurations", *Energies*, Vol. **13**, No. 22, 2020, DOI: 10.3390/en13225995.
- [114] O. Pinti, A. A. Oberai, R. Healy, R. J. Niemiec, and F. Gandhi, "Multi-Fidelity Approach to Predicting Multi-Rotor Aerodynamic Interactions", *AIAA Journal*, Vol. **60**, No. 6, 2022, pp. 3894–3908, DOI: 10.2514/1.J060227.
- [115] D. M. Pitt and D. A. Peters, "Theoretical Prediction of Dynamic-Inflow Derivatives", *Vertica*, Vol. **5**, No. 1, 1981, pp. 21–34.
- [116] J. Prieur and G. Rahier, "Comparison of Ffowcs Williams-Hawkings and Kirchhoff Rotor Noise Calculations", *4th AIAA/CEAS Aeroacoustics Conference*, Toulouse, France, June 1998, DOI: 10.2514/6.1998-2376.
- [117] Q. Quan, *Introduction to Multicopter Design and Control*, Singapore: Springer, 2017, DOI: 10.1007/978-981-10-3382-7.

- [118] M. Raffel, "Background-Oriented Schlieren (BOS) Techniques", *Experiments in Fluids*, Vol. **56**, No. 3, 2015, DOI: 10.1007/s00348-015-1927-5.
- [119] M. Raffel, C. E. Willert, F. Scarano, C. J. Kähler, S. T. Wereley, and J. Kompenhans, *Particle Image Velocimetry: A Practical Guide*, Cham, Switzerland: Springer International Publishing, 2018, DOI: 10.1007/978-3-319-68852-7.
- [120] G. Rahier and Y. Delrieux, "Blade-Vortex Interaction Noise Prediction Using a Rotor Wake Roll-Up Model", *Journal of Aircraft*, Vol. **34**, No. 4, 1997, pp. 522–530, DOI: 10.2514/2.2204.
- [121] G. Rahier and J. Prieur, "An Efficient Kirchhoff Integration Method For Rotor Noise Prediction Starting Indifferently From Subsonically Or Supersonically Rotating Meshes", *American Helicopter Society 53rd Annual Forum*, Virginia Beach, Virginia, USA, Apr. 1997.
- [122] M. Ramasamy, "Measurements Comparing Hover Performance of Single, Coaxial, Tandem, and Tilt-Rotor Configurations", *American Helicopter Society 69th Annual Forum*, Phoenix, Arizona, USA, May 2013.
- [123] M. Ramasamy, T. Lee, and J. Leishman, "Flowfield of a Rotating-Wing Micro Air Vehicle", *Journal of Aircraft*, Vol. **44**, No. 4, 2007, pp. 1236–1244, DOI: 10.2514/1.26415.
- [124] C. Russell and S. Conley, "The Multirotor Test Bed - A New NASA Test Capability for Advanced VTOL Rotorcraft Configurations", *Vertical Flight Society 76th Annual Forum*, Virtual, Oct. 2020, DOI: 10.4050/F-0076-2020-16370.
- [125] N. Schiller, K. Pascioni, and N. Zawodny, "Tonal Noise Control Using Rotor Phase Synchronization", *Vertical Flight Society 75th Annual Forum*, Virtual, May 2019, DOI: 10.4050/F-0075-2019-14455.
- [126] R. Schlinker and R. Amiet, "Helicopter Rotor Trailing Edge Noise", *AIAA 7th Aeroacoustics Conference*, Palo Alto, CA, USA, Oct. 1981, DOI: 10.2514/6.1981-2001.
- [127] F. H. Schmiz, "Reduction of Blade-Vortex Interaction (BVI) Noise through X-Force Control", *Journal of the American Helicopter Society*, Vol. **43**, No. 1, 1998, pp. 14–24, DOI: 10.4050/JAHS.43.14.
- [128] C. Schwarz and J. N. Braukmann, "Practical Aspects of Designing Background-Oriented Schlieren (BOS) Experiments for Vortex Measurements", *Experiments in Fluids*, Vol. **64**, No. 4, 2023, p. 67, DOI: 10.1007/s00348-023-03602-1.

- [129] H. Shraim, A. Awada, and R. Youness, "A Survey on Quadrotors: Configurations, Modeling and Identification, Control, Collision Avoidance, Fault Diagnosis and Tolerant Control", *IEEE Aerospace and Electronic Systems Magazine*, Vol. **33**, No. 7, 2018, pp. 14–33, DOI: 10.1109/MAES.2018.160246.
- [130] D. Shukla and N. Komerath, "Low Reynolds Number Multirotor Aerodynamic Wake Interactions", *Experiments in Fluids*, Vol. **60**, No. 4, 2019, DOI: 10.1007/s00348-019-2724-3.
- [131] D. Shukla and N. Komerath, "Multirotor Drone Aerodynamic Interaction Investigation", *Drones*, Vol. **2**, No. 4, 4 2018, DOI: 10.3390/drones2040043.
- [132] B. Smith, F. Gandhi, and R. Niemiec, "A Comparison of Multicopter Noise Characteristics with Increasing Number of Rotors", *Vertical Flight Society 76th Annual Forum*, Virtual, Oct. 2020, DOI: 10.4050/F-0076-2020-16499.
- [133] A. J. Spyropoulos, A. P. Fragiatis, D. P. Margaritis, and D. G. Papanikas, "Influence of Arbitrary Vortical Wake Evolution on Flowfield and Noise Generation of Helicopter Rotors", *22nd International Congress of Aeronautical Sciences*, Harrogate, UK, Aug. 2000.
- [134] T. C. A. Stokkermans, D. Usai, T. Sinnige, and L. L. M. Veldhuis, "Aerodynamic Interaction Effects Between Propellers in Typical eVTOL Vehicle Configurations", *Journal of Aircraft*, Vol. **58**, No. 4, 2021, pp. 815–833, DOI: 10.2514/1.C035814.
- [135] J. Tan and H. Wang, "Simulating Unsteady Aerodynamics of Helicopter Rotor with Panel/Viscous Vortex Particle Method", *Aerospace Science and Technology*, Vol. **30**, No. 1, 2013, pp. 255–268, DOI: 10.1016/j.ast.2013.08.010.
- [136] *The Most Popular RC (Remote Control): A Ranking of Top Choices*, StrawPoll, <https://strawpoll.com/most-popular-rc-remote-control> (visited on 12/13/2023).
- [137] B. Theys, G. Dimitriadis, T. Andrienne, P. Hendrick, and J. De Schutter, "Wind Tunnel Testing of a VTOL MAV Propeller in Tilted Operating Mode", *2014 International Conference on Unmanned Aircraft Systems (ICUAS)*, Orlando, Florida, USA, May 2014, pp. 1064–1072, DOI: 10.1109/ICUAS.2014.6842358.
- [138] B. Theys, G. Dimitriadis, P. Hendrick, and J. De Schutter, "Experimental and Numerical Study of Micro-Aerial-Vehicle Propeller Performance in Oblique Flow", *Journal of Aircraft*, Vol. **54**, No. 3, 2017, pp. 1076–1084, DOI: 10.2514/1.C033618.

- [139] G. Throneberry, A. Takeshita, C. M. Hocut, F. Shu, and A. Abdelkefi, "Wake Propagation and Characteristics of a Multi-Rotor Unmanned Vehicle in Forward Flight", *Drones*, Vol. 6, No. 5, 5 2022, DOI: 10.3390/drones6050130.
- [140] C. E. Tinney and J. Sirohi, "Multirotor Drone Noise at Static Thrust", *AIAA Journal*, Vol. 56, No. 7, 2018, pp. 2816–2826, DOI: 10.2514/1.J056827.
- [141] C. T. Tran and D. Petot, "Semi-Empirical Model for the Dynamic Stall of Airfoils in View of the Application to the Calculation of Responses of a Helicopter Blade in Forward Flight", *Vertica*, Vol. 5, 1981, pp. 35–53.
- [142] M. Tugnoli, D. Montagnani, M. Syal, G. Droandi, and A. Zanotti, "Mid-Fidelity Approach to Aerodynamic Simulations of Unconventional VTOL Aircraft Configurations", *Aerospace Science and Technology*, Vol. 115, 2021, DOI: 10.1016/j.ast.2021.106804.
- [143] J. Valentin and L. Bernardos, "Validation of a New Solver Based on the Vortex Particle Method for Wings, Propellers and Rotors", *49th European Rotorcraft Forum*, Bückeburg, Germany, Sept. 2023.
- [144] P. Ventura Diaz and S. Yoon, "High-Fidelity Computational Aerodynamics of Multi-Rotor Unmanned Aerial Vehicles", *AIAA SciTech Forum*, Kissimmee, Florida, Jan. 2018, DOI: 10.2514/6.2018-1266.
- [145] A. Visingardi, A. D'Alascio, A. Pagano, and P. Renzoni, "Validation of CIRA's Rotorcraft Aerodynamic Modelling System with DNW Experimental Data", *22nd European Rotorcraft Forum*, Brighton, UK, Sept. 1996.
- [146] *Volocopter | Aerokurier*, <https://www.aerokurier.de/elektroflug/grossbestellung-inklusive-volocopter-joint-venture-in-china/> (visited on 03/22/2024).
- [147] S. Waldherr, *The Mavic 2 Pro from DJI*. Wikimedia Commons, [https://upload.wikimedia.org/wikipedia/commons/7/76/DJI\\_Mavic\\_2\\_Pro\\_mit\\_Hasselblad\\_Kamera.jpg](https://upload.wikimedia.org/wikipedia/commons/7/76/DJI_Mavic_2_Pro_mit_Hasselblad_Kamera.jpg) (visited on 12/13/2023).
- [148] D. Weitsman and E. Greenwood, "Parametric Study of eVTOL Rotor Acoustic Design Trades", *AIAA Scitech 2021 Forum*, Virtual, Jan. 2021, DOI: 10.2514/6.2021-1987.
- [149] S. Y. Wie, S. Lee, and D. Lee, "Potential Panel and Time-Marching Free-Wake Coupling Analysis for Helicopter Rotor", *Journal of Aircraft*, Vol. 46, No. 3, 2009, pp. 1030–1041, DOI: 10.2514/1.40001.
- [150] D. C. Wilcox, "Multiscale Model for Turbulent Flows", *AIAA Journal*, Vol. 26, No. 11, 1988, pp. 1311–1320, DOI: 10.2514/3.10042.

- [151] G. S. Winckelmans and A. Leonard, "Contributions to Vortex Particle Methods for the Computation of Three-Dimensional Incompressible Unsteady Flows", *Journal of Computational Physics*, Vol. **109**, No. 2, 1993, pp. 247–273, DOI: 10.1006/jcph.1993.1216.
- [152] Y. Yang, Y. Liu, Y. Li, E. Arcondoulis, and Y. Wang, "Aerodynamic and Aeroacoustic Performance of an Isolated Multicopter Rotor During Forward Flight", *AIAA Journal*, Vol. **58**, No. 3, 2020, pp. 1171–1181, DOI: 10.2514/1.J058459.
- [153] J. Yin and S. R. Ahmed, "Helicopter Main-Rotor/Tail-Rotor Interaction", *Journal of the American Helicopter Society*, Vol. **45**, No. 4, 2000, pp. 293–302, DOI: 10.4050/JAHS.45.293.
- [154] J. Yin and S. R. Ahmed, "Multiblade Rotors in Forward Flight Utilising Pressure Data from a 3-D Free Wake Unsteady Panel Method", *20th European Rotorcraft Forum*, Amsterdam, The Netherlands, Oct. 1994.
- [155] S. Yoon, P. Ventura Diaz, D. D. Boyd, W. Chan, and C. Theodore, "Computational Aerodynamic Modeling of Small Quadcopter Vehicles", *American Helicopter Society 73rd Annual Forum*, Fort Worth, Texas, May 2017.
- [156] S. Yoon, H. C. Lee, and T. H. Pulliam, "Computational Analysis of Multi-Rotor Flows", *54th AIAA Aerospace Sciences Meeting*, San Diego, California, USA, Jan. 2016, DOI: 10.2514/6.2016-0812.
- [157] N. S. Zawodny, A. Christian, and R. Cabell, "A Summary of NASA Research Exploring the Acoustics of Small Unmanned Aerial Systems", *AHS Specialists' Conference on Aeromechanics Design for Transformative Vertical Flight*, San Francisco, CA, USA, Jan. 2018.
- [158] N. S. Zawodny, D. D. Boyd, and C. L. Burley, "Acoustic Characterization and Prediction of Representative, Small-Scale Rotary-Wing Unmanned Aircraft System Components", *American Helicopter Society 72nd Annual Forum*, West Palm Beach, FL, USA, May 2016.
- [159] X. Zhang, X. Li, K. Wang, and Y. Lu, "A Survey of Modelling and Identification of Quadrotor Robot", *Abstract and Applied Analysis*, Vol. **2014**, 2014, DOI: 10.1155/2014/320526.
- [160] T. Zhou and R. Fattah, "Tonal Noise Acoustic Interaction Characteristics of Multi-Rotor Vehicles", *23rd AIAA/CEAS Aeroacoustics Conference*, Denver, Colorado, USA, June 2017, DOI: 10.2514/6.2017-4054.

- 
- [161] W. Zhou, Z. Ning, H. Li, and H. Hu, "An Experimental Investigation on Rotor-to-Rotor Interactions of Small UAV Propellers", *35th AIAA Applied Aerodynamics Conference*, Denver, Colorado, USA, June 2017, DOI: 10.2514/6.2017-3744.
- [162] W. Zhu, M. Morandini, and S. Li, "Viscous Vortex Particle Method Coupling with Computational Structural Dynamics for Rotor Comprehensive Analysis", *Applied Sciences*, Vol. **11**, No. 7, 7 2021, DOI: 10.3390/app11073149.
- [163] C. Zioutis, A. Spyropoulos, A. Fragias, D. Margaritis, and D. Papanikas, "Influence of Helicopter Rotor Wake Modeling on Blade Airload Predictions", *International Journal of Engineering*, Vol. **3**, No. 6, 2010, pp. 521–535.

# Curriculum Vitae

Anna Aleksandra Kostek

born on 8th of November 1995 in Lublin, Poland

anna.kostek@dlr.de

## Work experience

---

- since 04/2020 **Research scientist** at the German Aerospace Center (DLR), Göttingen
- 11/2019-03/2020 **Postgraduate research exchange** at the German Aerospace Center (DLR), Göttingen
- 03/2018-09/2019 **Master thesis** at Łukasiewicz Research Network - Institute of Aviation, Warsaw, Poland
- 08/2017-09/2017 **Internship** at PZL-Swidnik, Leonardo Helicopters Company, Poland
- 03/2018-09/2019 **Bachelor thesis** at the Institute of Aeronautics and Applied Mechanics, Warsaw University of Technology, Poland

## Education

---

- 04/2020-today **Dissertation** at Gottfried Wilhelm Leibniz University Hannover: *Computational and Experimental Investigation of Quadrotor Aerodynamics and Aeoracoustics*
- 02/2018-10/2019 **Master of Science** in Aerospace Engineering at the Warsaw University of Technology (*with distinction*)
- 10/2014-01/2018 **Bachelor of Science** in Aerospace Engineering at the Warsaw University of Technology